Detailed Investigation on Electromagnetic Noise in Permanent Magnet Brushless Motors for Hybrid Vehicles

Von der Fakultät für Ingenieurwissenschaften,
Abteilung Maschinenbau und Verfahrenstechnik
der
Universität Duisburg-Essen
zur Erlangung des akademischen Grades eines

Doktors der Ingenieurwissenschaften
Dr.-Ing.

genehmigte Dissertation

von
Zakaria El Khawly
aus
Saida, Libanon

Gutachter: Univ.-Prof. Dr.-Ing. Dieter Schramm
Gutachter: Univ.-Prof. Dr.-Ing. Dieter Gerling

Tag der mündlichen Prüfung: 09. Dezember 2013

Dedicated to my Lord

My parents

My wife

Acknowledgment

In the name of Allah, the Most Gracious, the Most Merciful

To the leader of my life; it is always possible to gratitude people in different ways but with God, it is not possible to do more than "THANKS".

At the onset, I would like to exhibit my deepest thanks to Prof. Dr. Ing. Dieter Schramm for his consistent trust, unending support and great help. Without him, this work would never initiate nor finish.

I would like to pay my deepest gratitude to Prof. Dr. Ing. Dieter Gerling who has given me his time, assistance and patience so generously.

I would like to say "Thanks" for those people that might I forget to mention them in my acknowledgements but they have given me their support and assistance.

I would like to pay my deepest gratitude to my wife for her support, and her words of encouragement.

Finally, I would like to thank my parents for their unending support, willingness to accept and eagerness to love.

Zakaria El Khawly *München, October 2014*

Abstract

In this work, a scientific approach for computational evaluation and for theoretical and practical systematic design considerations for noise behavior of Permanent Magnet (PM) brushless motors used in the power train of hybrid vehicles has been established. This work provides designers and engineers with detailed description and specific information about electromagnetic noise, its generation process and the relation between the different scientific fields required in the complete evaluation process. It also explains modern electromagnetic concepts which help to fulfill the requirement of hybrid power train and introduces the different winding topologies. In this work, an explicit analysis of time and space harmonics for air-gap flux density or, rather, of magnetic forces, has been dealt with in detail and then related to their corresponding mechanical modes. The paper also introduces the electromagnetic parameters that contribute to the determination of these harmonics. Detailed mechanical and dynamic analyses needed for the evaluation process of noise have been completely covered. An analytical method for modeling the stator and for calculating its modal characteristics has been introduced. The mechanical factors that affect the results of modal and harmonic analyses are also investigated based on experimental and simulation results. A theoretical background concerning the structure borne sound, the airborne sound and their acoustic parameters is also included. The acoustic simulations were performed to synchronize electromagnetic and mechanical results and subsequently to compute the noise level. The design considerations which improve the electromagnetic design of PM motors and guarantee an enhanced vibration and noise behavior have also been revealed. The skewing effect on the torque ripple and the noise behavior has also been investigated with respect to a discrete skewed rotor topology. A complete chain of analysis for computation of vibration and noise has been defined using the analytical approaches as well as the modern numerical methods such as Finite Element Method (FEM), Boundary Element Method (BEM) and Fast Multi-pole Boundary Element Method (FMBEM).

Kurzfassung

Im Rahmen dieser Arbeit wurde ein systematischer Ansatz zur theoretischen und praktischen Designbetrachtung, sowie zur rechnerischen Auswertung des Geräuschverhaltens permanenterregter Motoren für den Antriebsstrang von Hybridfahrzeugen untersucht. Diese Arbeit bietet Ingenieuren und Maschinenauslegern detaillierte und spezifische Informationen über das elektromagnetische Betriebsgeräusch, seinen Entstehungsprozess und die für eine Bewertung notwendigen Beziehungen zwischen den verschiedenen physikalischen Bereichen. Dabei werden insbesondere moderne elektromagnetische Konzepte und Wicklungstopologien untersucht, die für die Erfüllung der Anforderungen in einen Hybrid-Antriebsstrang benötigt werden. Die Luftspaltflussdichte, bzw. die magnetischen Kräfte wurden hierbei zeitlich und räumlich analysiert um die entsprechenden Strukturmoden zu ermitteln. Zudem werden wichtige elektromagnetische Parameter vorgestellt, welche einen signifikanten Einfluss auf die Luftspaltoberwellen haben. Detaillierte mechanische und dynamische Analysen, die für den Bewertungsprozess des Betriebsgeräusches notwendig sind, werden im Rahmen der Arbeit ausführlich behandelt. Eine analytische Methode für das Modellieren des Stators und das Berechnen seiner modalen Eigenschaften wurde eingeführt. Die mechanischen Faktoren, die die Ergebnisse von modalen und harmonischen Analysen beeinflussen, wurden sowohl simulativ, als auch experimentell, untersucht. Die Arbeit umfasst zudem die theoretischen Hintergründe von Luft- und Körperschall, sowie weiterer akustisch relevanter Größen. Um den Geräuschpegel berechnen zu können, wurden elektromagnetische, strukturdynamische und akustische Simulationen miteinander kombiniert. Wichtige Maßnahmen, die zu einer Verbesserungen des elektromagnetischen Designs und insbesondere des vibro-akustischen Verhaltens führen, sind herausgearbeitet worden. Beispielsweise wurde der Einfluss von Schrägung auf die Drehmomentwelligkeit und das Geräuschverhalten für eine diskret geschrägte Rotor Topologie untersucht. Eine vollständige Analysekette für die Berechnung des Vibrations- und Geräuschverhaltens wurde sowohl mit analytischen Methoden, als auch mit modernen numerischen Methoden wie der Finite Element Method (FEM), der Boundary Element Method (BEM) und der sogenannten Fast Multi-pole Boundary Element Method (FMBEM) definiert.

TABLE OF CONTENTS

1 Introduction

1.1 Background

The two important challenges confronting the world today are the increased energy demand due to the growth of global population, and the growing environmental concerns regarding air pollution, global warming and greenhouse gas emissions. These issues are forcing automobile manufacturers to support the development of safer, cleaner, and more efficient vehicles. The Hybrid Electric Vehicle (HEV) is an example of one of the most promising and efficient technologies. This technology is not really new because it was presented many years ago in diesel-electric locomotives. At that time, it was abandoned by the automobile manufacturers due to the absence of high performance batteries and due to the availability of fossil fuels at reasonably low costs. However, the situation has radically changed in recent times. This is due to the energy shortage with its consequence of high and unpredictable fuel price as well as to dramatic environmental deterioration. All these give rise to the development of a drive train with high performance aggregates.

Recent advances, such as the availability of high-power electronic devices like IGBT transistors, the development of electric motors with high efficiency and large operation speed range, and the production of high performance batteries with non-aqueous storage systems like Lithium-Ion-System, present a renewed opportunity for the reconsideration of this competent technology. All these factors have given a real boost to the HEV technology during the past decade and have made it feasible for automotive applications where mass production is demanded.

1.2 Motivation and Objective

The two main reasons behind the development of such economical vehicles are energy shortage and environmental concerns.

1.2.1 Energy Shortage

The growth of the world's population is causing an increase in the demand for energy and, consequently, in the consumption of oil. Around 60% of the total oil consumption goes to transportation [Mi2011], and that is because both gasoline and diesel used for vehicles are refined from fossil oil. The American Petroleum Institute estimated in 1999 that the world's oil supply would be depleted between 2062 and 2094 (see Fig. 1-1) [Mi2011]. This explains the urgency to develop vehicles with high energy efficiency and economical fuel consumption.

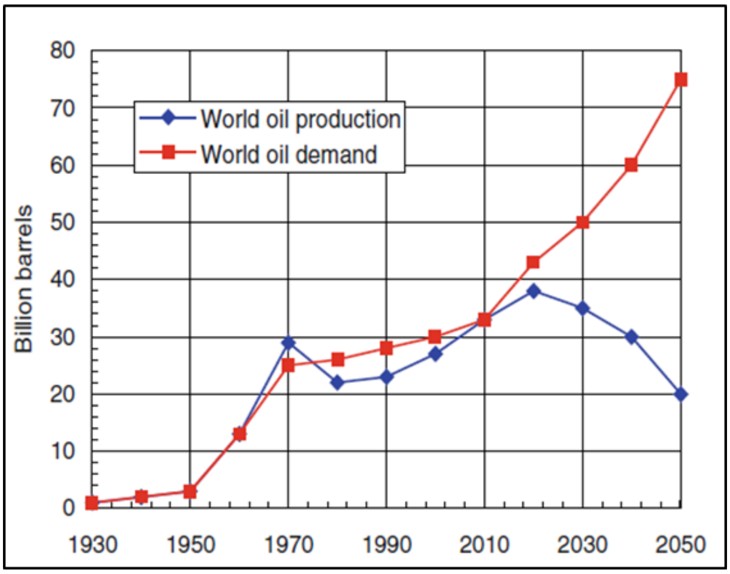

Figure 1-1:Oil production with oil demand up to the year 2050 [Eia2009]

1.2.2 Environmental Deterioration

The main environmental impact elements are air pollution (AP) and greenhouse gas (GHG) emissions. These environmental elements are essentially affected by the fuel-power train used in all transportation types. The greenhouse effect, which is induced by the presence of carbon dioxide and other gases, such as methane, contributes to global warming. The global warming effect entails an increase in the earth temperature and leads to major ecological damage in the ecosystems of the earth and leads to many natural disasters (see Fig. 1-2) [Meh2010].

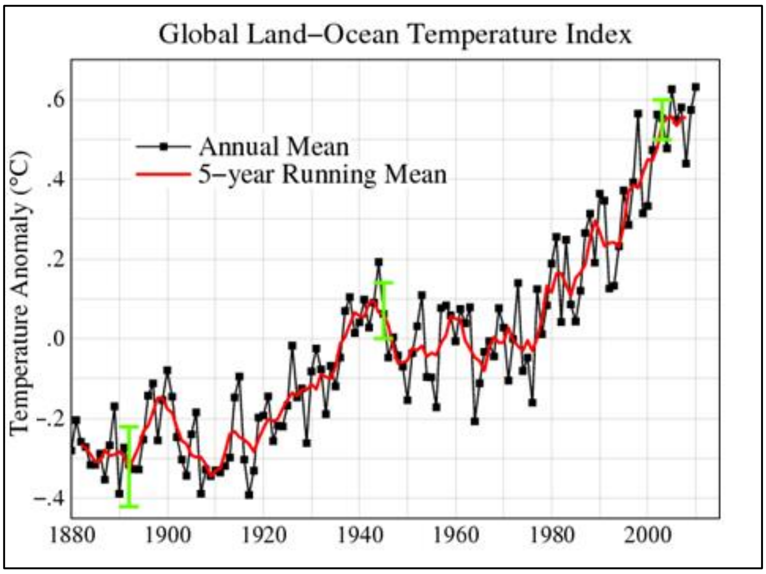

Figure 1-2: Plot of global mean land-ocean temperature index, from 1880 to 2010 [Gis2011]

In Figure 1-3, the temperature variation with a geographical distribution is represented.

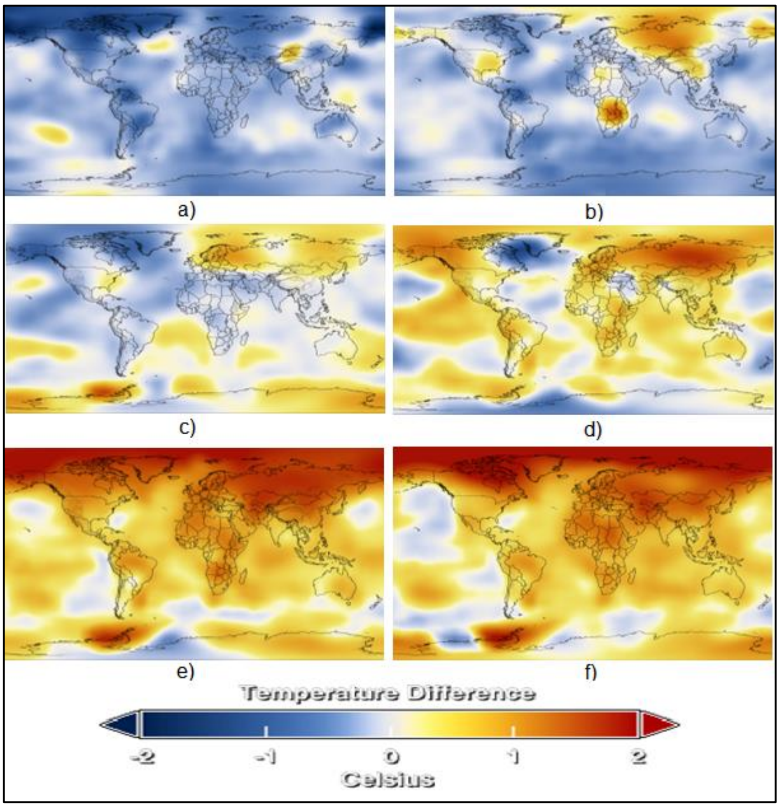

Figure 1-3: Global temperature anomalies distributed geographically from a) in 1891 to f) in 2010 [Nas2011]

A further environmental element, which also has to be considered, is noise pollution. This is one of the most unpleasant environmental hazards of this age. According to physicians and pathologists, noise can even cause permanent damage to the organs involved in hearing and it can also bring on disorders of the central nervous system [Tim1989].

To defeat these environmental hazards, a design of environmentally benign vehicles characterized by little or no atmospheric pollution and by low fuel consumption is highly demanded.

1.3 Hybrid Electrical Vehicle (HEV)

A vehicle is called a hybrid vehicle if it has two or more onboard power sources. The onboard power sources can be gasoline (or diesel), batteries and hydrogen. A power train corresponds to each type of power sources. The term “power train” means the on-board energy source, and the energy converter. Accordingly, a vehicle which has two power trains, such as a gasoline (or diesel) tank with an Internal Combustion (IC) engine and an electrical power train (electric motor, power electronics and battery) is called a Hybrid Electrical Vehicle (HEV). These

HEVs, which use these two power sources, have the advantages of both IC engine vehicles and Electrical Vehicles (EV). This is because the two power trains complement each other since they both, in the process, overcome their disadvantages [Ehs2010].

In HEV's, the hybrid drive train, which enfolds the aggregation of all power trains, has the following characteristics:

1. Hybrid traction: this is where both the IC engine and the electric motor work together at the same time and supply torque and power to the driven wheels. Here, the electric motor intensifies the power of the drive train and plays a boosting role to increase the power of the vehicle.
2. Engine-alone traction: at operating range of high efficiency, the IC engine runs alone and produces the required power to the driven wheels.
3. Motor-alone traction: inside the cities where a small power is sufficient, the electric motor runs alone, drives the vehicle safely, quietly, and cleanly with zero emissions.
4. Recuperation of braking-energy: in IC engine vehicles, the braking energy is dissipated in the form of heat at the braking system. A hybrid drive train allows the recapture of the energy which goes to the braking system by absorbing the kinetic and potential energy of the vehicle and using it to drive the electric machine in the generator operation mode.
5. Recharging battery from the engine: If the produced power of the IC engine is not fully needed for propulsion or the battery of the electric power train becomes empty, the additional mechanical energy is transformed into electric energy and then stored in a high voltage battery. This energy is utilized later by the electric drive train.

1.3.1 Electrical power train

In this era of upheaval and rapid change, the electrical power train occupies a significant part in individual mobility. The three main components which represent an electrical power train are: the storage system or battery, the power electronics and the electrical motor.

In this work, the focus is on the electrical motor. It is strongly recommended to have a compact electrical motor with a high efficiency and a high power density which has to be able to operate in motor and generator operation modes.

Interior Permanent Magnet (IPM) Motor

To fulfill these requirements, the Interior Permanent Magnet (IPM) motors have been adopted. This is particularly due to their high efficiency, compact size, high power density, and their special torque and power characteristic curves. The IPM motors have earned this great importance in the electrical power drives because they have a high starting torque and a wide constant-power speed area. They are also able to operate as motors during electric driving and as generators during energy recuperation and battery recharging.

To make these motors more compact, new design concepts are implemented. The concepts of non-overlapping windings with segmented teeth in stator and with a fractional slot number per pole per phase are implemented. The non-overlapping windings (fractional slot windings or concentrated windings) are used to extend the effective length of the iron core. With the non-overlapping windings, the iron and copper mass is reduced in the machine. As a result, a longer stator stack in the same frame length can be achieved. This is because the axial length of the end winding becomes smaller [Sal2004]. With a segmented teeth concept, the waste material is reduced considerably during the stamping process of rotor and stator lamination sheets, which reduces the initial costs of those motors and makes their commercial production feasible.

On the other hand, the iron cores of those machines operate under magnetic saturation. The additional electric and magnetic loads mean higher flux densities and a deeply magnetic saturation, all of which aggravate the noise and vibration level of these motors. As a consequence, the noise and vibration behavior of these motors are problematic above all records. The noise and vibration behavior of IPM motors differ significantly in the drive-train from that of combustion engines or gearboxes. This is particularly due to their tonality and the strong high frequency content [Boe2008]. Therefore, more attention has to be devoted to the generated noise by the IPM motors in order to achieve more efficient designs and better noise behavior.

In this work, the noise and vibration behavior of IPM motors will be investigated from different levels on the basis of electromagnetic, mechanical and acoustic computations and simulations. The goals can be summarized as follows:

- To develop IPM motors with a comfort making behavior, a quiet tonality, an acceptable noise level regarding the noise standards and a high efficiency;
- To develop a methodology in the estimation of noise for synchronous machines and especially for IPM motors that can qualify and quantify the generated noise and provide realistic values regarding the radiation factor, sound velocity and sound pressure levels;
- To establish reliable vibration, noise and reduction techniques for this machine category and then to demonstrate their low noise capability;
- To estimate, in earlier design phases the noise behavior of the machine and then to improve the overall design in order to minimize the post-production solutions during the series phase, where a non-optimal design regarding the noise and vibrations can be determined.

Noise and vibration in IPM

The IPM motors, or rather all electric motors, generate vibration and noise during operation due to three types of excitation: aerodynamic, mechanical and electromagnetic. The aerodynamic noise represents the smallest fraction of the whole generated noise in the electric machines, whereas the noise of mechanical origin, as is already known, is identified as resulting from the dynamic operation of several kinds of machine. However, the noise of electromagnetic origin cannot be easily predicted due to its complicated origin and its interaction with the mechanical vibrations [Lac2004]. Generally, the factors affecting this type of noise are:

- Winding topology
- Shape design of stator and rotor lamination sheets

- Shape and orientation of magnets
- Air gap shape
- Operating points, frequencies and loads

All these factors influence the magnetic field in the air gap. This magnetic field produces magnetic forces which excite the body of the machines. In fact, the static magnitudes of these forces do not contribute to the production of vibration and noise, but rather it is the dynamic variation of these forces that is responsible for this problem. This fluctuation in the amplitude of forces attacks the stator with different frequencies, excites its dynamic behavior and sets it into resonance.

1.4 Outline of the Thesis

In general, to put a system into a state of vibration, it is always necessary to excite its structure with a dynamic force or with a force that changes temporally. Therefore, it is important to know the origin and type of this force. When the origin of the exciting force is known, the next step is to analyze this force and to determine its frequency orders and their amplitudes. Despite its various stages, the noise is detected in its last state as airborne sound. The process of generation of the electromagnetic noise starts in the air gap of the IPM motor. The magnetic forces and their harmonics act dynamically on the teeth of the stator. The reaction of the stator can then be summarized in terms of its spatial deformation and temporal agitation. The results of the stator reaction are, firstly, vibration in the structure, which, at this stage, is called the structure borne sound process. Then the surface of the stator emits a part of this energy to the surrounding area. This emitted energy is defined by the radiated acoustic energy, and it goes under the field of the airborne sound. Each state in the process of noise generation in IPM motors has a different scientific background and each must be treated separately (see Fig. 1-4).

In Chapter 1, the introduction gives an overview of the thesis and states the objectives of this work. In Chapter 2, the electromagnetic design is investigated. New design concepts in IPM motors are presented and an analytical study is performed to determine the harmonics of magnetic forces that can appear in the air gap. Electromagnetic simulations are performed to compute the magnetic field, and to determine the Maxwell forces with their harmonics and their static and dynamic amplitudes.

These forces, with their frequencies and modes, represent the system exciter for the process of noise generation in all electric motors. In Chapter 3, these forces are subjected to the stator of the machine in order to determine its dynamic behavior and modal characteristics. The stator is the transporter medium for vibration and noise. A theoretical study is presented to introduce the mathematical and analytical methods in the computation of stator modal characteristics. Numerical simulations are then performed to determine exactly the Eigen frequencies and modes of the stator. But first, an experimental modal analysis is performed to determine the damping and the friction factors for every mode.

These factors are implemented in the simulation to achieve a realistic situation environment. A harmonic response analysis is then performed to calculate the deformations in the stator structural. As a result, each mode is then described by its Eigen frequency and deformation value.

The deformations and their time derivatives, which are the vibration velocities, are then calculated. In order to determine the noise behavior of the machine, the acoustical computations have to be performed. This is done in Chapter 4. The radiated acoustic energy and the generated noise are consequently computed. The acoustic levels of all dominant modes are determined.

In Chapter 5, procedures for the optimization of electromagnetic design are introduced. A geometrical optimization for rotor and stator lamination sheets is done completely. The effect of the skewing process is theoretically introduced and then investigated. An optimal design of the studied motor is then proposed.

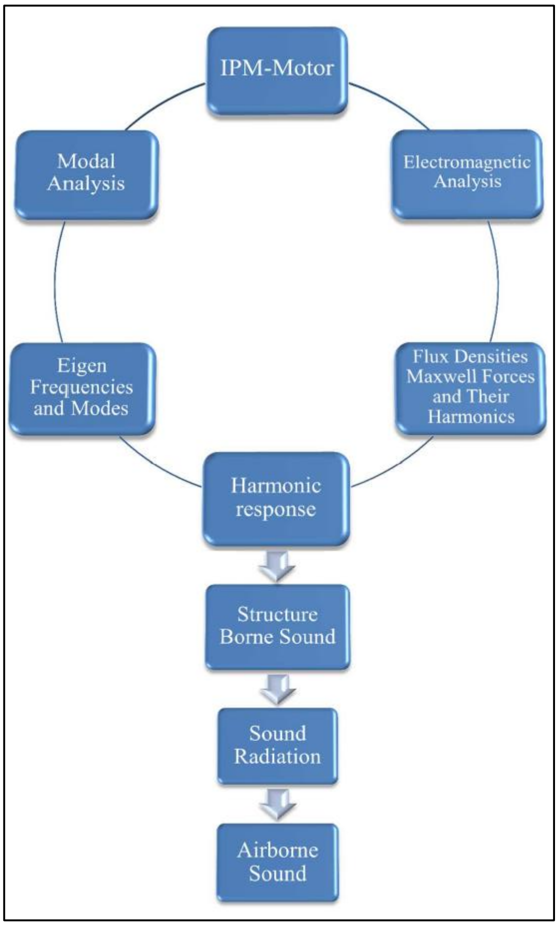

Figure 1-4: States and steps in the generation process of noise in IPM motor

1.5 Reviewed Literature

From time immemorial, the importance of electromagnetic noise in the design of electric machines was a main subject of discussion for engineers and designers. This led to numerous research activities and investigations to discover the reasons behind the noise generation process and to establish a methodology for dealing with this topic. In lieu of this aforementioned fact, a general review of the noise generation in electric motor was introduced by *Verma* (1996) and *Vijayraghaven* (1998) [Ver1996, Vij1998].

Later on, the investigation focused on every type and concept of electric motors that has been used in the last hundred years.

On induction motors, several projects that lead to Ph.D. theses have been carried out to analyze the generation process of electromagnetic noise. *Gerling* (1992) studied the influence of the current harmonics on the generated noise. The noise calculation was performed analytically using a two-dimensional model of the magnetic field. Likewise, the Maxwell surface forces have been determined and used in the calculation of acoustic noise level [Ger1992]. *Arians'* (2001) focus and dedication was to establish a 3D electromagnetic model and, consequently, to calculate the magnetic forces for the acoustic investigation of an induction machine [Ari2001]. For *Lach* (2005), the focus was on the magnetic noise emitted by the cage rotor of the induction motor. The author compared the results of the measurement of noise with those obtained from simulation [Lac2005].

For switched reluctance motors, the electromagnetic noise has been studied by some engineers in order to find an optimal electromagnetic design with low and quiet acoustic behavior. In 1992, *Cameron* carried out an experimental investigation to study the acoustic noise emitted from a doubly salient variable-reluctance motor. Also, the radial modes and their deformations have been derived experimentally [Cam1992]. By *Mahn* (in 1996), the calculation of magnetically-induced forces and the dynamic response of motor structure to these forces have been introduced [Mah1996]. According to *Anwar* (2000) and *Lachman* (2003), an analytical model for calculating the magnetic radial force and the circumferential mode frequencies from the geometry and operating conditions was studied [Anw2000, Lac2003]. In 2006, *Matveev* introduced the methods for optimal design of switched reluctance motors which led to the award of doctor of philosophy (Ph.D.). The noise behavior is considered to be an important step in the electromagnetic design. Therefore, an analytical model to estimate the vibration and noise behavior has been achieved [Mat2006]. By *Divandari* (2011), two mathematical methods have been proposed to determine and optimize the radial forces by adjusting the machine parameters in the controller [Div2011].

Grüning (2006) investigated the vibration resulting in the end winding of a large turbo generator. The electromagnetic forces are described and calculated with different methods. The goal was to calculate the electromagnetic forces acting on the end winding and to investigate the initiated vibration in this part of the turbo generator [Grü2006].

Several works have also been carried out to investigate the vibration and noise for permanent magnet brushless motors. This is because the permanent magnet motor has been introduced as the best motor type that can be used in the field of electro-mobility. By *Chen* (2008) and *Yang* (2009), the electromagnetic vibration of PM machine has been investigated. The electromagnetic forces have been calculated using a two-dimensional finite element model and prediction of corresponding vibration spectrum [Che2008, Yan2009]. By *De Medeiros* (1998), both Maxwell stress tensor and the energetic principle methods have been applied to calculate the magnetic forces on the surface of the permanent magnet using finite element models [DeM1998]. According to *Zhu* (2002), an analytical technique which can predict the magnetic field distribution in brushless permanent magnet machines has been introduced [Zhu2002]. By *Asano* (2002), the radial forces in PM motor with concentrated winding have been optimized and reduced by changing the air gap thickness [Asa2002]. According to *Chen* (2006), a prediction method for the electromagnetic vibration of PM brushless Motors has been presented. The electromagnetic forces have been calculated using a two-dimensional model. These forces have been utilized to predict the stator deformation analytically [Che2006]. By *Gieras* (2007), the acoustic noise radiated by electric motors was predicted. The sound power level has been calculated on the basis of magnetic field analysis in the air gap, radial forces, and natural frequencies of the stator- frame system and radiation efficiency coefficient [Gie2007].

From the above mentioned literature, the reasons behind the generation of noise in electric machines can be deduced. However, the investigation process is not described in detail. A complete description of a methodology cannot be achieved. The special design of permanent magnet motors for hybrid power trains is not considered and the new design concepts that are implemented in PM motors are not treated. Even the influence of the stator mechanical design on the acoustic behavior has not been examined and the description of electromagnetic forces in time and space domains has also not been separately preserved. The implementation of new numerical tools for realistic acoustic simulations has not been reflected upon, which explains why in depth research is needed to cover the gap left by the earlier researchers and their findings.

2 Electromagnetic Force Analysis

2.1 Introduction

This chapter outlines the theoretical and numerical considerations of the electromagnetic noise for synchronous machines with buried magnets, showing the stator and rotor fields as well as the air gap field. The derived equations can be used not only for synchronous motors with distributed windings, but also for motors with concentrated windings. The effects of the winding arrangement as well as the stator slots and the number of pole pairs will be examined. The radial force waves with their amplitudes and frequencies will be described. The effects of the stator slots and the magnetic saturation will also be demonstrated.

This chapter therefore aims to determine the electromagnetic field distribution and the magnetic forces theoretically and numerically. A precise knowledge of the electromagnetic characteristics of synchronous machines will explain and substantiate the noise generation of synchronous machines.

2.2 Magnetomotive Force (MMF)

The sinusoidal current of a three-phase system can be represented by:

$$\begin{aligned} i_1 &= \sqrt{2}I\cos(\omega t) \\ i_2 &= \sqrt{2}I\cos(\omega t - 2\frac{\pi}{3}) \\ i_3 &= \sqrt{2}I\cos(\omega t - 4\frac{\pi}{3}). \end{aligned} \tag{2.1}$$

The values here are: (i) the alternating current, (I) the root mean square (rms) value of the current, (ω) is the electric angular frequency and (t) is the time.

With an AC wave, the magnetomotive force changes both spatially with (α) and temporally with time (t). A three-phase symmetrical stator, which is fed with three sinusoidal currents, has a total magnetomotive force MMF as follows [Gie2006]:

$$\Theta\,(\alpha,t) = \sum_{\nu=6k\pm1}^{\infty}\overline{\Theta}\,\left[\cos(\omega\,t \mp \nu p\alpha)\right], \tag{2.2}$$

where $\overline{\Theta} = \frac{3\sqrt{2}}{\pi}\frac{N\,\xi_\nu}{\nu p}I$, N is the number of turns in series per phase, ξ_ν is the winding factor per phase corresponding to the harmonic number ν, p is the pole pair number and k is an integer.

2.3 Air Gap Field

To determine the electromagnetic forces, the air gap field should be analyzed. The entire air gap field in the electric motor comprises the stator and rotor fields. Each air gap field can be represented as a rotating wave that is identified by the number of pole pairs and the angular frequency.

2.3.1 Stator Field

The rotational field of the stator can be generated by the multi-phase stator winding, through which current flows. The stator winding of the permanent magnet synchronous machine for hybrid power train is almost a three-phase winding. The three-phase windings are inserted in the stator slots of the laminated core according to a winding configuration. The air gap field and its corresponding harmonics depend on the geometrical design of the slots and the winding configuration.

Stator winding

In general, there is a considerable number of winding configurations or arrangements, which differ in terms of their production process, costs and electromagnetic effects. In the case of stator windings, the phase windings are either nested in one another (distributed winding) or arranged in succession (concentrated winding) [Jur2003]. The concentrated winding (tooth coil winding, individual tooth winding) can be wound around a tooth. In a "distributed winding", more than one slot can be overlapped. In contrast to the distributed windings, the concentrated windings have closely positioned coils with excellent heat emission to the laminated core; the short winding length and high slot filling factor result in very small winding resistance [Got2007]. Thereby they ensure lower winding losses in the coils. A characteristic measure of the winding structure is the number of slots per pole per phase q, which indicates how many slots are available per phase and pole (given by number $2p$) [Jur2003].

$$q = \frac{Z}{2p \times m_{ph}} \tag{2.3}$$

Here, Z is the tooth number, p the pole pair number, and m_{ph} the phase number.

If q is an integer, the winding is called an "integer-slot winding". However, if q=b/c (counter b and denominator c are relatively prime) is a fractional rational number, the winding is then a "fractional-slot winding". The integer-slot winding generally corresponds to the distributed winding. The concentrated windings are always fractional-slot windings.

As mentioned above, the concentrated winding system has certain advantages over the distributed winding system. This winding type can be a two-layer or one-layer winding. A two-layer winding exists if each tooth is wound, whereby two coil sides are located in each slot. If only one coil side is in each slot, this is then referred to as a one-layer winding (see Fig. 2-1 a), b)). One drawback here is that the air gap field of the concentrated windings has a wide amplitude spectrum, which can be influenced by the pole slot number combination and the winding arrangement. Therefore, the work in this chapter will focus on the analysis of concentrated two-layer windings and their air gap fields.

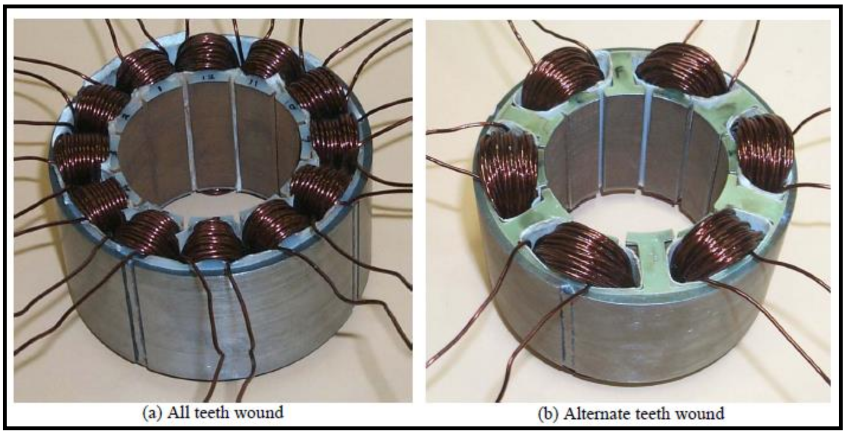

Figure 2-1: Two-layer winding (a) and single-layer winding (b) [Ish2004]

Concentrated windings in three-phase machines

The windings in the PM motors in hybrid power trains are usually designed as concentrated two-layer windings. This means that the coil width (y) is shortened in comparison to the pole pitch (τ). In contrast, the coil width of distributed windings corresponds generally to the pole pitch of the electric machine.

$$\tau = \frac{2\pi}{2p} \tag{2.4}$$

In case of a tooth coil winding (concentrated winding), the coils are wound around a tooth, and the coil width (y) is thus y=*s* (slot pitch) [Got2007].

$$s = \frac{2\pi}{Z} \tag{2.5}$$

The general formula that relates the poles, teeth and phase numbers for the three-phase machine with two layer windings can be expressed as follows [Hof2005]:

$$\begin{aligned} \frac{Z}{2p} &= \frac{m_{ph}}{m_{ph}+1} \rightarrow 2p > Z, \\ \frac{Z}{2p} &= \frac{m_{ph}}{m_{ph}-1} \rightarrow 2p < Z, \end{aligned} \tag{2.6}$$

where m_{ph} is the phase number.

For three phase machines, the phase number is m_{ph}=3. Then Eq. 2.6 can be written as:

$$\frac{3}{4} \leq \frac{Z}{2p} \leq \frac{3}{2}. \tag{2.7}$$

Based on Eq. 2.7, the pitch factor for three-phase machines can then be defined as the ratio of the slot pitch to the pole pitch:

$$\frac{2}{3} \leq \frac{s}{\tau} \leq \frac{4}{3}. \tag{2.8}$$

Using Eq. 2.3, the slot number of a three-phase stator winding is calculated as follows:

$$Z = 6p \times q. \tag{2.9}$$

Applying Eq. 2.9 in Eq. 2.7, the number of slots per pole per phase "*q*" will be restricted to the range.

$$\frac{1}{4} \leq q \leq \frac{1}{2}. \tag{2.10}$$

Additionally, the three phases have to be electrically offset from each other with a spatial angle of 120°; for this purpose, the following condition must be fulfilled [Got2007]:

$$k_T = \frac{Z}{3p} + i\frac{Z}{p}. \tag{2.11}$$

k_T and i are integers here.

The interconnection of the coils and the winding arrangement along the circumference of the stator plays an important role in determining the air gap field. The number of coils in a phase can be determined by dividing the coil number by the phase number n_S / m_{ph} [Adz2008].

$$n_{SP} = \frac{n_S}{m_{ph}} \tag{2.12}$$

Here, n_s is the number of coils, n_{sp} the coil number of one phase.

The coils of one phase can be connected in series or in a parallel way, as required. If the coils of one phase are divided into several groups along the stator, each individual group is recognized as a zone. The coil number of one zone (n) and the number of zones of one phase (n_{ZP}) can only be integers, and their product must yield the number of coils per phase.

$$n_{SP} = n \times n_{ZP}. \tag{2.13}$$

To increase the conductor cross-section of a phase, the coils have to be connected in a parallel way, whereas the winding number (N) of the phase is increased by connecting the coils in series [Adz2008].

The winding arrangement primarily influences the zone factor or rather the winding factor. The winding factor is proportional to the torque, i.e. an electric machine with a low winding factor must compensate its lower torque with a higher current. The zone factor is the result of the fact that each zone comprises multiple adjoining coils. If each zone were only to comprise one coil, the zone factor would always be equal to one.

There are various options for winding the coils of a definite combination of poles and teeth. The best winding arrangement is the one which gives the highest winding factor [Mei2008]. Also, choosing an appropriate combination of poles and teeth numbers significantly increases the winding factor [Mag2003].

A method for determining the best winding arrangement or the maximum winding factor for the non-overlapping windings is described in [Cro2002]. Using an electric machine with Z=30 and p=10, the steps can be summarized as follows:

1- The number of slots per pole per phase q has to be reduced to its lowest terms: q=b/c, whereby "b" and "c" are integers. So, if q=1/2, this means that b=1 and c=2.

2- The slots of the stator on each side have to be nominated by a series of zeros and ones. The basic sequence of zeros and ones can be deduced using the "b" and "c" integers. This basic sequence then has to be repeated among all the slots in the stator. For the basic sequence, the number of ones is equal to "b" and the number of zeros is equal to (c-b). For the studied machine, the numbers of ones and zeros are both equal to one. Consequently the basic sequence is defined by "1 0"and has to be repeated by $3\times 2p/\text{c}=Z/\text{b}=30$. In the general case where the numbers of ones and zeros are different and greater than 1, the ones have to be distributed as regularly as possible in the basic sequence.

3- The whole sequence is compared then with the arrangement of the distributed winding with 3×2p slots and q=1. The sequence for the distributed winding with q=1 is [AC'BA'CB'] whereby A' identifies the return conductor of A.

Figure 2-2: Step 2 and 3 in the winding arrangement method

4- The phases corresponding to"1" are retained and form a layer of the winding arrangement. The second layer is obtained by setting the corresponding return line on the other side of the tooth A' for A, B' for B.

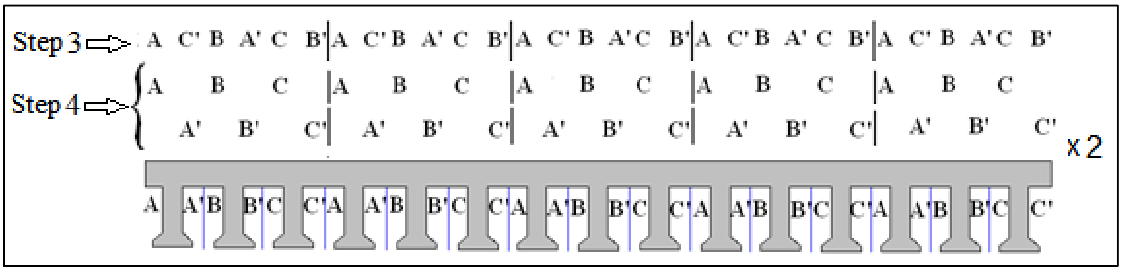

Figure 2-3: Step 4 in the winding arrangement method

5- A vector S is derived to describe the winding arrangement of a phase. It can be used to calculate the winding factor. This vector S consists of the slot numbers describing phase A. For the return conductor A', a minus is added for the corresponding slot number [Lib2005].

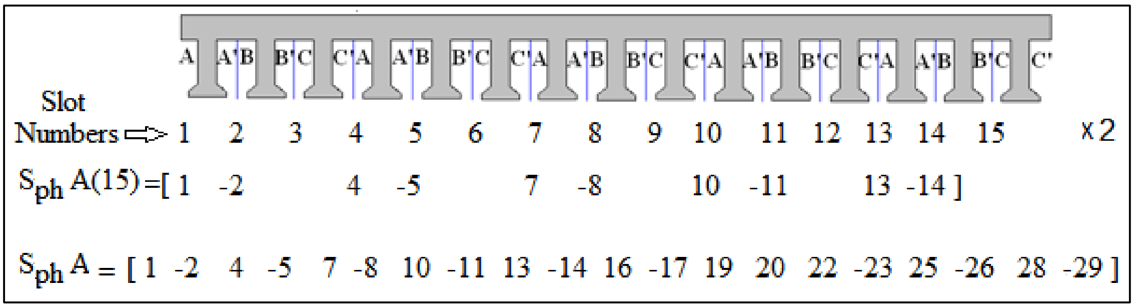

Figure 2-4:Step 5 in the winding arrangement method

Calculation of the winding factor

The winding factor can be calculated by different methods. One of them is to calculate the **E**lectro **M**otive **F**orce EMF phasor ($\vec{E}_i$) (per unit) of each coil side from a phase A using the vector S which is represented above. This method is described in ([Mei2008] and [Mag2003]).

Using the vector S, the electromotive force EMF phasors ($\vec{E}_i$) for the fundamental wave (ν=1) can be calculated using the following equation:

$$\vec{E}_i = sign(S(i))e^{j\frac{\pi 2p}{Z}|S(i)|} \tag{2.14}$$

where Z is the slot number of the electric machine.

For the harmonics:

$$\vec{E}_{i\nu} = sign(S(i))e^{j\frac{\nu\pi 2p}{Z}|S(i)|} \tag{2.15}$$

The resulting EMF phasor is the sum of the EMF element phasors ($\vec{E}_i$) assigned to that phase (per unit), as given by:

$$\vec{E}_{phase,pu} = \sum_{i=1}^{n_l Z/3} \vec{E}_i \tag{2.16}$$

The winding factor of the fundamental wave ($\nu = 1$) is found by dividing the magnitude of the resulting phasor ($\vec{E}_{phase,pu}$) by the number of winding elements per phase, as given by:

$$\xi = \frac{1}{n_l Z/3}\left|\sum_{i=1}^{n_l Z/3} \vec{E}_i\right| \tag{2.17}$$

and for the harmonics[Eme2009]:

$$\xi_\nu = \frac{1}{n_l Z/3}\left|\sum_{i=1}^{n_l Z/3} \vec{E}_{i\nu}\right|. \tag{2.18}$$

Here, *i* is an element in S, n_l is the winding type (single-layer winding n_l=1; or two-layer winding n_l=2).

The sum of the EMF phasors ($\vec{E}_i$) in a phase yields to the resultant EMF phasor (see Fig. 2-5).

$S_{\text{ph A}}$=[1 -2 4 -5 7 -8 10 -11 13 -14 16 -17 19 -20 22 -23 25 -26 28 -29]

$$\sum_{i=1}^{20}\vec{E}_i = e^{j\frac{\pi 2p}{Z}} - e^{j\frac{2\pi 2p}{Z}} + e^{j\frac{4\pi 2p}{Z}} - e^{j\frac{5\pi 2p}{Z}} + e^{j\frac{7\pi 2p}{Z}} - e^{j\frac{8\pi 2p}{Z}} + e^{j\frac{10\pi 2p}{Z}} - e^{j\frac{11\pi 2p}{Z}}$$
$$+ e^{j\frac{13\pi 2p}{Z}} - e^{j\frac{14\pi 2p}{Z}} + e^{j\frac{16\pi 2p}{Z}} - e^{j\frac{17\pi 2p}{Z}} + e^{j\frac{19\pi 2p}{Z}} - e^{j\frac{20\pi 2p}{Z}} + e^{j\frac{22\pi 2p}{Z}} - e^{j\frac{23\pi 2p}{Z}}$$
$$+ e^{j\frac{25\pi 2p}{Z}} - e^{j\frac{26\pi 2p}{Z}} + e^{j\frac{28\pi 2p}{Z}} - e^{j\frac{29\pi 2p}{Z}}$$

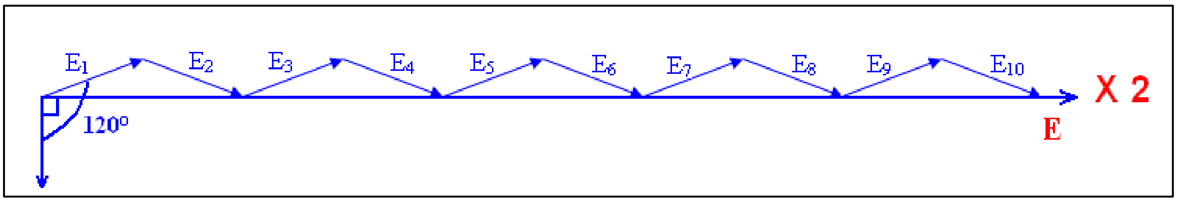

Figure 2-5: The sum of the phasors for a phase

The winding factor is then:

$$\xi = \frac{1}{n_l Z/3}\left|\sum_{i=1}^{n_l Z/3} \vec{E}_i\right| = 0.866$$

Another method can also be applied to calculate the winding factor. This method is based on the definition that the winding factor is the multiplication result of the zone factor by the pitch factor as is the case for conventional machines with distributed winding (with no skewing) [Hof2005].

For the fundamental wave:

$\xi = \xi_Z \xi_S$,

whereby ξ_Z is the zone factor and ξ_S the pitch factor.

For the harmonics (ν):

$\xi_\nu = \xi_{Z\nu}\xi_{S\nu}$.

The pitch factor (fundamental wave) can be calculated for the two-layer winding as follows [Hof2005]:

$$\xi_S = \sin\left(\frac{s}{\tau}\frac{\pi}{2}\right) = \sin\left(\frac{2p}{Z}\frac{\pi}{2}\right) = \sin\left(\frac{m_{ph}n \pm 1}{m_{ph}n}\frac{\pi}{2}\right) \tag{2.19}$$

and for the harmonics[Hof2005]:

$$\xi_{S\nu} = \sin\left(\nu\frac{s}{\tau}\frac{\pi}{2}\right) = \sin\left(\nu\frac{2p}{Z}\frac{\pi}{2}\right) = \sin\left(\nu\frac{m_{ph}n \pm 1}{m_{ph}n}\frac{\pi}{2}\right), \tag{2.20}$$

where *s* is the slot pitch, τ the pole pitch, *2p* the pole number, *Z* the tooth number, m_{ph} the phase number and *n* the number of coils in a zone.

The zone factor for the fundamental wave is [Hof2005]:

$$\xi_Z = \frac{\sin\left(\frac{\pi}{2m_{ph}}\right)}{n \cdot \sin\left(\frac{\pi}{2m_{ph}n}\right)} \tag{2.21}$$

and for the harmonics[Hof2005]:

$$\xi_{Z\nu} = \frac{\sin\left(\nu\frac{\pi}{2m_{ph}}\right)}{n \cdot \sin\left(\nu\frac{\pi}{2m_{ph}n}\right)}. \tag{2.22}$$

According to Eq. 2.19 and Eq. 2.21, the winding factor of the fundamental wave is $\xi = 0.866$.

Harmonics in three-phase machines with fractional-slot winding

With sinusoidal currents and using the number of slots per pole per phase q=b/c, the harmonic number ν of the two-layer windings can be calculated as follows:

Case 1: c is even [Sal2004]:

$$\nu = \pm\frac{1}{c}(2m_{ph}k + 2) \rightarrow k = 0,\ \pm1,\ \pm2,... \tag{2.23}$$

Case 2: c is odd [Sal2004]:

$$\nu = \pm\frac{1}{c}(2m_{ph}k + 1) \rightarrow k = 0,\ \pm1,\ \pm2,... \tag{2.24}$$

In a three-phase machine with sinusoidal current, the harmonic numbers for m_{ph}=3 and q=1/2 can be calculated using Eq. 2.23:

$$\nu = (3k \mp 1) \Rightarrow \nu = (\mp 1, \mp 2, \mp 4, \mp 5, \mp 7, \mp 8, \mp 10, \mp 11, \mp 13, \mp 14....) \tag{2.25}$$

The magnetomotive force for three phases can be written as in Eq. 2.2:

$$\Theta\,(\alpha,t) = \sum_{\nu} \overline{\Theta}\,\left[\cos[\omega\,t - \nu p\alpha] + \cos[\omega\,t + \nu p\alpha]\right], \tag{2.26}$$

where $\overline{\Theta} = \dfrac{3\sqrt{2}}{\pi}\dfrac{N\,\xi_\nu}{\nu p} I$.

The magnetomotive force comprises two opposite waves with an equal speed. The waves, moving in the rotational direction of the rotor, are described as positive.

The stator field is formed from the magnetomotive force $\Theta\,(\alpha,t)$ and the relative permeance $\Lambda_g(\alpha,t)$:

$$b_m(\alpha,t) = \Theta(\alpha,t)\Lambda_g(\alpha,t) = \sum_{\nu} B_{m,\nu}\cos(\nu p\alpha \mp \omega\,t)\,. \tag{2.27}$$

The relative permeance function changes spatially and temporally $\Lambda_g(\alpha,t)$. This function will be discussed later with the saturation and slot effects.

2.3.2 Rotor Field

For the permanent-field synchronous machine, the fundamental frequency of the feeding three-phase system determines the rotor speed:

$$\omega = p\,\Omega\,. \tag{2.28}$$

Here ω is the basic frequency, p the number of pole-pairs of the rotor and Ω the rotor speed.

The electrical frequency of the rotor waves increases with the harmonic number µ of the rotor.

$$\omega_\mu = \mu p \Omega \tag{2.29}$$

The magnetomotive force of the rotor can now be described as follows:

$$\Theta_R(\alpha,t) = \sum_{\mu=1,3,5,...}^{\infty} \overline{\Theta}_R\cos(\mu\alpha p \mp \omega_\mu t + \phi_\mu)\,. \tag{2.30}$$

Here ϕ_μ is the phase angle between the stator and rotor waves with equal ordinal number, μ the ordinal number of rotor harmonics.

The magnets are radially magnetized. Consequently, their magnetic field represents a square wave. Therefore the rotor has only odd ordinal numbers which can be described by a Fourier analysis with uneven sinusoidal waves.

$\mu = (2k \pm 1) \Rightarrow \mu = (1,3,5,7,9,11,13,...)\ k = 0,1,2,3,4,5,6,...$

As with the stator, the rotor field is formed from the magnetomotive force and the magnetic conductivity as follows:

$$b_R(\alpha,t) = \Theta_R(\alpha,t)\Lambda_g(\alpha,t) = \sum_{\mu} B_\mu \cos(\mu p\alpha \mp \omega_\mu t + \phi_\mu)\,. \tag{2.31}$$

2.4 Radial Forces

The total radial forces caused by the entire air gap field are responsible for the definitive noise stimulation. The mechanical noise emission is exhibited if certain harmonic fields interact with each other in the air gap of the machine. Thus radial force waves, acting on the stator, are developed from stator and rotor harmonic fields together. These forces are dependent on many variables, such as the pole-pair number, the rotational frequency and the spatial and temporal variations. These are known by the stimulation variables of the magnetic vibrations and by noise which can be manifested in the structure-borne noise and in the noise emission.

The radial forces, with their ordinal numbers and frequencies, will be explained here, especially for the three-phase machines. An exact derivation of these relations will thus be carried out.

2.4.1 Radial Force Waves

The stator and rotor fields of a three-phase machine with a sinusoidal current will now be examined.

For the stator:

$$b_m(\alpha,t) = \Theta(\alpha,t)\Lambda_g(\alpha,t) = \sum_{\nu} B_m \cos(\nu p\alpha \mp \omega\, t)\,. \tag{2.32}$$

For the rotor:

$$b_R(\alpha,t) = \Theta_R(\alpha,t)\Lambda_g(\alpha,t) = \sum_{\mu} B_\mu \cos(\mu p\alpha \mp \omega_\mu t + \phi_\mu)\,. \tag{2.33}$$

Here, α is the spatial angle, p the pole-pair number, ϕ_μ the phase angle, ν and μ the ordinal harmonic numbers of the stator and rotor respectively, $\omega = 2\pi f$ the angular frequency of the supplied current, and $\Lambda_g(\alpha,t)$ the relative permeance function [Gie2006].

To calculate the surface forces (radial P_{rad} and tangential P_{tan}), the Maxwellian plane stresses on the inner area of the stator must be calculated [Ger1992]:

$$\vec{P} = T\,\vec{n} = \vec{P}_{\tan}\vec{e}_x + \vec{P}_{rad}\vec{e}_y\,, \tag{2.34}$$

$$\vec{n} = \begin{pmatrix} 0 \\ 1 \end{pmatrix} = 0\vec{e}_x + 1\vec{e}_y\,, \tag{2.35}$$

$$T = \frac{1}{2\mu_0}\begin{pmatrix} (b_x^2 - b_y^2) & 2b_x b_y \\ 2b_x b_y & (b_y^2 - b_x^2) \end{pmatrix}, \tag{2.36}$$

where b_x and b_y are the tangential and radial components of the flux density on a radial path in the air gap.

The evaluation yields:

$$T\,\vec{n} = \frac{1}{2\mu_0}\begin{pmatrix} (b_x^2 - b_y^2) & 2b_x b_y \\ 2b_x b_y & (b_y^2 - b_x^2) \end{pmatrix}\begin{pmatrix} 0 \\ 1 \end{pmatrix}$$

$$\Rightarrow T\,\vec{n} = \frac{1}{2\mu_0}\left(2b_x b_y \vec{e}_x + (b_y^2 - b_x^2)\vec{e}_y\right)$$

The radial component P_{rad} can be then expressed by:

$$P_{rad} = \frac{1}{2\mu_0}(b_y^2 - b_x^2) \tag{2.37}$$

and the tangential component P_{tan} by:

$$P_{\tan} = \frac{1}{2\mu_0}2b_x b_y \tag{2.38}$$

The radial force per area (P_{rad}) at time (t) and angle (α) in the air gap can be expressed on the basis of Maxwellian stress tensors as follows:

$$P_{rad}(\alpha,t) = \frac{1}{2\mu_0}\left[b_y^2(\alpha,t) - b_x^2(\alpha,t)\right]. \tag{2.39}$$

The instantaneous value of the normal component of the magnetic flux density in the air gap at a defined point via the angle can be calculated as follows [Gie2006]:

$$b_y(\alpha,t) = \left[\Theta(\alpha,t) + \Theta_R(\alpha,t)\right]\Lambda_g(\alpha,t) = \left[b_m(\alpha,t) + b_R(\alpha,t)\right]. \tag{2.40}$$

Nevertheless, the tangential flux density $b_x(\alpha,t)$ can be neglected in comparison to the radial flux density $b_y(\alpha,t)$; Eq. 2.39 can then be described as follows:

$$P_{rad}(\alpha,t) \approx \frac{b_y^2(\alpha,t)}{2\mu_0} = \frac{1}{2\mu_0}\left[\Theta_m(\alpha,t)+\Theta_R(\alpha,t)\right]^2 \Lambda^2{}_g(\alpha,t)$$

$$= \frac{1}{2\mu_0}\left[\Theta_m^2(\alpha,t)\Lambda^2{}_g(\alpha,t)+2\Theta_m(\alpha,t)\Theta_R(\alpha,t)\Lambda^2{}_g(\alpha,t)+\Theta_R^2(\alpha,t)\Lambda^2{}_g(\alpha,t)\right]$$

$$P_{rad}(\alpha,t) = \frac{\left[b_m(\alpha,t)\right]^2 + 2b_m(\alpha,t)b_R(\alpha,t)+\left[b_R(\alpha,t)\right]^2}{2\mu_0}. \tag{2.41}$$

Based on Eq. 2.41, three groups of the infinite number of radial force waves can be described:

- For one harmonic wave of number ν, τhe product of the stator field $\left[b_m(\alpha,t)\right]^2$ is:

$$P_{rad,\nu}(\alpha,t) = \frac{\left[b_{m,\nu}(\alpha,t)\right]^2}{2\mu_0} = \frac{\left[B_{m,\nu}\cos(\nu p\alpha \mp \omega\, t)\right]^2}{2\mu_0} = \frac{B_{m,\nu}^2}{4\mu_0}\left[1+\cos(2\nu p\alpha \mp 2\omega\, t)\right] \quad (2.42)$$

Equation 2.42 is composed of two mathematical expressions:

a- The static force density $\frac{B_{m,\nu}^2}{4\mu_0}$: this mathematical expression does not have any effect on the vibrations of the structure, as it is uniformly distributed over the air gap.

b- The dynamic force density $\frac{B_{m,\nu}^2}{4\mu_0}\left[\cos(2\nu p\alpha \mp 2\omega\, t)\right]$: its amplitude and frequency are

$$\overline{P}_{rad} = \frac{B_{m,\nu}^2}{4\mu_0},$$

$$\omega_r = 2\omega. \tag{2.43}$$

- For one harmonic wave of number μ, the product of the rotor field $\left[b_{R,\mu}(\alpha,t)\right]^2$ is:

$$P_{rad,\mu}(\alpha,t) = \frac{\left[b_{R,\mu}(\alpha,t)\right]^2}{2\mu_0} = \frac{\left[B_{R,\mu}\cos(\mu p\alpha \mp \omega_\mu t + \phi_\mu)\right]^2}{2\mu_0}$$

$$P_{rad,\mu}(\alpha,t) = \frac{B_{R,\mu}^2}{4\mu_0}\left[1+\cos(2\mu p\alpha \mp 2\omega_\mu t + 2\phi_\mu)\right]. \tag{2.44}$$

Similar to Eq. 2.42, Eq. 2.44 comprises two mathematical expressions:

a- The static force density $\overline{P}_{rad} = \dfrac{B_{R,\mu}^2}{4\mu_0}$

b- The dynamic force density $\dfrac{B_{R,\mu}^2}{4\mu_0}\left[\cos(2\mu p\alpha \mp 2\omega_\mu t + 2\phi_\mu)\right]$: its amplitude and frequency can be described by:

$$\overline{P}_{rad} = \frac{B_{R,\mu}^2}{4\mu_0},$$

$$\omega_r = 2\omega_\mu . \tag{2.45}$$

- The product of the stator and rotor fields $\left[2b_m(\alpha,t)b_R(\alpha,t)\right]$ for the two harmonic numbers ν and μ, is:

$$P_{rad,\nu\mu}(\alpha,t) = \frac{2b_{m,\nu}(\alpha,t)b_{R,\mu}(\alpha,t)}{2\mu_0} = \frac{2B_{m,\nu}\cos(\nu p\alpha \mp \omega\ t)B_{R,\mu}\cos(\mu p\alpha \mp \omega_\mu t + \phi_\mu)}{2\mu_0}$$
$$= \frac{2B_{m,\nu}B_{R,\mu}}{2\mu_0}\left\{\begin{array}{l}\cos\left[(2\nu p\alpha \mp 2\omega\ t) - (\mu p\alpha \mp \omega_\mu t + \phi_\mu)\right] \\ + \\ \cos\left[(2\nu p\alpha \mp 2\omega\ t) + (\mu p\alpha \mp \omega_\mu t + \phi_\mu)\right]\end{array}\right\}$$

$$P_{rad,\nu\mu}(\alpha,t) = \frac{2B_{m,\nu}B_{R,\mu}}{2\mu_0}\left\{\begin{array}{l}\cos\left[p\alpha(\nu - \mu) \mp (\omega\ \ - \omega_\mu)t - \phi_\mu\right] \\ + \\ \cos\left[\ p\alpha(\nu + \mu) \mp (\omega\ \ + \omega_\mu)t + \phi_\mu\right]\end{array}\right\}. \tag{2.46}$$

The force amplitude is: $\overline{P}_{rad} = \dfrac{2B_{m,\nu}B_{R,\mu}}{2\mu_0}$

and the frequency is:

$$\omega_r = \omega \pm \omega_\mu . \tag{2.47}$$

The following trigonometric functions are used to show Eq. 2.42, 2.44 and 2.46 in their last forms:

$\cos^2\alpha = 0.5(1 + \cos 2\alpha)$ and $2\cos\alpha\cos\beta = \cos(\alpha - \beta) + \cos(\alpha + \beta)$.

2.4.2 Modes and Frequencies of the Radial Force Waves

According to Eq. 2.42, 2.44 and 2.46, the radial force density can be generally described as follows:

$$P_{rad}(\alpha,t)=\overline{P}_{rad}\cos(r\alpha-\omega_r t)\,. \tag{2.48}$$

Here, (r) is the number of modes, $\overline{P}_{rad}$ the amplitude of the radial force and ω_r the frequency of the force wave.

- Stator harmonics with the ordinal number ν:

  According to Eq. 2.43, the frequency of the radial force doubles the fundamental frequency:

$$f_r=2f \tag{2.49}$$

  The modes can be described according to Eq. 2.48:

$$r=2\nu p \tag{2.50}$$

  The modes in a three-phase machine can also be described in relation to the number of teeth and pole-pairs.

  For q=1/2:

  $\nu=3k\pm1$ and $q=\dfrac{Z}{m_{ph}\times 2p}=\dfrac{Z}{6p}=\dfrac{1}{2}\Rightarrow\dfrac{Z}{p}=3$

$$\Rightarrow \nu=3k\pm1=(k\frac{Z}{p}\pm1)\,. \tag{2.51}$$

  For q=1:

  $\nu=6k\pm1$ and $q=\dfrac{Z}{m_{ph}\times 2p}=\dfrac{Z}{6p}=1\Rightarrow\dfrac{Z}{p}=6$

$$\Rightarrow \nu=6k\pm1=(k\frac{Z}{p}\pm1)\,. \tag{2.52}$$

  Eq. 2.51 and 2.52 then result for:

$$r=2\nu p=2(kZ\pm p)\,. \tag{2.53}$$

  Here k is an integer.

- Rotor harmonics with the ordinal number μ:

  The rotor slots in the PM machine equalize the pole number 2p, which means that the angular frequencies of the rotor harmonics can be expressed as follows:

$$\omega_\mu = \omega \pm 2pk\Omega \ = \omega \pm 2pk\frac{\omega}{p} = \omega \pm 2k\omega = \omega(1 \pm 2k)\,. \tag{2.54}$$

According to Eq. 2.45, 2.47 and 2.54, the frequencies and modes are calculated as follows:

$$f_r = 2(1 \pm 2k)f\,, \tag{2.55}$$

and

$$r = 2\mu p = 2p(1 \pm 2k)\,. \tag{2.56}$$

- Interaction of the stator and rotor harmonics:

  The "product of the stator and rotor fields" will result in a subgroup, which can describe the interaction of the stator and rotor harmonics. According to Eq. 2.47, the angular frequencies of this subgroup are expressed as follows:

$$\omega_r = \omega \pm \omega_\mu = \omega \pm \omega \pm 2pk\Omega = \omega \pm \omega \pm 2k\omega$$

$$\omega_r = \omega \pm \omega(1 + 2k)\,. \tag{2.57}$$

The frequencies and modes can be expressed as follows:

$$f_r = f \pm f(1 + 2k)\,, \tag{2.58}$$

or $f_r = 2(1 + k)f$ and $f_r = 2kf$

$$r = (\nu \pm \mu)p = kZ \pm 2p(k + 1)\,. \tag{2.59}$$

The groups of the radial force waves as well as their amplitudes, frequencies and modes are summarized in Tab. 2-1.

	Radial force waves		
Group	Amplitude ($\overline{P}_{rad}$)	Frequency (f_r)	Mode (r)
Product of stator space harmonics of the same number ν	$\overline{P}_{rad} = \frac{B_m^2}{4\mu_0}$	$f_r = 2f$	$r = 2\nu p = 2(kZ \pm p)$
Product of rotor space harmonics of the same number μ	$\overline{P}_{rad} = \frac{B_R^2}{4\mu_0}$	$f_r = 2f_\mu$ $f_r = 2(1 \pm 2k)f$	$r = 2\mu p = 2p(1 \pm 2k)$
Product of stator and rotor space harmonics (general)	$\overline{P}_{rad} = \frac{B_m B_R}{2\mu_0}$	$f_r = f \pm f_\mu$	$r = (\nu \pm \mu)p$
Product of stator winding and rotor space harmonics, where: $\nu = (kZ/p) \pm 1 = 3k \pm 1$ $\mu = 2k \pm 1$	$\overline{P}_{rad,\nu\mu} = \frac{B_{m\nu} B_{R\mu}}{2\mu_0}$	$f_r = f \pm f(1+2k)$	$r = kZ \pm 2p(1+k)$

Table 2-1: The radial forces with their amplitudes, frequencies and modes

If the amplitude $\overline{P}_{rad}$ is multiplied by the expression ($D_{in}L_i$), the radial forces are calculated in Newton; here, D_{in} and L_i are the inner diameter of the stator and the length of the stator, respectively.

2.4.3 Effect of the Stator Slotting on the Radial Force Waves

Until now, the theory has been presented under the assumption of a smooth stator surface. The existence of the stator slots disturbs the rotor field or the entire air gap field and this can significantly increase the vibration or noise in the machine. The slot opening or the air between two pole shoes of adjoining teeth leads to a highly asymmetrical reluctance distribution at the air gap.

However, the difference in reluctance can influence the air gap field in two ways:

1) The entire pole flux is reduced, as the effective air gap width is increased. This effect is taken into account by using the Carter factor (K_c); the geometrical dimensions of the air gap are projected in an ideal air gap of a quasi-homogenous field using the Carter factor:

$$K_c = \frac{s_1}{s_1 - \gamma\, g_{nom}}. \tag{2.60}$$

Here $s_1 = s \times R_s = (2\pi / Z) \times R_s$ is the slot pitch length, R_s the inner radius of the stator, g_{nom} the geometrical air gap, and γ the slot factor:

$$\gamma = \frac{4}{\pi}\left[\frac{1}{2}\kappa \arctan\left(\frac{1}{2}\kappa\right) - \ln\sqrt{1+\left(\frac{\kappa}{2}\right)^2}\right], \tag{2.61}$$

whereby $\kappa = b_s / g_{nom}$ is the relative slot opening [Ric1967].

The effective air gap for buried permanent magnet motors is then: $g' = g_{nom} \times K_c$ [Gie2006].

2) Additional harmonics in the air gap field appear when the distribution of the flux in the air gap changes. This effect is taken into account by considering the relative permeance of the air gap $\Lambda_g(r,\alpha)$.

   The permeance function can be introduced according to [Zhu1993] as follows:

$$\overline{\Lambda}_g(r,\alpha) = \left\{ \begin{array}{l} \Lambda_0\left[1-\beta_r-\beta_r\cos\dfrac{\pi}{0.8\alpha_0}\alpha\right] \;\; for \;\; 0 \le \alpha \le 0.8\alpha_0 \\ \Lambda_0 \;\; for \;\; 0.8\alpha_0 \le \alpha \le \alpha_t/2 \end{array} \right\}. \tag{2.62}$$

   Here $\Lambda_0 = \mu_0 / g'$ is the constant component of the air gap relative permeance, $\alpha_0 = b_s / R_s$, and $\alpha_t = s / R_s$ [Zhu1993]. The relative permeance function $\Lambda_g(r,\alpha)$ is:

$$\Lambda_g(r,\alpha) = \frac{\overline{\Lambda}_g(r,\alpha)}{\Lambda_0} = \frac{\overline{\Lambda}_g(r,\alpha)}{\mu_0 / g'}. \tag{2.63}$$

   This function varies spatially and also in a radial direction.

   The function β_r expresses, for each radius (*r*), the ratio between B_0 and B_{max} [Cra2005]:

$$\beta_r = \frac{B_{0(r)}}{B_{\max(r)}} = \frac{B_{\max(r)} - B_{\min(r)}}{2B_{\max(r)}}, \tag{2.64}$$

   and can be calculated by:

$$\beta_r = \frac{1}{2}\left(1 - \frac{1}{\sqrt{1+\kappa^2(1+\nu^2)}}\right), \tag{2.65}$$

   whereby the variable (ν) results iteratively from:

$$y_s\frac{\pi}{b_s} = \frac{1}{2}\ln\left[\frac{\sqrt{a^2+\nu^2}+\nu}{\sqrt{a^2+\nu^2}-\nu}\right] + \frac{2}{\kappa}\arctan\frac{2}{\kappa}\frac{\nu}{\sqrt{a^2+\nu^2}}, \tag{2.66}$$

with $a=1+\left(\frac{2}{\kappa}\right)^2$, $y_s=r-R_s+g'$ for inside-rotor machines and $y_s=R_s+g'-r$ for outside-rotor machines.

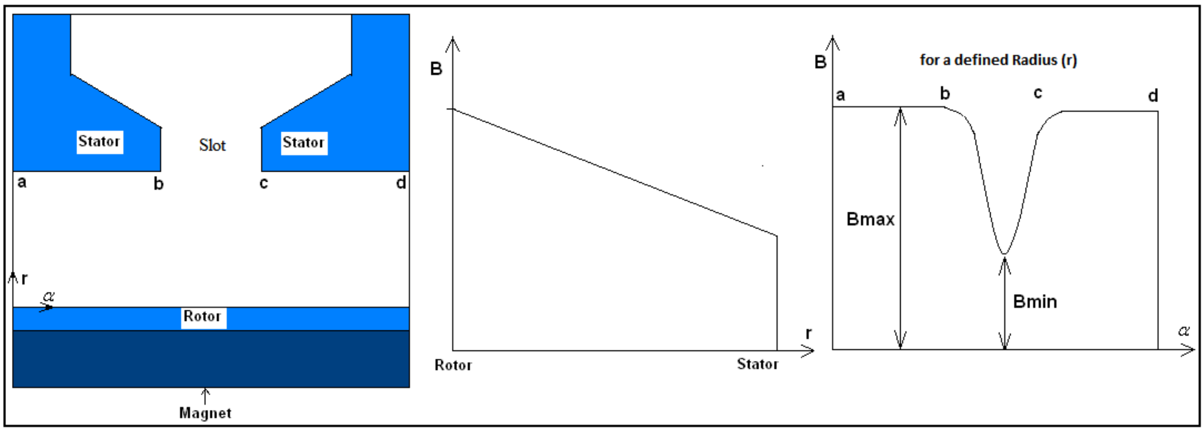

Figure 2-6: Rotor field in the air gap

The relative permeance function of the air gap can be also described in the form of Fourier series [Zhu1993]:

$$\Lambda_g(r,\alpha)=\Lambda_0\sum_{k=0,1,2,3...}^{\infty}A_k(r)\cos(kZ\alpha)\,, \tag{2.67}$$

where A_k can be expressed as follows:

$$\begin{aligned}A_0(r)&=\frac{1}{K_c}\left(1-1.6\beta_r\frac{b_s}{s}\right)\\ A_k(r)&=-\beta_r\frac{4}{k\pi}\left[0.5+\frac{\left(\frac{kb_s}{s}\right)^2}{0.78125-2\left(\frac{kb_s}{s}\right)^2}\right]\sin\left(1.6\pi\frac{kb_s}{s}\right).\end{aligned} \tag{2.68}$$

As mentioned before, the relative permeance varies radially from the middle of a slot opening in the stator onto the rotor (see Fig. 2-6) [Zhu1993].

The effect of the stator slots on the rotor field can be considered by the relative permeance function. The rotor field can then be described by the product of the magnetomotive force $\Theta_R(\alpha,t)$ and the relative permeance function $\Lambda_g(r,\alpha)$:

$$b_R(\alpha,t)=\Theta_R(\alpha,t)\Lambda_g(r,\alpha)=\Lambda_0\sum_{\mu}\overline{\Theta}_R\cos(\mu p\alpha\mp\omega_\mu t+\phi_\mu)\sum_{k=1,2,3}A_k\cos(kZ\alpha)$$

$$b_R(\alpha,t)=\frac{1}{2}\Lambda_0\sum_{\mu}\sum_{k}A_k\overline{\Theta}_R\cos\left[(\mu p\pm kZ)\alpha\mp\omega_\mu t+\phi_\mu\right]. \tag{2.69}$$

The radial force density on the stator due to the rotor μth and stator permeance k^{th} harmonics is [Gie2006]:

$$\begin{aligned}P_{rad,\mu\,k}(\alpha,t)&=\frac{\left[b_R(\alpha,t)\right]^2}{2\mu_0}=\frac{1}{2\mu_0}\left\{\frac{1}{2}\Lambda_0\Theta_R A_k\cos\left[(\mu p\pm kZ)\alpha\mp\omega_\mu t+\phi_\mu\right]\right\}^2\\ P_{rad,\mu\,k}(\alpha,t)&=\frac{1}{8\mu_0}\Lambda^2{}_0\Theta_R^2A_k^2\left\{1+\cos\left[2(\mu p\pm kZ)\alpha\mp 2\omega_\mu t+2\phi_\mu\right]\right\}.\end{aligned} \tag{2.70}$$

Similar to the cogging torque, the radial forces arise not only when the stator is supplied with current, but also at zero current. The most important modes of the radial forces $P_{rad}(\alpha,t)$, on account of the slot openings in the stator, are the low even modes $r=2,4,6,8$ with the ordinal number of the relative permeance function k = 1. Based on this consideration, a new group of radial force waves is derived, which includes the effect of the stator slots on the rotor field.

	Radial force waves		
Group	Amplitude ($\overline{P}_{rad}$)	Frequency (f_r)	Mode (r)
Effect of the stator slots on the rotor field	$\frac{\Lambda^2{}_0\Theta_R^2A_k^2}{8\mu_0}$	$f_r=2\mu f$	$r=2(\mu p\pm Z)$

Table 2-2: Radial force waves from the effect of the stator slots on the rotor field

Stator slot opening undermagnetic saturation

Due to the slot opening in the stator, the air gap field is suppressed to pass through the tooth tips. Consequently, the tooth tips become highly saturated. This effect can be regarded by increasing the slot opening from b_s to b_{sat} (see Fig. 2-7).

The supposed slot opening b_{sat} is a periodic function with a duration (π/p), and has a frequency twice that of the fundamental frequency. It can therefore be described by the first and second components of Fourier series as follows [Gie2006]:

$$b_{sat}=b_{mean}-b_{s1}\cos[2(p\alpha-\omega t)], \tag{2.71}$$

where b_{mean} is the mean value of the slot opening along the pole pitch, and ($b_{s1} = b_{mean} - b_s$) the amplitude of the first harmonic in b_{sat}.

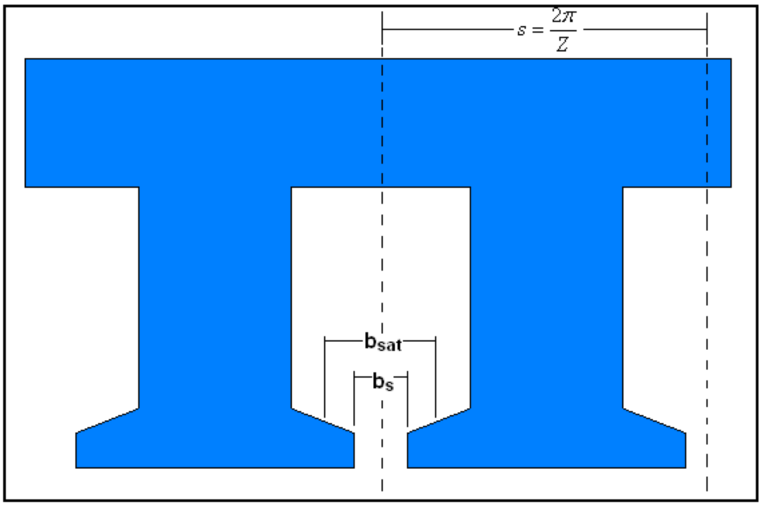

Figure 2-7: The equivalent slot opening " b_{sat}" upon saturation of the tooth tips

Air gap fields under magnetic saturation:

In order to consider the effect of the magnetic saturation into the stator and rotor fields in the air gap, the relative permeance has to be expressed with respect to the magnetic saturation. According to [Gie2006], the air gap permeance including the magnetic saturation effect can be expressed as follows:

$$\Lambda\ (\alpha,t) \approx \Lambda_0 + \Lambda_{sat}(\alpha,t)\,, \tag{2.72}$$

whereby $\Lambda_{sat}(\alpha,t)$ is:

$$\Lambda_{sat}(\alpha,t) = -\overline{\Lambda}_{sat}\cos(2p\alpha - 2\omega t - 2\phi_s)\,. \tag{2.73}$$

Considering only the magnetomotive force of the fundamental wave, the stator field can be expressed by using the relative permeance function $\Lambda_{sat}(\alpha,t)$ as follows:

$$b_{sat}(\alpha,t) = \Theta_1(\alpha,t)\Lambda_{sat}(\alpha,t) = -\overline{\Theta}_1\cos(p\alpha - \omega\, t)\overline{\Lambda}_{sat}\cos(2p\alpha - 2\omega t - 2\phi_s)$$

$$= -\frac{1}{2}\overline{\Theta}_1\overline{\Lambda}_{sat}\cos(-p\alpha + \omega\, t + 2\phi_s) - \frac{1}{2}\overline{\Theta}_1\overline{\Lambda}_{sat}\cos(3p\alpha - 3\omega\, t - 2\phi_s)$$

$$b_{sat}(\alpha,t) = -B_{sat,v}\left\lfloor\cos(-p\alpha + \omega\, t + 2\phi_s) - \cos(3p\alpha - 3\omega\, t - 2\phi_s)\right\rfloor, \tag{2.74}$$

whereby $B_{sat} = \overline{\Theta}_1\overline{\Lambda}_{sat}/2$.

The two waves of the stator field in Eq. 2.74 take account of the saturation effect in the teeth and yoke. However, the first wave progresses with the fundamental frequency and the second wave has three times the fundamental frequency.

$$b_m = b_{sat}(\alpha,t) = -B_{sat,\nu}\left[\cos(-p\alpha+\omega\, t+2\phi_s)-\cos(3p\alpha-3\omega\, t-2\phi_s)\right]. \qquad (2.75)$$

The rotor field under saturation can be described as follows [Gie2006]:

$$b_R(\alpha,t) = \sum_{\mu} B_{sat,\mu}\cos(\mu p\alpha-\omega_\mu t-2\phi_\mu)\,. \qquad (2.76)$$

According to Eq. 2.54, the rotor frequency is derived in case of saturation for:

$$\begin{gathered}\omega_\mu = 3\omega \pm 2pk\Omega_m = 3\omega \pm 2pk\frac{\omega}{p},\\ \omega_\mu = \omega(3\pm 2k).\end{gathered} \qquad (2.77)$$

The effect of the saturation on the product of the rotor and stator fields gives rise to a new group of radial force waves, whereby their frequencies and modes are expressed as follows:

$$\omega_{rsat} = \omega \pm \omega_\mu = \omega \pm \omega(3\pm 2k)\,, \qquad (2.78)$$

or

$$\omega_{rsat} = \omega + \omega(3+2k) = 2(2+k)\omega \quad \text{and}\; \omega_{rsat} = \omega - \omega(3-2k) = 2(1+k)\omega\,.$$

Then the frequencies and modes result into:

$$f_{rsat} = f \pm f_\mu = f \pm f(3\pm 2k)\,, \qquad (2.79)$$

$$r = (\nu \pm \mu)p = (k\frac{Z}{P} \pm 1 + 3 \pm 2k)p\,, \qquad (2.80)$$

or

$$r = kZ + 2kp + 4p \;\text{ and }\; r = kZ - 2kp + 2p\,.$$

	Radial force waves		
Group	Amplitude ($\overline{P}_{rad}$)	Frequency (f_r)	Mode (r)
Saturation effect on stator and rotor fields	$\overline{P}_{rad} = B_{sat,\mu}B_{sat,\nu}$	$f_{rsat} = f \pm f_\mu$ $f_{rsat} = f \pm f(3\pm 2k)$	$r = (\nu \pm \mu)p$ $r = (k\frac{Z}{P} \pm 1 + 3 \pm 2k)p$

Table 2-3: Radial force waves based on the saturation effect in the stator

2.4.4 Effect of the Eccentricity

The temporal and spatial changes in the air gap are derived from:

$$g(\alpha,t) = R - r - e\cos(\alpha - \omega_\varepsilon t) = g_{nom}[1 - \varepsilon\cos(\alpha - \Omega_\varepsilon t)]\,. \tag{2.81}$$

In g_{nom} = R-r, R is the inner radius of the stator and r the outer radius of the rotor.

The relative eccentricity is defined in:

$$\varepsilon = \frac{e}{g_{nom}}\,,$$

whereby e is the rotor eccentricity and g_{nom} the geometrical constant air gap with e=0.

With $\Omega_\varepsilon = 0$ a static eccentricity from Eq. 2.81 is discernible. The dynamic eccentricity for synchronous motors can be expressed as $\Omega_\varepsilon = \frac{\omega}{p} = 2\pi\frac{f}{p}$.

The change in the air gap has a direct influence on the resultant relative permeance function $\Lambda_g(\alpha,t)$. For more information, the derivations of the relative permeance function and the flux density for this case are clearly described in [Gie2006].

The frequencies of the radial forces based on the eccentricity can be expressed as follows, for the static eccentricity:

$$f_{r\varepsilon} = 2f(1+k)\,, \tag{2.82}$$

or

$$f_{r\varepsilon} = 2f\,k\,, \tag{2.83}$$

and for the dynamic eccentricity:

$$f_{r\varepsilon} = f\left[2(1+k) \pm \frac{1}{p}\right], \tag{2.84}$$

or

$$f_{r\varepsilon} = f\left[2k \pm \frac{1}{p}\right]. \tag{2.85}$$

The essential modes for both cases are: r = 1 and r=2, which can be excited simply due to their lower frequencies.

2.5 Analytical Considerations Regarding Three-Phase Machines

A PM-machine, where p=10 und Z=30, is analyzed and its electromagnetic noise behavior is evaluated according to the given equations. The number of pole-pairs of the stator (p_s) is equal to the number of pole-pairs of the rotor:

$p_s = Z / nm_{ph} = 30/3 = 10$

The number of coils per zone (n) in this case is: $n = 1$

The rotor field moves in the rotational direction of the rotor and its harmonics are then designated by positive signs. During open circuit mode, only the rotor harmonics appear in the air gap, since the supplied current is zero. The frequencies and modes of the air gap waves for this case are shown in Table 2-4.

	k	0	1	2	3	4	5	6	7
Open Circuit	Rotor harmonics $\mu = 1 \pm 2k$	1	3 -1	5 -3	7 -5	9 7	11 -9	13 -11	15 -13
	Frequency factor $f_r / f = 2(1 \pm 2k)$	2	6 -2	10 -6	14 -10	18 -14	22 -18	26 -22	30 -26
	Modes $r = 2\mu p$	20	60	100	140	180	220	260	300

Table 2-4: Frequencies and modes of the air gap field during idling

In normal operation, the stator and rotor harmonics interact with each other and define the air gap harmonics. For the studied PM-machine, the stator and rotor ordinal harmonic number are ν=3k±1 and μ=2k±1, respectively. The frequencies and modes are determined according to Table 2-1. The results are shown in Table 2-6. The number of pole-pairs is the common factor between the modes and their frequency factors for all harmonics.

	k	0	1	2	3	4	5	6	7
Effect of stator harmonics with rotor harmonics	Rotor harmonics $\mu = 2k \pm 1$	1	3 1	5 3	7 5	9 7	11 9	13 11	15 13
	Stator harmonics $\nu = k(Z/p) \pm 1$	1	4 2	7 5	10 8	13 11	16 14	19 17	20 18
	Frequency factor $f_r / f = 2(1 + k)$	2	4	6	8	10	12	14	16
	Modes $r = kZ + 2p(k+1)$	20	70	120	170	220	270	320	370
	Frequency factor $f_r / f = 2k$	0	2	4	6	8	10	12	14
	Modes $r = kZ - 2p(k+1)$	-20	-10	0	10	20	30	40	50

Table 2-5: Frequencies and modes resulting from the interaction of the stator and rotor harmonics

According to Tab. 2-5, mode “0” has appeared with a frequency factor of 4. The frequency of this radial force wave can lead to a resonance in the stator structure when it matches the natural frequency f_0 of mode “0”.

$$f_r = 4f \ , \tag{2.86}$$

where f_r is the frequency of the radial force harmonic and f is the electrical frequency.

For the studied machine f_0 is:

$f_0 = 4150Hz$:

A resonance can occur if the frequency of a radial force wave encounters a natural frequency of the stator:

$f_0 = f_r$;

Based on Eq. 2.86:

$f_r = 4f = 4 \times p \times f_m = 40 f_m$,

where p is the number of pole-pairs and f_m is the mechanical frequency.

The mechanical frequency can then be calculated as follows:

$$f_0 = 4150Hz, \ f_0 = 4f = 40 f_m = 4150Hz \Rightarrow f_m = \frac{4150Hz}{40} = 103.75Hz.$$

The mechanical frequency in rpm can be then calculated as follows:

$$f_m = 103.75Hz \times 60(s/\min) = 103.75 \times (1/s) \times 60(s/\min) = 6225 \times (1/\min) = 6225\text{rpm}.$$

In this studied case, the maximum allowed rotational speed is related to the maximum rotational speed of the transmission, which is 7200 rpm. This is because the PM-machine is connected directly to the transmission shaft by means of a clutch.

The mechanical frequency f_m of mode zero is less than the maximum allowed rotational speed: f_m=6225rpm < 7200rpm. This means that mode zero can be excited.

2.6 Numerical Calculation of the Magnetic Forces

Due to the complex geometry of an interior permanent magnet synchronous machine, the analytical calculation methods limit the extent to which the electromagnetic field distribution can be determined with a fine spatial resolution. In contrast to the analytical calculation, the finite element method is used to model the complex geometries by performing numerical computations. Consequently, the determination of the flux trend or, rather, the magnetic forces and their waves in the air gap, is accurately performed by using the **F**inite **E**lement **M**ethod (FEM).

The simulations are realized statically in a 2D space model. As a result, the spatial and temporal curves for the radial forces are determined. For every static simulation, the rotor increment is 6° electrically. In order to cover an electrical period, a total of 60 different positions of rotor or rather simulations are performed for one operating point.

The magnetic symmetrical part in the electric machine plays an important role in the **F**inite **E**lement (FE) simulation. It represents a geometrical part which repeats itself along the circumference of the machine. The FE simulation of one magnetic symmetrical model covers the whole machine and carries out all the information that is required in the investigation of electromagnetic noise for electric motors (see Fig. 2-8).

The operating point (Id=0 and Iq=277.6 Arms) is chosen for the simulations, as the rotor harmonics were not diminished by the direct current “Id”.

The simulation procedures in FEM involve the following steps:

1- Modeling and specifying materials such as iron, magnet and copper (pre-processing)

2- Specifying loads and boundary conditions and running the solution process (solving)

3- Evaluation of the solution and calculation of derived variables (post-processing)

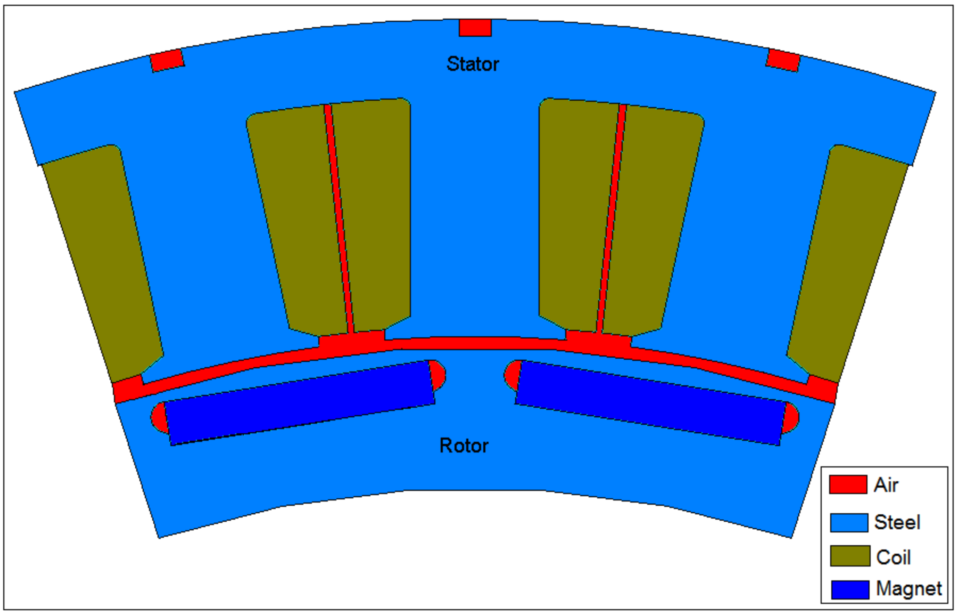

Figure 2-8: The magnetic symmetry corresponds to a pole-pair of the machine

2.6.1 Flux Density in the Air Gap

The FE simulation allows extracting of the radial and tangential air gap fields directly from the FE simulation along a path in the air gap. As shown in Fig. 2-9, it can be discerned that the amplitude of the tangential flux density is significantly less than the radial flux density. By looking at the flux curve, the width of the tooth can be recognized.

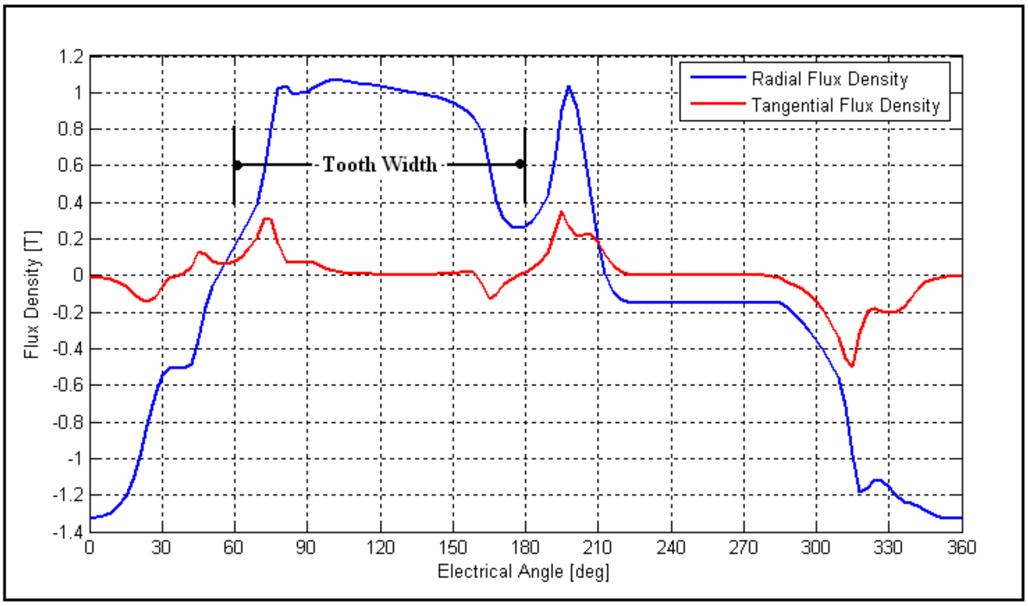

Figure 2-9: Radial and tangential flux density from FE simulation

The spatial representation of the flux components in Fig. 2-10 illustrates the strength of the first harmonic. The resolution of the first ten Fourier coefficients is carried out here for a magnetic symmetrical sector (one pole-pair).

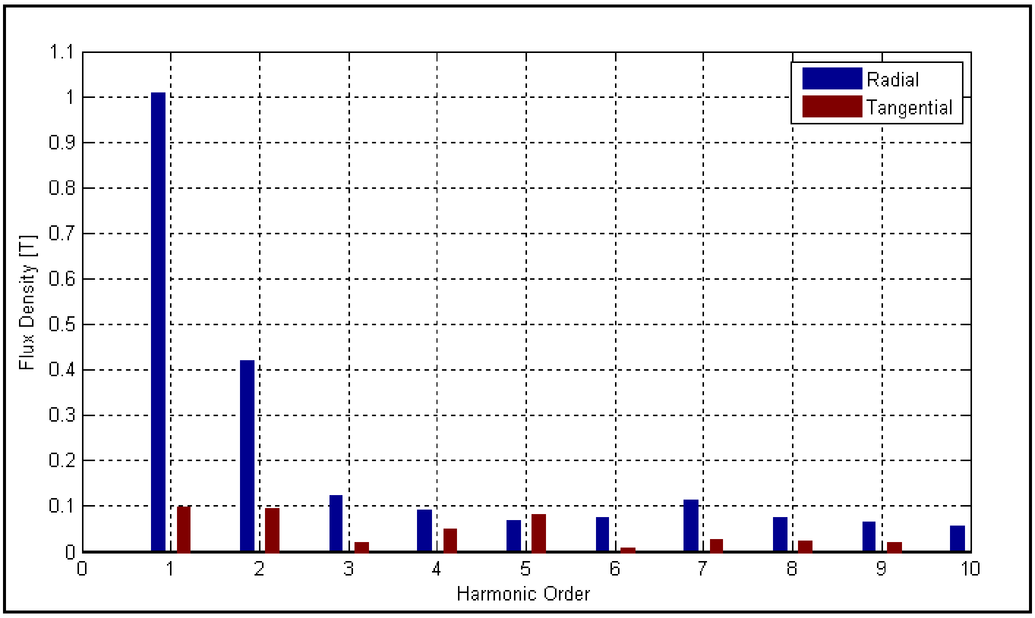

Figure 2-10: Fourier coefficients of the flux density

2.6.2 Spatial Distribution of the Radial Forces

For the analysis of vibrations and noise, it is important to determine the spatial distribution as well as the time dependence of the radial force or stress.

To describe the spatial and temporal functions, the general form of the radial stress can be used:

$$P_{rad}(\alpha,t)=\sum_r \overline{P}_{rad}\cos(r\alpha-k\omega t)\,. \tag{2.87}$$

The radial force per unit area at time (t) and angle (α) comprises an infinite number of harmonic waves. At an instant of time, the radial stress equation can be simplified to:

$$P_{rad}(\alpha)=\sum_r \overline{P}_{rad}\cos(r\alpha-\phi)\,, \tag{2.88}$$

where ϕ is a constant.

Expanding Eq. 2.88in Fourier series gives:

$$P_{rad}(\alpha)=\sum_{r=0}^{\infty}\overline{P}_{rad}\cos(r\alpha-\phi)=a_0+\sum_{r=1}^{\infty}a_n\cos r\alpha+\sum_{r=1}^{\infty}b_n\sin r\alpha\,. \tag{2.89}$$

Equation 2.89 can also be written as:

$$P_{rad}(\alpha)=a_0+\sum_{r=1}^{\infty}a_n\cos r\alpha+\sum_{r=1}^{\infty}b_n\sin r\alpha=\sum_{r=0}^{\infty}a_n\cos r\alpha+\sum_{r=0}^{\infty}b_n\sin r\alpha\,. \tag{2.90}$$

For an arbitrary instant of time, Eq. 2.87 can be used again where the time is included as an additional parameter. In this case, the radial stress equation has to be developed into a two dimensional Fourier series as follows:

$$P_{rad}(\alpha,t)=\sum_r \overline{P}_{rad}\cos(r\alpha-\omega_r t)=\sum_{r=0}^{\infty}a_n\cos r\alpha+\sum_{r=0}^{\infty}b_n\sin r\alpha\,, \tag{2.91}$$

where the coefficients $a_n(t)$ and $b_n(t)$ are periodic functions and can be also expanded into Fourier series as follows:

$$a_n(t)=\sum_{r=0}^{\infty}c_{r,k}\cos k\omega t+\sum_{r=0}^{\infty}d_{r,k}\sin k\omega t\,, \tag{2.92}$$

$$b_n(t)=\sum_{r=0}^{\infty}e_{r,k}\cos k\omega t+\sum_{r=0}^{\infty}f_{r,k}\sin k\omega t\,. \tag{2.93}$$

If Eq. 2.92 and Eq. 2.93 are integrated into Eq. 2.91, then the radial stress equation can be expressed as:

$$P_{rad}(\alpha,t)=\sum_{r=0}^{\infty}\sum_{k=0}^{\infty}g_{r,k}\cos(-r\alpha+k\omega t+\gamma_+)+\sum_{r=0}^{\infty}\sum_{k=0}^{\infty}h_{r,k}\cos(r\alpha+k\omega t+\gamma_-)\,, \tag{2.94}$$

where the constants $g_{r,k}$ and $h_{r,k}$ are described as functions of $c_{r,k}$, $d_{r,k}$, $e_{r,k}$ and $f_{r,k}$ (see [Bel2004]).

According to Eq. 2.94, each force wave is composed of two locally spatially force waves which rotate in different directions. One wave rotates in the rotor direction and is designated by a phase parameter γ_+ and the other wave rotates in the opposite direction and is also designated by a phase parameter γ_-.These two waves are called orthogonal force waves or modes and can be also be described by cosine and sine components for each mode.

The flux density values are calculated from the FEM computation along a path in the middle of the air gap; this path has been divided into 121 points. The radial and tangential flux densities are calculated at each point. The FEM results of the flux densities are read by a MATLAB-script, so that the radial and tangential forces are then computed in Newton by integrating the force densities (N/m^2) along the defined path and multiplying them by the axial length of the machine (see Fig. 2-11). The force densities can be also used as pressure forces in the dynamic and structural simulations.

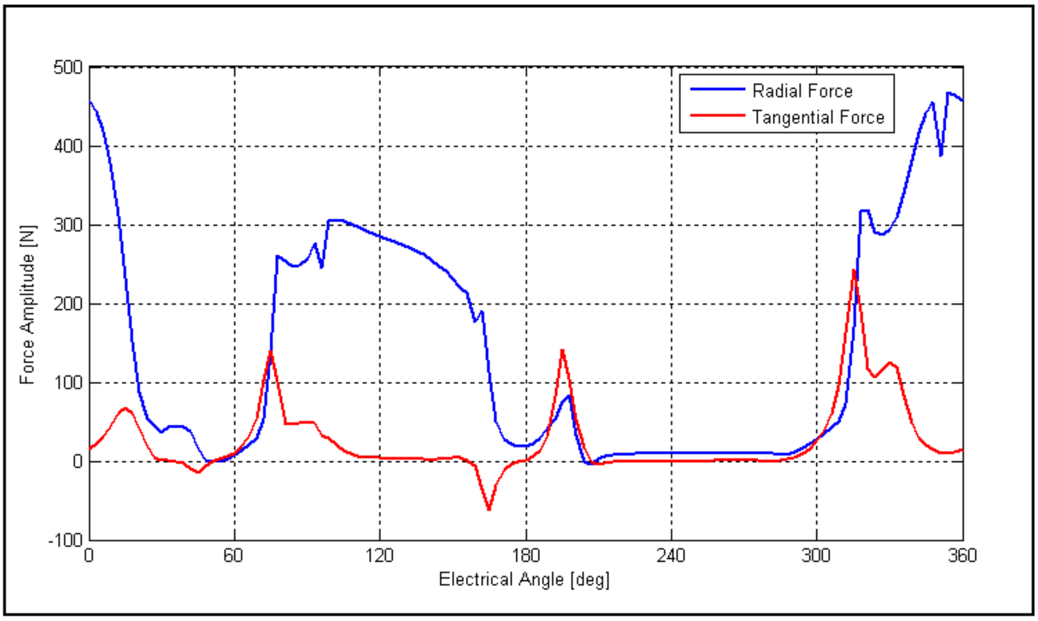

Figure 2-11: Radial and tangential forces in the air gap.

A Fourier decomposition of the radial force, taken at one instant of time, is represented in Fig. 2-12. These spatial harmonic waves can restore the original curve of the radial force if they are superposed (see Fig. 2-13).

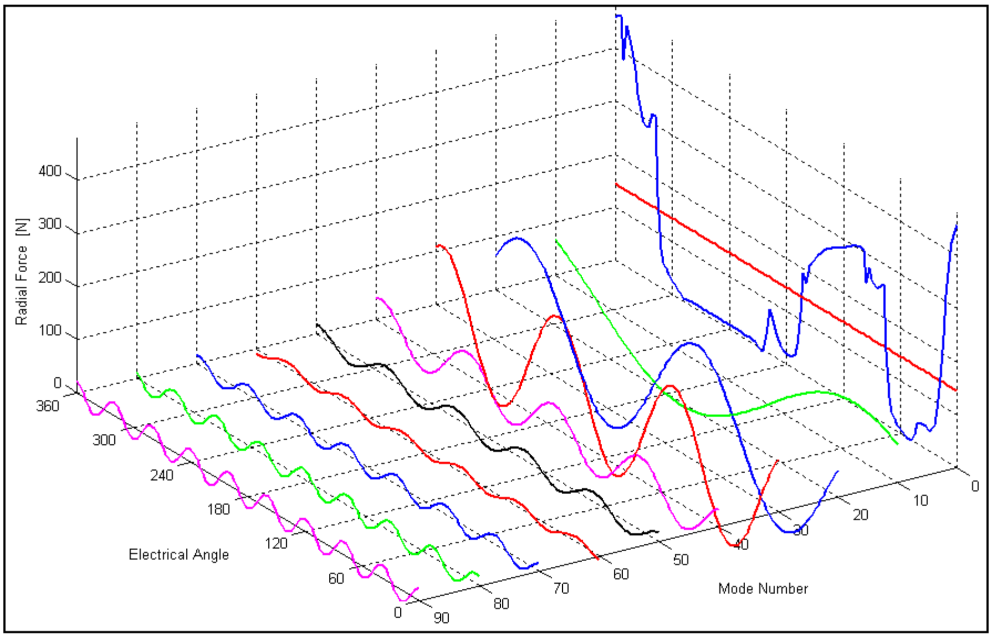

Figure 2-12: Decomposition of the original radial force curve into harmonics

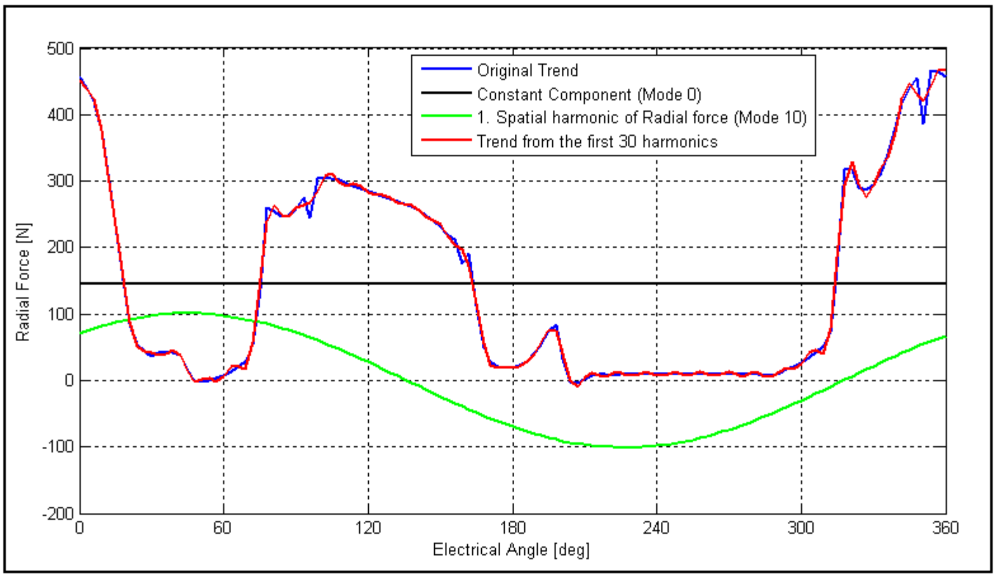

Figure 2-13:Restoring the radial force curve using the first 30 harmonics

The aim of the spatial representation is to state which vibration modes are excited with respect to the electromagnetic design of the electric machine. The recognition of the dominant vibration modes is very useful in the dynamic investigation of the structure. Here, the first spatial harmonic in Fig. 2-13 is actually repeated for each pole-pair (symmetrical sector) along the circumference of the stator; this can yield a vibration mode 10 for the studied machine. In addition to that, if the constant component of the Fourier series is plotted along the stator, a zero vibration mode will appear. These two modes are then the most dominant modes because they represent the first two harmonics of the radial force with the smaller electrical frequencies. In Fig. 2-14, these two modes are described by their orthogonal waves according to Eq. 2-94.The force amplitudes of each mode and their resulting deflections in the structure of the electric machine will be discussed in the following chapters.

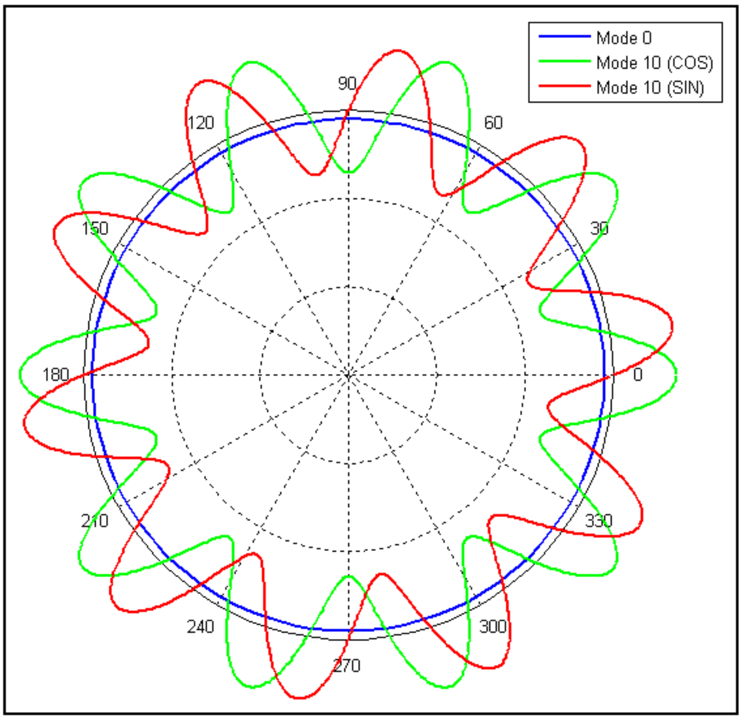

Figure 2-14: The Orthogonal waves of modes “0” and “10”

2.6.3 Recalculation of the Torque

The torque is related to the tangential forces by the radius of the rotor. As a result, the calculation method for the magnetic forces in Newton can be checked by recalculating the torque and comparing it with the torque value T_{FEM} given directly by the FEM-Software. The tangential force over one pole-pair can be calculated by integrating the element forces on a path along one pole-pair (symmetrical sector). The total tangential force over the circumference of the rotor can then be obtained by multiplying the tangential force of one pole-pair (one symmetrical sector) by the number of pole-pairs (number of symmetrical sectors) of the machine.

The tangential force from Fig. 2-11 yields to:

$$Ft_{pp} \approx 230N$$

$$Ft_{rotor} = Ft_{pp} \times p \approx 230N \times 10 \approx 2300N$$

The torque is then derived as:

$$M_{\max} = Ft_{rotor} \times Radius_{rotor} \approx 2300N \times 0.1135m \approx 261\,\text{Nm.}$$

However, the torque obtained directly from the FEM software for this operating point is:

T_{FEM} = 255Nm.

2.6.4 Temporal Representation of the Radial Forces

The current in the coils causes a fluctuation in the amplitudes of the radial forces. This temporal fluctuation excites the stator of the electric machine and leads to a definite mechanical vibration response. In the electromagnetic FEM-computations for the temporal representation, the current flows through the coils with a full electric period by a fixed rotor position. The FEM-computations are repeated at various rotor positions along a pole-pair (or along magnetic symmetrical sector). The FEM-results are therefore processed and the temporal curve of the radial forces is deduced. In order to show the temporal representation along one pole-pair (see Fig. 2-15), the results of 60 static simulations at different rotor positions are presented together.

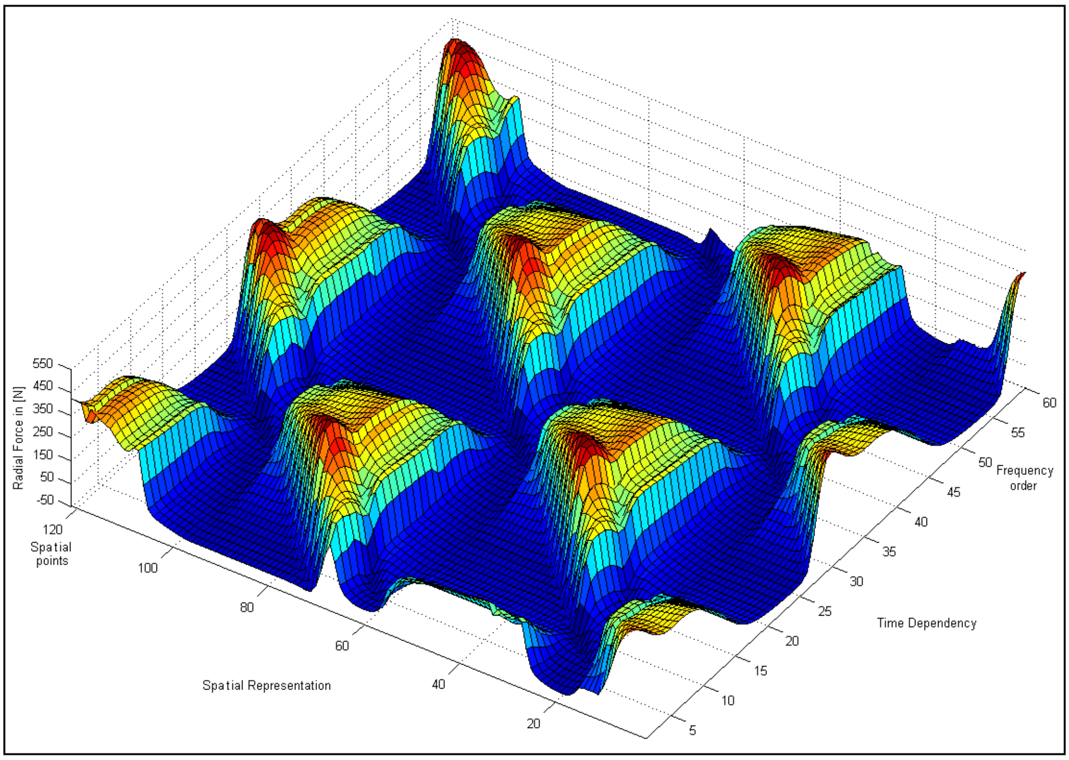

Figure 2-15: 3D force representation in temporal and spatial ranges

The 2D contour diagram in Fig. 2-16 is mapped from the 3D representation in Fig. 2-15. The amplitudes of the radial forces are characterized by the colored map. However, the X- and Y-axis correspond to the temporal and spatial representations.

At one time point, it is possible to see three zones along the spatial representation, and these zones represent the three teeth of one pole-pair.

In FEM simulation, the coils of the three-phase machine are energized with sinusoidal current waves, then the radial force wave progresses with twice the fundamental frequency over a pole-pair (see Fig. 2-15 “Time Dependency” axis).

In reality, the power electronics provide PWM (Pulse Width Modulation) signals and not sinusoidal current signals; however, the harmonics resulting from the PWM signal can be analyzed separately by analytical investigation, especially when the FEM software is limited to sinusoidal input signals. In fact, it is important to mention that the induced voltage and the flux density in the air gap are not sinusoidal, even though sinusoidal input currents were used. This explains why it is necessary to make the noise study based on the investigation of the harmonics.

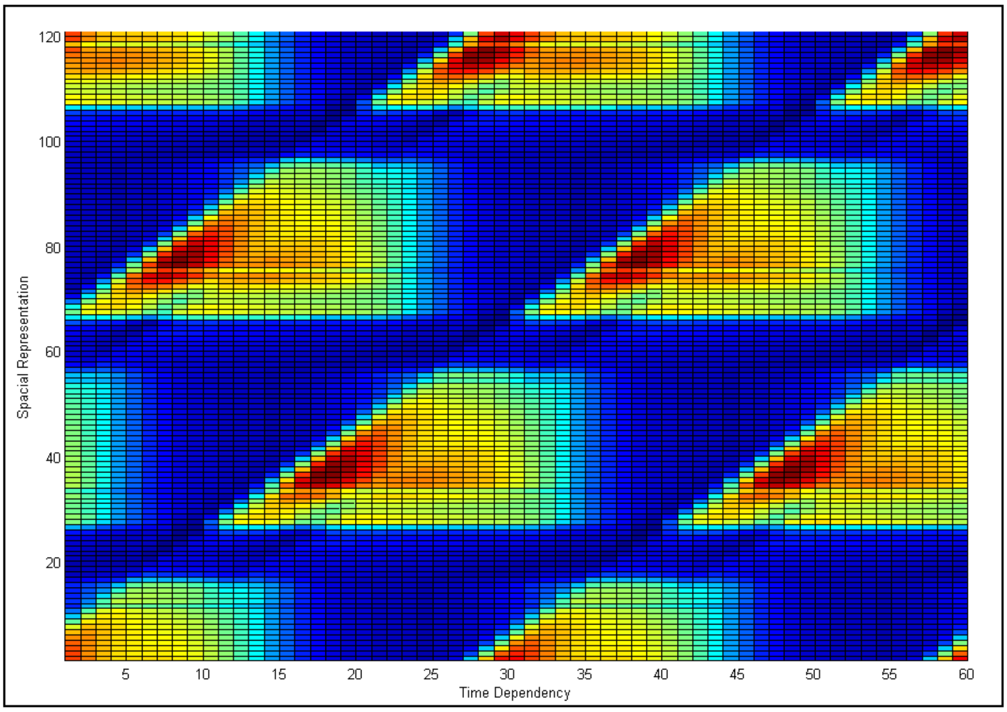

Figure 2-16: Spatial and temporal change in the force amplitudes

Temporal force curve from mode zero

The purpose of the temporal representation is to map the frequency decomposition of the resulting vibration modes. The frequency decomposition should outline the temporal curve of the individual modes in frequency components with the corresponding ordinal numbers.

The two orthogonal force waves of each mode are described as cosine or sine. The cosine and sine mode curves in Fig. 2-17 supplement the statement that mode zero only contains a cosine mode. Theoretically, the cosine mode should not produce any temporal fluctuation in the case of an ideal machine. But the machine is usually operated under saturation where the material characteristics are non-linear. The geometrical shape of rotor and stator, including the slot effect, shifts the design to the non-ideal operating modes. The fluctuation is 23N peak-to-peak.

For the structural analysis, the force of mode zero is equal to one half the amount of the peak force, which is then 11.5 N.

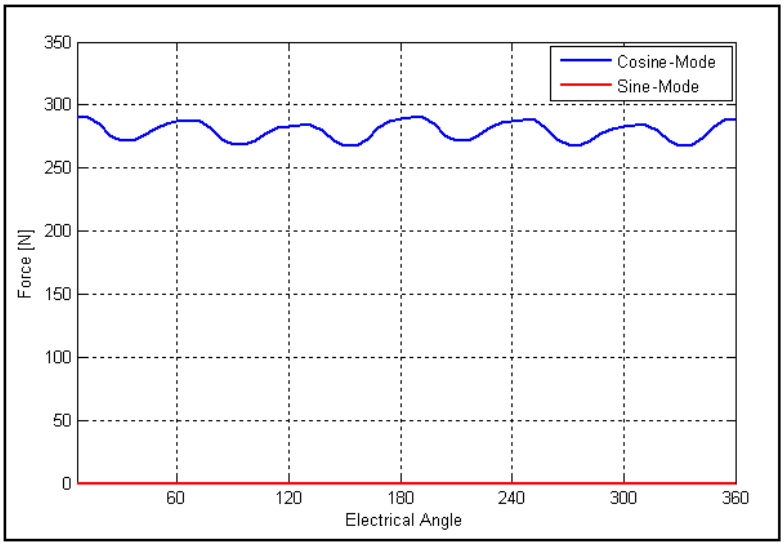

Figure 2-17: Cosine and sine components of mode zero

The temporal decomposition in Fig. 2-18 reveals that mode 0 occurs as a multiple of the 60th frequency order. This number can be generally deduced based on the pole and teeth number of the machine. The Least Common Multiple “LCM” factor of pole and teeth number gives the basic frequency order of mode 0. The force component of the 0th order represents the static amount of mode 0, but the components of orders 60, 120 and 180 give an indication on the distribution of the force. All amplitudes are represented in a logarithmic scale [dB] using a reference point of 1N.

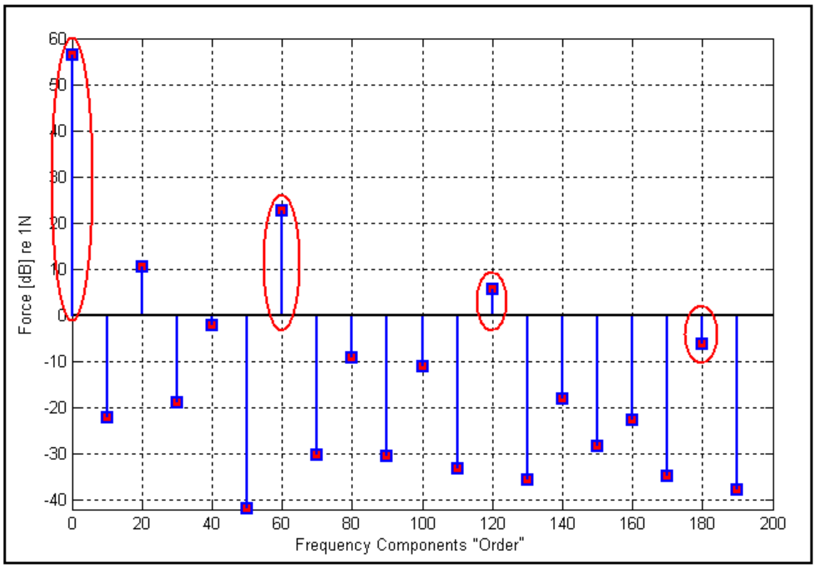

Figure 2-18:Frequency composition of the mode zero in [dB]

Temporal force curve from mode 10:

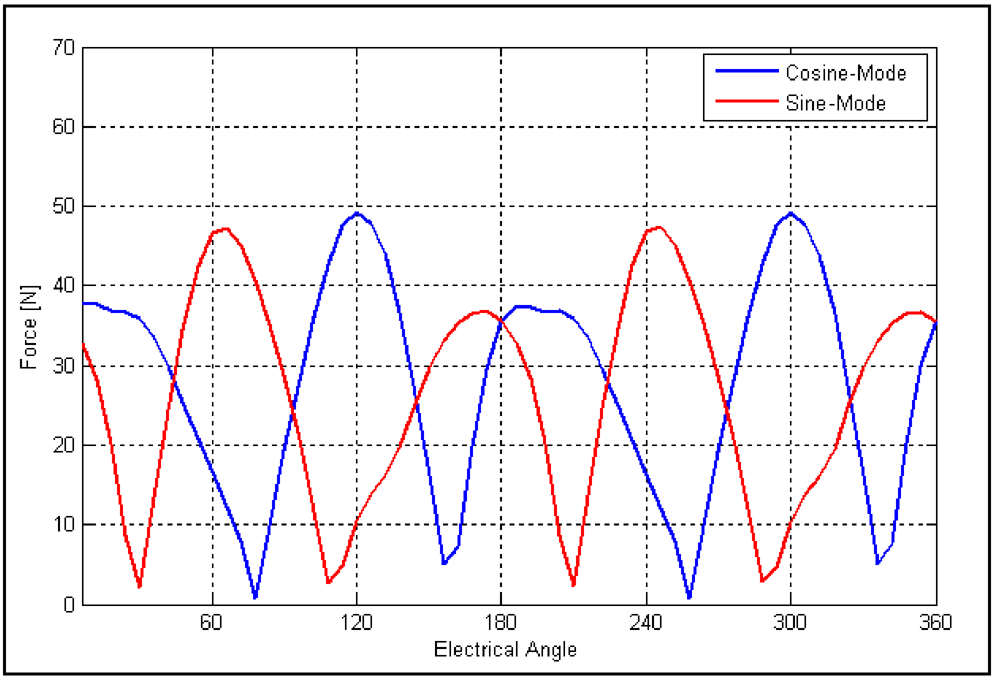

Figure 2-19: Cosine and sine components of mode 10

In Fig. 2-19, the two orthogonal waves were clearly shown. So, the frequency decomposition of one wave is sufficient to expose corresponding orders. The decomposition is also based on the LCM factor of poles and teeth number of the machine, but mode 10 has a rotating reference frame with the rotor, and the representation on stationary reference will introduce the 20th order and its multiples (see Fig. 2-20).

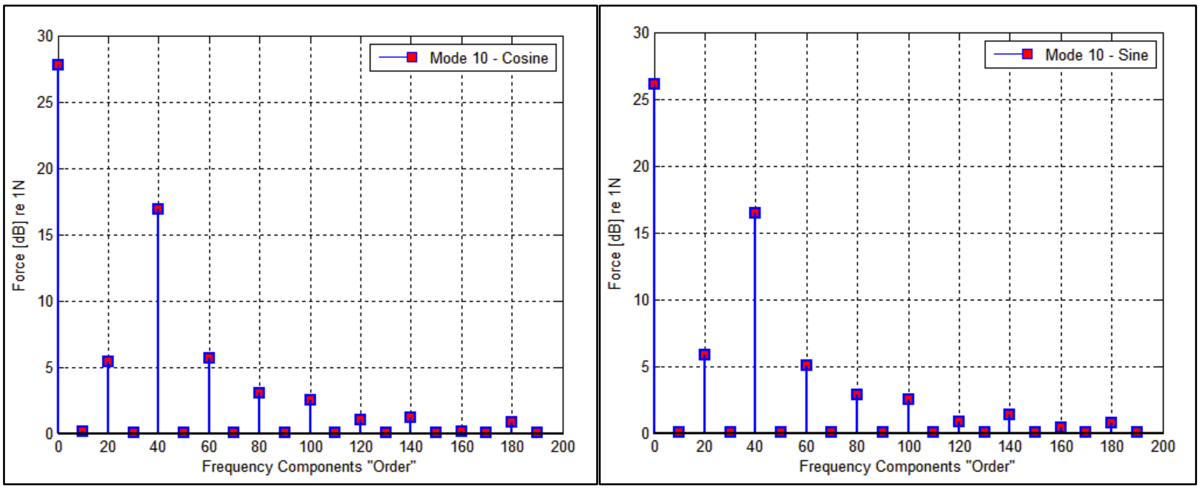

Figure 2-20: Frequency components of mode 10

2.6.5 Eccentricity

The mismatch between the symmetrical axes of the rotor and stator leads to air-gap eccentricity, and this can occur in a static or dynamic form. In an ideal machine, the rotor's axis of rotation is center-aligned with the geometrical axis of the stator bore. A static eccentricity occurs when the rotor rotates about its own centerline, but this centerline does not coincide with that of the stator bore [Ebr2008]. In this case, the position of minimum radial air-gap is fixed in space. A dynamic eccentricity occurs when the center of the rotor is not at the center of rotation and the minimum air gap rotates with the rotor [Rez2010]. The air gap length in the dynamic eccentricity is a function of space and time. Fig. 2-21 shows the difference between static and dynamic eccentricity.

An air gap eccentricity causes a variation in the magnetic reluctance and results in unsymmetrical distribution of the magnetic forces.

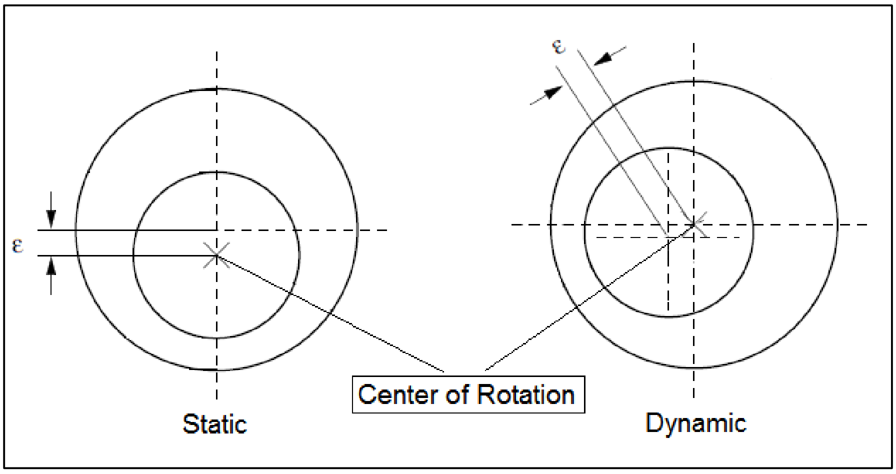

Figure 2-21: Static and dynamic eccentricities

Along the stator circumference and with full mechanical period, the modes 1 and 2, which are excited by the static and dynamic eccentricities, are represented in Fig. 2-23. It is necessary to mention that the eccentricity harmonics are always available, but it can be stimulated by assuming a certain clearance between the rotor and the stator centers in the FEM model. Therefore, the eccentricity would clearly reveal itself with its corresponding modes and orders. Here, an eccentricity of 0.1mm was considered for both cases (static and dynamic).

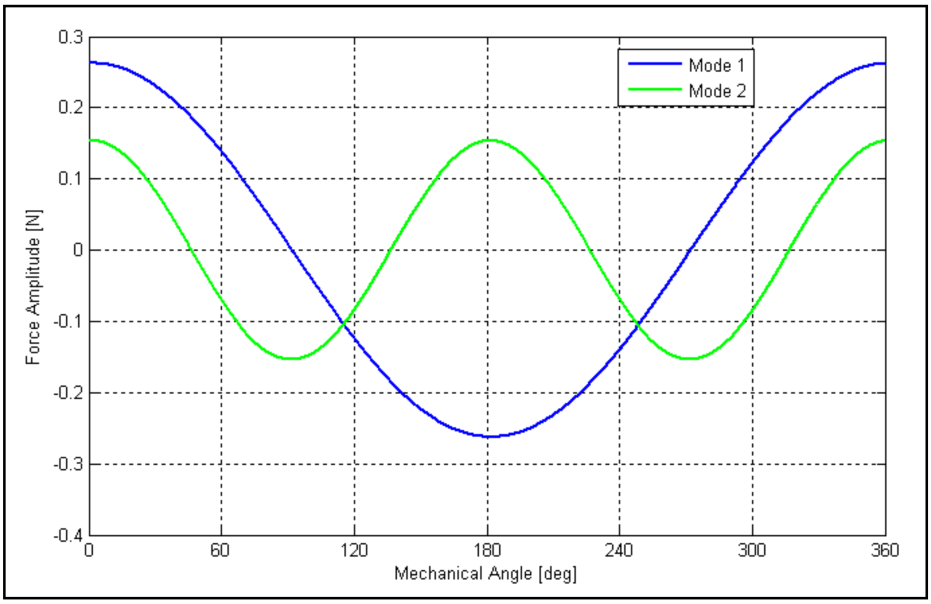

Figure 2-22: Spatial representation of mode 1 and 2 versus a full mechanical period

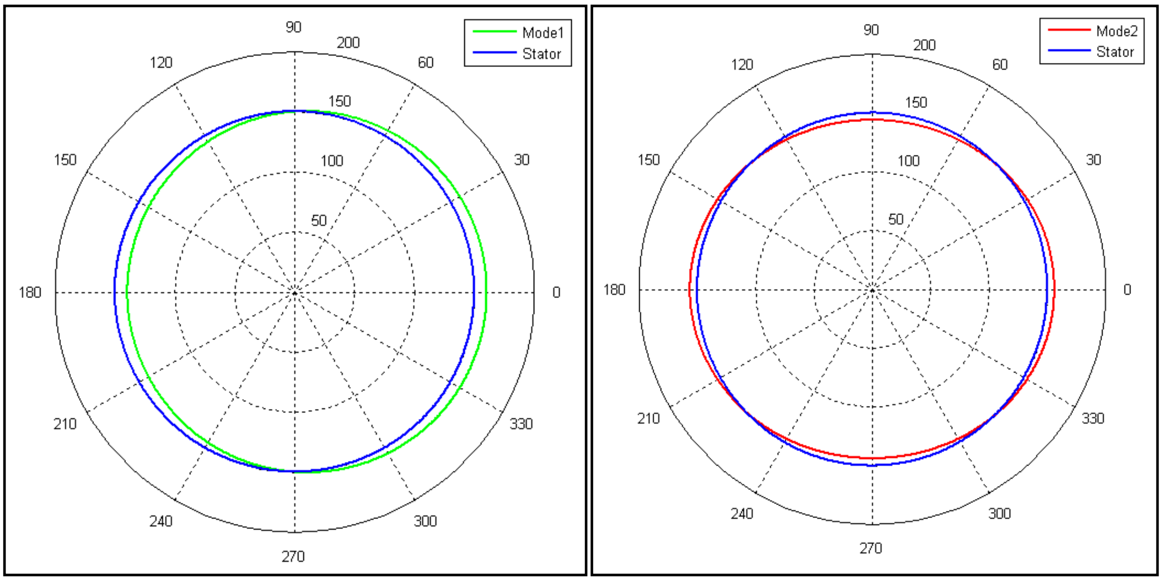

Figure 2-23: Representation of mode 1 and 2 on the stator circumference

3 Structural Analysis

3.1 Modal Analysis

In order to estimate the electromagnetic vibration and noise of Permanent Magnet (PM) machines in hybrid vehicles, a modal analysis for the stator system has to be realized and the natural frequencies have to be consequently determined. This modal analysis can be defined as a process to describe a structure in terms of its natural characteristics, which are the frequencies, damping and mode shapes [Avi2001]. As a result, the vibration in the harmonic response can be predicted and the design of the stator system can be optimized.

Therefore, it is essential to understand the vibration behavior of the stators, so as to prevent resonance between the electromagnetic harmonics in the air gap and the natural frequencies of the stators [Wat1983].

3.1.1 Theoretical

Today, the modal analysis is a well-known method of finding the modes of vibration of a machine or structure. The natural frequency, the modal damping and the mode shape are the modal parameters of every mode. Any change in material properties or in boundary conditions of the model directly affects the modes and their behavior.

3.1.2 The Analytical Method and the Finite Element Method (FEM)

The resonant frequencies can be obtained by analytical calculation, numerical computation (finite element method etc.) and/or experimental techniques. The experimental method can be performed only after a prototype has been built. Therefore, deriving analytical formulae and building numerical computation models which can be validated experimentally are essential for motor designers [Cai2001].

Nowadays, the FE Method is principally used to perform a modal analysis and to compute numerically the natural frequencies of the stator system, but it is also possible to compute analytically the natural frequencies of the PM motors, taking into consideration their special shapes, dimensions, and constraints applied in the hybrid transmission vehicles. The reason behind this is that these analytical and mathematical models are needed by the electrical engineers when they investigate the electromagnetic noise of their developed electric motors. Therefore, they need, for example, analytical or mathematical equations to calculate the natural frequencies of their motor-structures without having to build 3D-models in FEM, and to perform the mechanical analysis which is not in the field of an electrical engineer.

In this chapter, the analytical modal equations for the stator system of a permanent magnet synchronous motor are presented, starting from the mathematical displacement model of a cylindrical shell, then deriving the analytical equations of the stator system, and finally adding to the final model the effect of the stator teeth, the windings and the insulation material. In order to verify this analytical model, a stator system of a PM machine is taken as a case study where its natural frequencies are calculated, verified and compared with the FEM (Finite Element Method) results.

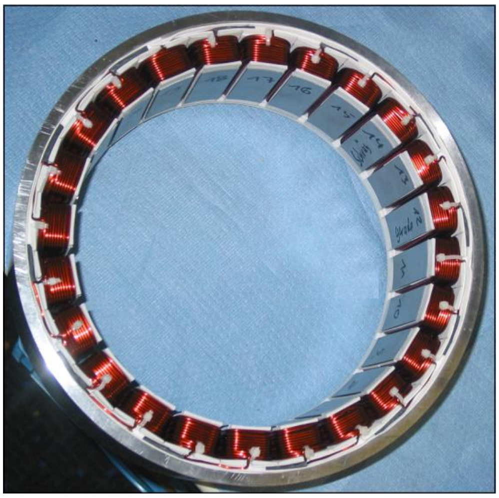

Figure 3-1: A stator of a PMSM

For nearly all electrical machines of hybrid vehicles, the stators are the structural parts that are examined in the analysis of vibration and noise (see Fig. 3-1).

The PM motors used in hybrid electric vehicles are mostly mounted between the engine and the transmission (see Fig. 3-2). Therefore, they are axially restricted and usually have larger diameters in comparison with the traditional electric motors. The space as a constraint is actually a challenge for finding acoustically suitable configurations for such motors [Boe2008].

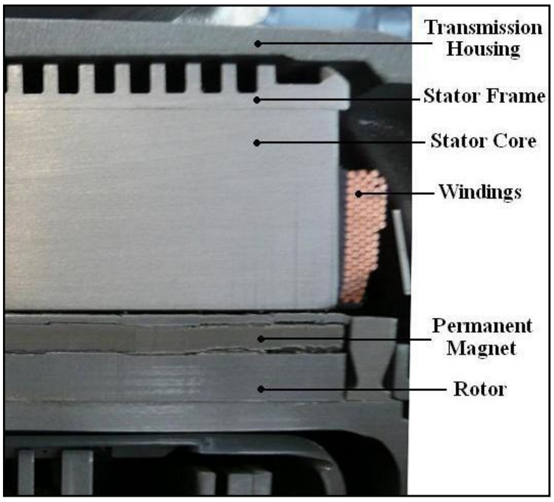

Figure 3-2: Cut side-view of PMSM in transmission

The most difficult problem in the analytical prediction of noise is the accurate calculation of natural frequencies of the stator core-winding-frame system [Gie2007].

An analytical study for computing the natural frequencies of the stator system is performed according to the following steps:

1. Describing the general form for the deformations of a freely vibrating cylindrical shell (cylindrical shell in space) and introducing its characteristic polynomial.
2. Simplifying this general form of a cylindrical shell by applying free-free boundary conditions.
3. Deriving the modal equations according to 2, and finding the general equation of the natural frequency as a function of the mode index.
4. Describing the stator system as two components (frame and core) and establishing a method to model these two components both separately and together.
5. Adding the effect of the stator teeth, the windings and the insulation material to the final system of equations.
6. Performing an analytical study of the stator system of a PM motor and calculating the natural frequencies of the first eight radial-circumferential modes.
7. Setting up a 3D FE simulation in ANSYS for the stator system to verify and analyze the analytical results with the corresponding FEM results and applying a correction factor in case of necessity to improve the accuracy of the analytical study.

Methodology

The two main components of a stator are the frame and the core:

a) The stator frame represents the cylindrical shell that envelops the stator core and encloses the cooling jacket on its outer surface. This cooling jacket can have outwardly extending longitudinal fins, or multiple cooling channels; the cooling element here can be air-based, water-based or oil-based (see Fig. 3-3). Nevertheless, this component, with its irregular external surface, has to be substituted by a cylindrical shell in order to compute its modal characteristics. The methodology here will cover the type of a stator jacket with cooling channels.

   In order to find this substituting cylindrical shell which can replace the stator frame, three conditions have to be fulfilled to assure better results in the analytical calculations. These conditions will always have the following characteristics:

   - The mass of the cylindrical shell has to be equal to the mass of the stator frame.
   - The inner radius of the cylindrical shell has to be equal to the inner radius of the stator frame.
   - The thickness of the cylindrical shell has to be equal to the thickness of the stator frame. The variable parameter will be the axial length of the cylindrical shell.

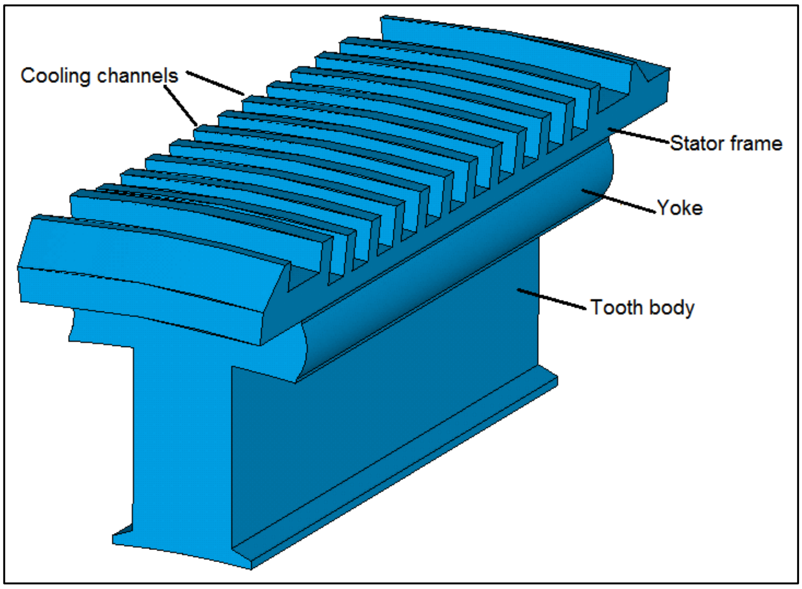

Figure 3-3: Cut-view of the stator

b) The stator core comprises the yoke as well as the teeth and the coils (see Fig. 3-4). It has been modeled as a cylindrical shell with a thickness equal to that of the yoke. The influence of the teeth and the coils will be included in the model.

Figure 3-4: Stator core without coils [Gas2010]

The stator system: many assumptions have been considered in modeling the stator system of an electrical motor. But here, the stator system will be modeled as one cylindrical shell with a thickness equal to the sum of yoke thickness and with the frame thickness. However, the frame thickness is the thickness of a substituting cylindrical shell described with an axial length equal to the axial length of the yoke.

This condition is especially used in modeling the stator system and its purpose is:

- To find an equivalent cylindrical shell with an axial length equal to the axial length of the yoke.
- To assure a uniform pressure distribution between the stator frame and the stator core. This can lead to better results when computing the lumped stiffness and mass of the overall system.

General Model

There is no general agreement on the linear differential equations which describe the deformation of a shell [Ble1995], but there are a number of theories which have been developed for this purpose. Some of these prominent theories are A.E.H. Love (1888), W. Flügge (1934), L.H. Donnell (1938), K.M. Mushtari (1938), E. Reissner (1941) and J.L. Sanders (1959). All these theories have employed some common assumptions in the analysis of shells [Ble1995]:

1. The shells have constant thickness.
2. The shell walls are thin. The shell wall is less than 10% of the shell radius.
3. The shells are composed of linear, elastic, homogeneous, isotropic material.
4. There are no loads applied to the shells.
5. The deformations of the shell (u, v, w) are small in comparison with the radius of the shell. Straight lines perpendicular to the midsurface of the shell remain straight lines perpendicular to the midsurface during deformation (see Fig. 3-5).
6. Rotary inertial and shear deformation are neglected.

Strain-deformation relationships: according to the Flügge theory, the midsurface deformation u, v, and w produce the following strains in the plane of a cylindrical shell:

$$\begin{aligned}
\varepsilon_x &= \frac{\partial u}{\partial x} - z\frac{\partial^2 w}{\partial x^2},\\
\varepsilon_\theta &= \frac{1}{R}\frac{\partial v}{\partial \theta} - \frac{z}{R(R+z)}\frac{\partial^2 w}{\partial \theta^2} + \frac{w}{R+z},\\
\varepsilon_{x\theta} &= \frac{1}{R+z}\frac{\partial u}{\partial \theta} + \frac{R+z}{R}\frac{\partial v}{\partial x} - \frac{\partial^2 w}{\partial x \partial \theta}\left(\frac{z}{R} + \frac{z}{R+z}\right),\\
\varepsilon_{xz} &= \varepsilon_{\theta z} = \varepsilon_{zz} = 0.
\end{aligned} \tag{3.1}$$

Here ε_x is the longitudinal strain, ε_θ the circumferential strain, and $\varepsilon_{x\theta}$ the in-plane shear strain.

The out-of-plane shear strains are assumed to be zero. *z* is a coordinate from the midsurface of the shell, normal to the surface of the shell and directed outward from the cylinder axis. z =0 is the midsurface of the shell. R is the radius of the shell midsurface, θ is the angular coordinate on the center of the shell, and h is the thickness of the shell.

The isotropic stress-strain relationships in a shell read as follows:

$$
\begin{aligned}
\sigma_{xx} &= \frac{E}{1-\nu_p^2}(\varepsilon_x + \nu_p \varepsilon_\theta),\\
\sigma_{\theta\theta} &= \frac{E}{1-\nu_p^2}(\varepsilon_\theta + \nu_p \varepsilon_x),\\
\sigma_{x\theta} &= \sigma_{\theta x} = \frac{E}{2(1+\nu_p)}\varepsilon_{x\theta},\\
\sigma_{xz} &= \sigma_{\theta z} = \sigma_{zz} = 0.
\end{aligned}
\tag{3.2}
$$

Here E is the modulus of elasticity and ν_p is Poisson's ratio. $\sigma_{xx}, \sigma_{\theta\theta}$, and σ_{zz} are normal stresses acting on the x, θ, and *z* faces of the shell element, respectively. $\sigma_{xz}, \sigma_{\theta z}$, and $\sigma_{x\theta}$ are shear stresses.

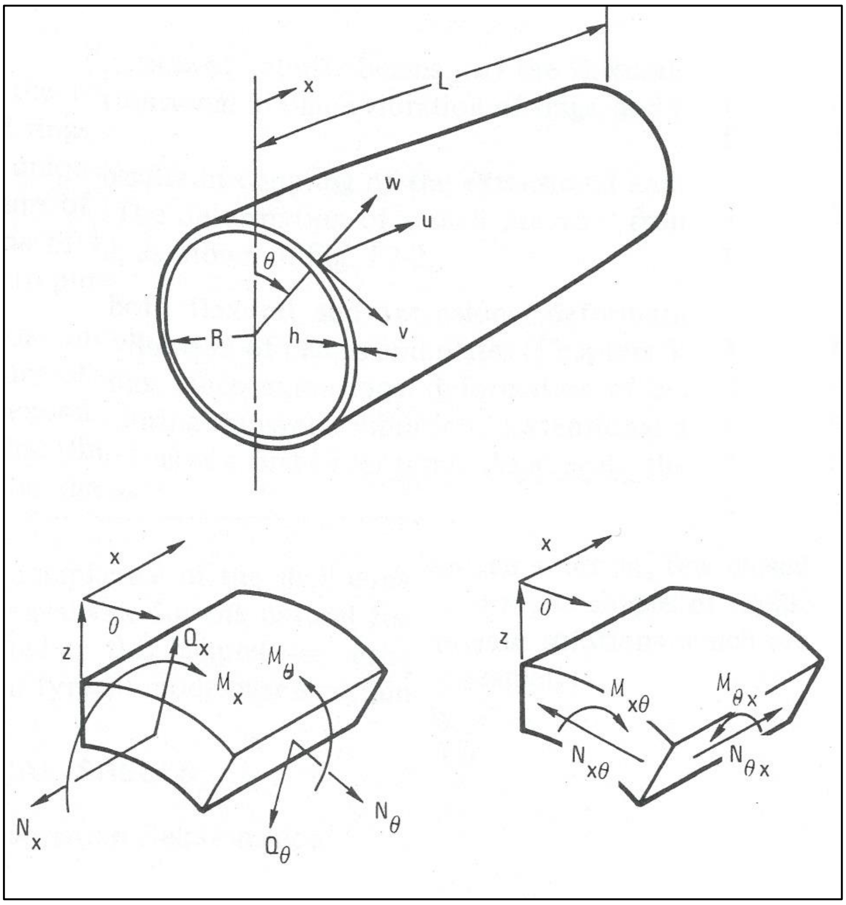

Figure 3-5: Coordinate system, deformations, strains and stresses on a shell element [Ble1995]

The stresses, strains and moments relations shown on the shell element of Fig. 3-5 are described and expressed in equations in [Ble1995]. N_x, $N_{\theta x}$, and N_θ are the resultant forces per unit length of the circumferential edge; Q_θ and Q_x are the transverse shear stresses and also related to the deformations of the shell; M_x, M_θ, and $M_{x\theta}$ are the resultant moments per unit length of the circumferential edge.

General Solution Form

The general form of the deformations of a freely vibrating cylindrical shell reads:

$$\begin{aligned}
&u = A\tilde{\phi}_j'(x/L)\cos i\theta \;\cos\omega\, t,\\
&\mathrm{v} = B\tilde{\phi}_j(x/L)\sin i\theta \;\cos\omega\, t,\\
&w = C\tilde{\phi}_j(x/L)\cos i\theta \;\cos\omega\, t,\\
&i = 0,1,2,3....,\;\; j = 1,2,3... \quad .
\end{aligned} \tag{3.3}$$

The constants A, B, and C describe the amplitude of the axial (u), tangential (v), and radial (w) deformations of the shell midsurface. (ω) is the circular natural frequency of vibration $2\pi f$. (i) is the number of circumferential waves in the mode shape and (j) is the number of longitudinal half-waves in the mode shape (see Fig. 3-6). The axial modal functions $\tilde{\phi}(x/L)$ have to be chosen to satisfy the desired boundary conditions at x=0 and x=L.

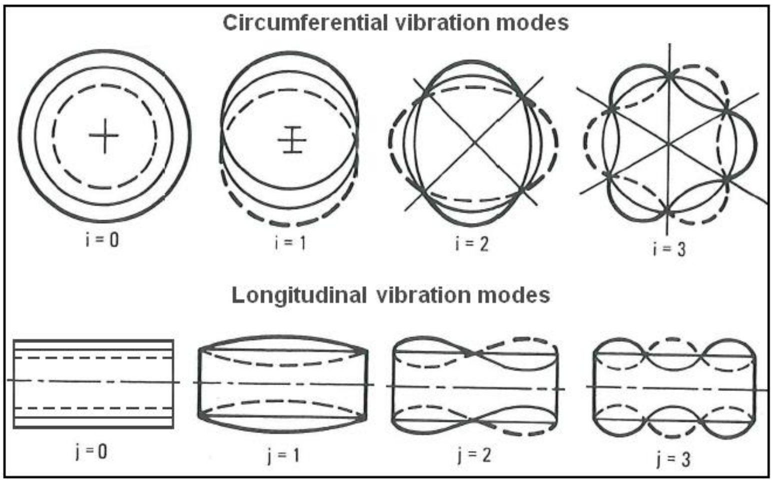

Figure 3-6: Circumferential and longitudinal vibration modes [Ble1995]

Using Eq. 3.3 in conjunction with the Flügge shell theory and Rayleigh-Ritz Technique, the characteristic equation for the natural frequencies and mode shapes of a cylindrical shell is expressed as follows:

$$\begin{bmatrix} a_{11}-\alpha_2\lambda^2 & a_{12} & a_{13} \\ a_{12} & a_{22}-\lambda^2 & a_{23} \\ a_{13} & a_{23} & a_{33}-\lambda^2 \end{bmatrix} \begin{bmatrix} A \\ B \\ C \end{bmatrix} = 0. \tag{3.4}$$

Setting the determinant of the characteristic matrix to zero for non-trivial solutions results in the following characteristic polynomial and mode shapes:

$$\begin{aligned} &\alpha_2\lambda^6 - \lambda^4(a_{11}+\alpha_2 a_{22}+\alpha_2 a_{33}) - \lambda^2(a_{12}^2+a_{13}^2+\alpha_2 a_{23}^2-\alpha_2 a_{22}a_{33}-a_{11}a_{33}-a_{11}a_{22}) \\ &+(a_{12}^2 a_{33}+a_{23}^2 a_{11}+a_{13}^2 a_{22}+a_{11}a_{22}a_{33}+2a_{12}a_{23}a_{13}) = 0 \ , \end{aligned} \tag{3.5}$$

$$\frac{A}{C} = \frac{(a_{33}-\lambda^2)(a_{22}-\lambda^2)-a_{23}^2}{a_{12}a_{23}-a_{22}a_{13}}, \tag{3.6}$$

$$\frac{B}{C} = \frac{a_{12}(a_{33}-\lambda^2)-a_{13}a_{23}}{a_{22}a_{13}-a_{23}a_{12}}, \tag{3.7}$$

where

$$a_{11} = \beta_j^2 + \frac{1}{2}(1+k)(1-\nu_p)i^2\alpha_2\,,$$

$$a_{12} = \nu i\beta_j\alpha_1 - \frac{1}{2}(1-\nu_p)i\ \beta_j\alpha_2\,,$$

$$a_{13} = \nu\beta_j\alpha_1 + k\beta_j\left[-\beta_j^2 + \frac{1}{2}(1-\nu_p)i^2\alpha_2\right],$$

$$a_{22} = i^2 + \frac{1}{2}(1+3k)(1-\nu_p)\beta_j^2\alpha_2\,,$$

$$a_{23} = i\ + ki\beta_j^2\left[\nu_p\alpha_1 + \frac{3}{2}(1-\nu_p)\alpha_2\right],$$

$$a_{33} = 1 + k\left[\beta_j^4 + (i^2-1)^2 + 2\nu i^2\beta_j^2\alpha_1 + 2(1-\nu_p)i^2\beta_j^2\alpha_2\right],$$

$$\beta_j = \lambda_j R/L \quad ; \quad k = \frac{h_c^2}{12R_c^2} = \frac{h_c^2}{3D_c^2}\ .$$

The variables $\alpha_1$and α_2 are the integrals of the mode shape:

$$\alpha_1 = -\frac{1}{L}\int_0^L \tilde{\phi}_j''(x)\tilde{\phi}_j(x)dx \quad , \quad \alpha_2 = \frac{1}{L}\int_0^L \left[\tilde{\phi}_j{}'(x)\right]^2 dx\,.$$

λ_j are the dimensionless beam frequency parameters which correspond to the desired axial mode shape:

$$\lambda = \omega R\left[\rho(1-\nu_p^2)/E\right]^{1/2}, \tag{3.8}$$

where ρ is the density of the shell material.

Simplified General Solution

According to the assumptions, Sharma and Johns [Ble1995], Eq. 3.3 could be considerably simplified if the circumferential strain ε_θ and the shear strain $\varepsilon_{x\theta}$ of the midsurface of the shell (i.e. at z=0) were neglected, which means that the extensional modes are not included any more. These assumptions lead to the midsurface deformations:

$$\begin{aligned} u &= -\frac{G}{i^2} R \frac{d\tilde{\phi}_j}{dx} \cos i\theta \ \cos\omega t \ , \\ \mathrm{v} &= -\frac{G}{i} \tilde{\phi}_j \sin i\theta \ \cos\omega t \ , \\ w &= G\tilde{\phi}_j \cos i\theta \ \cos\omega t \ . \end{aligned} \tag{3.9}$$

The higher circumferential mode natural frequencies can then be expressed as:

$$f_{ij} = \frac{\lambda_{ij}}{2\pi R}\left[\frac{E}{\rho(1-\nu_p^2)}\right]^{1/2}, i = 2,3,4,\ldots \ , j = 1,2,3,\ldots. \ , \tag{3.10}$$

where ρ is the density of the shell material, G is a constant.

The dimensionless frequency parameter λ_{ij} is given by:

$$\lambda_{ij}^2 = \frac{\beta_j^4 + ki^2\beta_j^2\left[\beta_j^2 i^2 + 2\nu_p i^2(i^2-1)\alpha_1 + 2(1-\nu_p)(i^2-1)^2\alpha_2\right] + ki^4(i^2-1)^2}{\beta_j^2\alpha_2 + i^2(i^2+1)}. \tag{3.11}$$

Free-Free Boundary Conditions

The boundary conditions of a cylindrical shell free at both ends yield to the following:

$$N_x = M_x = 0 \ , \ N_{x\theta} + \frac{M_{x\theta}}{R} = 0,$$

$$Q_x = \frac{1}{R}\frac{\partial M_{x\theta}}{\partial\theta} = 0 \quad at \quad x = 0, \ L \cdot$$

In fact, the higher modes (i = 2, 3, 4 . . .) of a free-free cylindrical shell can be grouped by the axial (x) behavior of the mode shape. If the mode does not vary axially, then the mode corresponds roughly to j=0. Consequently, with j=0, the axial mode shape $\tilde{\phi}_j(x/L)$ is constant and $\tilde{\phi}'(x/L)$ will be equal to zero. This case, which is analyzed by Rayleigh, allows computing the mode shapes and the corresponding natural frequencies. Eq. 3.9 results in:

$$u = 0 \ ,$$
$$\mathrm{v} = -\frac{G}{i}\tilde{\phi}_j \sin i\theta \ \cos \omega t \ , \tag{3.12}$$
$$w = G \cos i\theta \ \cos \omega t \ .$$

The frequency parameter can be deduced, for this case, from Eq. 3.11 as follows:

$$\lambda_i = \frac{k^{1/2} i \ (i^2 - 1)}{(i^2 + 1)^{1/2}} , \tag{3.13}$$

where $\beta_j = \lambda_j R / L = 0$ for j = 0.

The natural frequencies can be then computed from:

$$f_i = \frac{\lambda_i}{2\pi R}\left[\frac{E}{\rho(1-\nu_p^2)}\right]^{1/2} , i = 2,3,4,... \ . \tag{3.14}$$

When i = 0, then $\lambda_0 = 1$ and the natural frequency f_0 can be expressed by:

$$f_0 = \frac{1}{2\pi R}\left[\frac{E}{\rho(1-\nu_p^2)}\right]^{1/2} . \tag{3.15}$$

Effect of Teeth and Windings

The hybrid PM motors have to be as compact and as short as possible because the existing axial space considered for the construction is usually limited. Consequently, it is difficult to excite the axial modes, especially when the axial length is too small with respect to the diameter, that is, when $L << 2R$. So it is essential to determine the radial modes of the stator and the corresponding natural frequencies for the analysis of vibration and noise in the hybrid power train.

Indeed, there are analytical equations which include the effect of the teeth, the windings and the isolation material in the computation of the modal characteristics of a stator. These equations are derived in [Gie2006]:

1. Breathing Mode (i = 0), the lumped stiffness and mass:

$$k_0 = 4\pi \frac{E_c h_c L}{D_c} , \tag{3.16}$$

$$m_0 = m_c k_{md} , \tag{3.17}$$

$$k_{md} = 1 + \frac{m_t + m_w + m_{in}}{M_c}, \tag{3.18}$$

with the yoke thickness h_c, the mean diameter D_c, the mass of the teeth without the yoke m_t, the mass of the windings m_w, the mass of the insulation m_{in}, and the mass of the yoke m_c.

The natural frequency is given by:

$$f_0 = \frac{1}{2\pi}\sqrt{\frac{k_0}{m_0}} = \frac{1}{\pi D_c}\sqrt{\frac{E_c}{\rho_c k_{in} k_{md}}}, \tag{3.19}$$

where k_{in} is the stacking factor: $k_{in} = 0.96$.

It is important to mention that the effect of the teeth and the windings in the breathing mode is just observed in the mass equation through the factor k_{md}.

2. Bending-Mode (i = 1):

$$k_1 = 4\pi \frac{E_c h_c L_c}{D_c} \tag{3.20}$$

$$m_1 = \frac{m_c k_{md}}{F_1^2} \tag{3.21}$$

$$F_1 = \sqrt{\frac{2}{1 + k\ k_{mrot} / k_{md}}}, \tag{3.22}$$

where k_{mrot} is the mass addition factor for rotation:

$$k_{mrot} = 1 + \frac{s_1 c_t L_i h_t^2}{\pi D_c I_c}\left(1 + \frac{m_w + m_{in}}{m_t}\right)(4h_t^2 + 6h_c h_t + 3h_c^2). \tag{3.23}$$

I_c is the area moment of inertia about the neutral axis parallel to the cylinder axis, s_1 is the number of stator teeth, c_t is the tooth width and h_t is the tooth height.

$$I_c = \frac{h_c^3 L}{12} \tag{3.24}$$

3. Circumferential modes (i ≥ 2):

$$k_i = 16\pi \frac{E_c I_c}{D_c^3}(i^2 - 1)^2 k_a^2, \tag{3.25}$$

$$m_i = m_c \frac{k_{md}}{F_i^2}\left(\frac{i^2+1}{i^2}\right), \tag{3.26}$$

$$F_i = \left(1 + \frac{k^2(i^2-1)[i^2(4+k_{mrot}/k_{md})+3]}{i^2+1}\right)^{-1/2}. \tag{3.27}$$

The coefficient k_a is taken as a unity because there are no end bells and frame support (foot or flange) in the case of a PM motor for a hybrid power train.

Modeling of the stator frame

The stator frame has been modeled as a cylindrical shell. The radial modes with j=0 have to be analytically computed for the stator frame. The frame has an irregular surface, and it has to be substituted by a cylindrical shell according to the conditions mentioned in the methodology, which means that the equivalent cylindrical shell has the following dimensions:

1- The inner radius of the shell is equal to the inner radius of the stator frame:
$R_s = R_f = 0.145m$.

2- The mass of the shell is equal to the frame mass:
$m_s = m_f = 2.8568kg$.

3- The thickness of the shell is equal to the frame thickness:
$h_s = h_f = 0.0074m$.

The volume of the stator frame can be computed as follows:

$$V_f = \frac{m_f}{\rho} = \frac{2.8568}{7850} = 0.36392 * 10^{-3} m^3,$$

where ρ is the material density of the stator frame.

The volume of the equivalent cylindrical shell has to be equal to the volume of the stator frame; consequently, the axial length of the equivalent cylindrical shell can be computed as follows:

$$V_f = L \times \pi \times \left[(R_f + h_f)^2 - R_f^{\,2}\right] \tag{3.28}$$

yielding to: $L = \dfrac{V_f}{\pi \times \left[(R_f + h_f)^2 - R_f^{\,2}\right]} = 0.052636m$.

FEM and analytical results of the Eigen frequencies for the real stator frame in (Hz)								
Mode Index	0	2	3	4	5	6	7	8
FEM Results	5429	199	561	1075	1736	2545	3495	4585
Analytical Results	5663	218	618	1184	1915	2809	3866	5086
Deviation in %	4%	9%	9%	9%	9%	9%	10%	10%

Table 3-1: Comparison between the FEM results and the analytical results of the real stator frame

Using Eq. 3.13 and Eq. 3.14, the dimensionless frequency parameter (λ_i) as well as the Eigen frequencies of the equivalent cylindrical shell can be computed. Table 3-1 presents the FEM results of the real stator frame with the analytical results of the equivalent cylindrical shell.

A 3D FEM model of the stator has been constructed in ANSYS Workbench to verify the analytical results. The FEM model consists of two parts: the frame and the core. Each of these two parts is simulated separately by deactivating the other one. Finally, the two parts, which represent the stator, are simulated together. A mapped mesh has been used for the teeth in the axial directions and for the frame in circumferential direction, in order to minimize the number of the finite elements. Contact elements have been automatically inserted between the two parts. The boundary conditions have been chosen based on the results of an experimental modal analysis. All boundary conditions will be discussed in detail later in this chapter.

Referring to Tab. 3-1, a maximum deviation of 10% has appeared between the FEM and analytical results of the stator frame. This means that this method can be considered for analytical calculation within a maximum error of 10%.

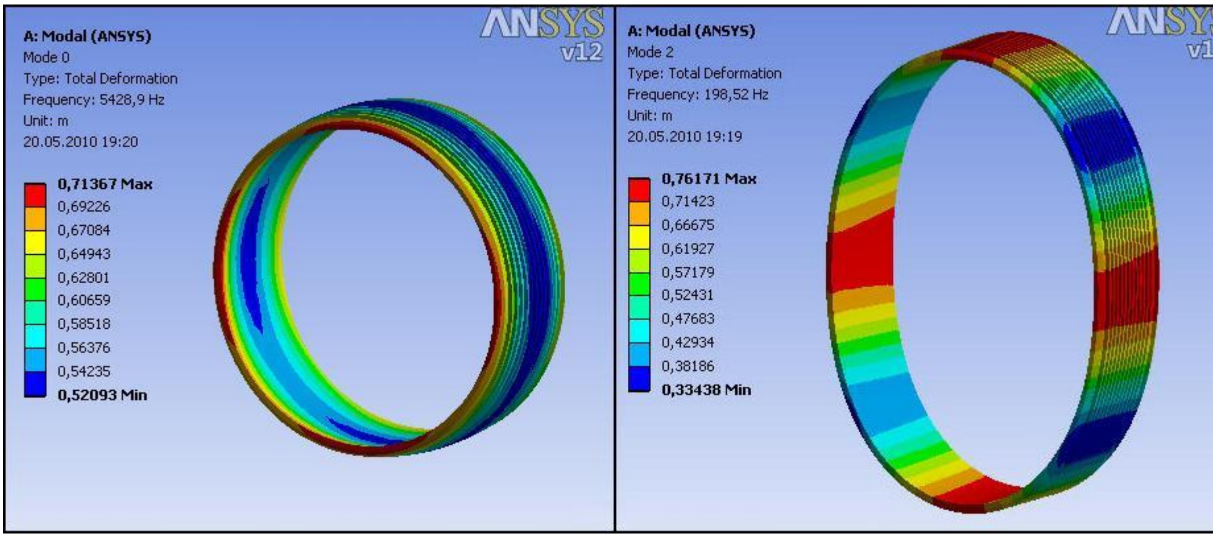

Figure 3-7: Mode 0 and Mode 2 for the real stator frame

Modeling of the stator core

The stator core comprises the yoke and the teeth of the stator. The Eigen frequencies of the first eight modes have to be computed according to the equations from 3.16 to 3.27, including the teeth effect.

Table 3-2 contains the values of parameters used in the analytical calculations of the Eigen frequencies for the stator core. The analytical results show a maximum deviation of 9% in comparison to the FEM results (see Tab. 3-3).

Parameter	Value
m_c (kg)	4.91
m_t (kg)	3.65
E_c (Pa)	200e^9
I_c (m^4)	2.46e^{-9}
k_{mrot}	23.11
k_{md}	2.34
k	0.0153

Table 3-2: Values of parameters

FEM and analytical results of the Eigen frequencies for the stator core in (Hz)								
Mode index	0	2	3	4	5	6	7	8
FEM results	3790	171	470	875	1367	1924	2526	3147
Analytical results	3767	162	454	860	1373	1980	2674	3445
	1%	6%	4%	2%	0%	3%	6%	9%

Table 3-3: Comparison between the FEM and analytical results of the stator core

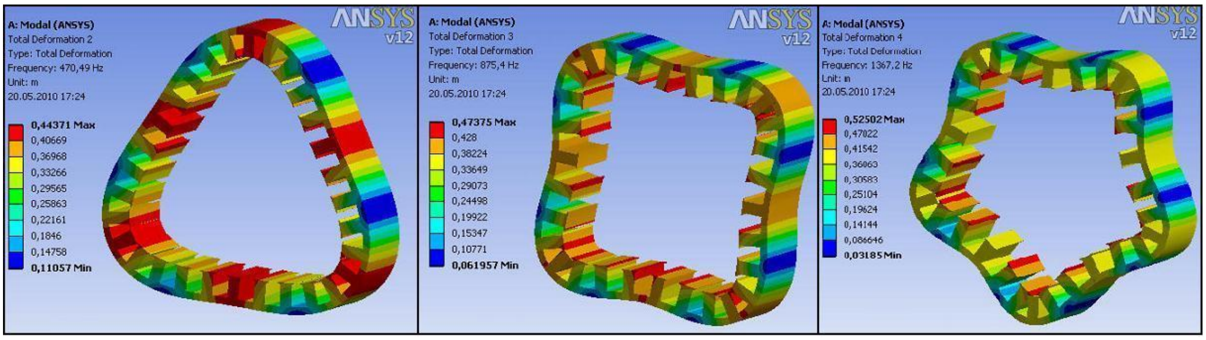

Figure 3-8: Mode 3, 4 and 5 of the stator core

Modeling of the stator system

As mentioned before, the stator system will be represented as a cylindrical shell with a thickness equal to the sum of the yoke thickness and the thickness of the equivalent cylindrical shell of the frame. In this case, the thickness of the equivalent shell for the frame has to be computed using Eq. 3.18 with an axial length (L) equal to the axial length of the yoke; otherwise it is not possible to combine the two cylindrical shells as one part. The new thickness of the equivalent shell can then be added to the thickness of the yoke. The Eigen frequencies of the stator system are subsequently computed using Eq. 3.16 until Eq. 3.27 as shown in Table 3-4.

FEM and analytical results of the Eigen frequencies for the stator system in (Hz)								
Mode index	0	2	3	4	5	6	7	8
FEM results	4261	321	877	1621	2507	3487	4510	5512
Analytical results	4258	313	875	1649	2609	3732	4992	6366

Table 3-4: Comparison between the FEM and analytical results of the stator system

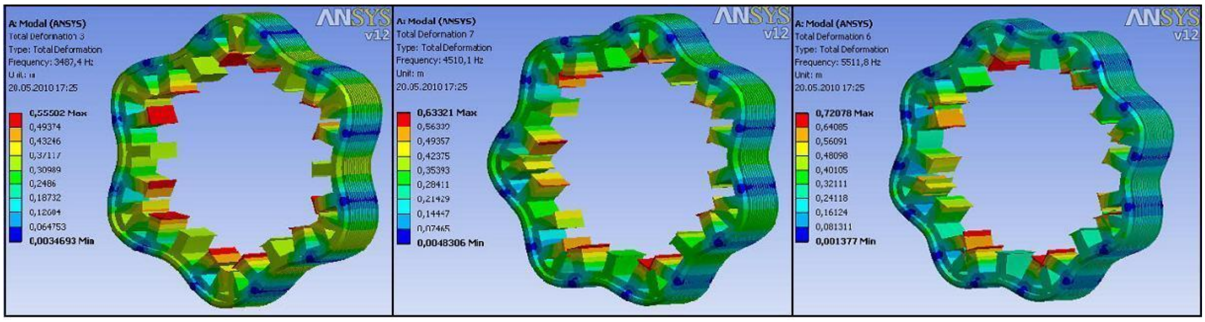

Figure 3-9: Mode 6, 7 and 8 for the stator system

3.1.3 Experimental Modal Analysis

One of the most important areas of structural dynamics testing is that of experimental modal analysis. This is because most noise, vibration or failure problems in mechanical structures and systems are caused by excessive dynamic behavior. This behavior results from complex interactions between applied forces and the mass-elastic properties of the structure.

The implementation of the Fast Fourier Transform (FFT) in computer-based signal analyzers has provided the environmental testing laboratory with a fast and more powerful tool for acquisition and analysis of vibration data. As a result, these tests are used more today for dynamic testing to complement the FEM structural analysis activities [RAM1983].

Advantages of Modal Testing:

In order to use FEM models with confidence, it is necessary to confirm the accuracy of the model by comparing the modal parameters (frequency, damping and mode shapes) predicted by the simulation with the modal parameters identified by the experimental modal test. Also, the inaccurate definition of modal parameters and the unrealistic boundary conditions in simulation are the main reasons behind the execution of an experimental modal analysis.

In the case of hybrid PM motors, as shown before, the specification of the boundary conditions between the core and the frame of the stator is one of the most important topics in modeling.

The core and the frame can be taken as one solid part, or a contact element with diverse contact conditions can be applied between them.

In addition, the implementation of the individual teeth concept in the stator has to be investigated. This is because the teeth are assembled using different methods which give no indication of the mechanical behavior of the teeth among each other from one side, and with the stator frame from another side.

Individual teeth in stator core “Joint-Lapped Core”

The entire section of the core can be punched as one piece, which is one of a number of methods used in the manufacturing of electrical motors. With this method, the wasted steel after the punching process is estimated to be around 80% to 90% of the purchased iron material [Mei2008]. With the individual teeth concept, the wasted iron material during the punching process is reduced. This is because the teeth patterns are placed side by side in the punching tool, which allows minimizing the wasted steel between the teeth in all directions.

In fact, there are numerous patents which describe how to assemble the individual teeth [Zep2006, Shi2008, Har2005, Tat2009, Yos2004, Kol2005, and Hor2005]. In some patents, the teeth have to be axially inserted into the slots of the stator ring and secured in fixed radial alignment (see Fig. 3-10) [Zep2006]. This concept permits utilization of an optimized magnetic material for the teeth production, like the grain oriented electrical steel sheets which allow the magnetic flux to orient itself along the central axis of the teeth for better magnetic performance.

Some other patents have split the stator into multiple stator segment assemblies. Each stator segment typically includes one stator tooth [Har2005]. The individual stator segments or teeth are usually wound individually and then assembled and subsequently combined using different assembling methods (see Fig. 3-11). In this case, the yoke of the stator is also split and distributed to the stator segments. There are various assembling methods for these individual stator segments which are based either on the shape design of the tooth or on the connection structure.

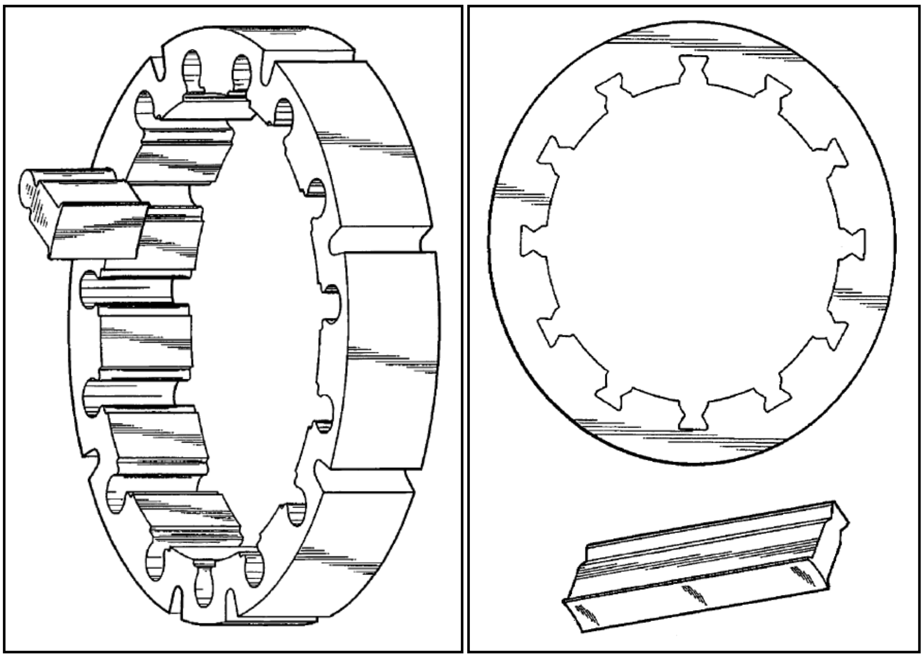

Figure 3-10: Axially mounted teeth [Zep2006]

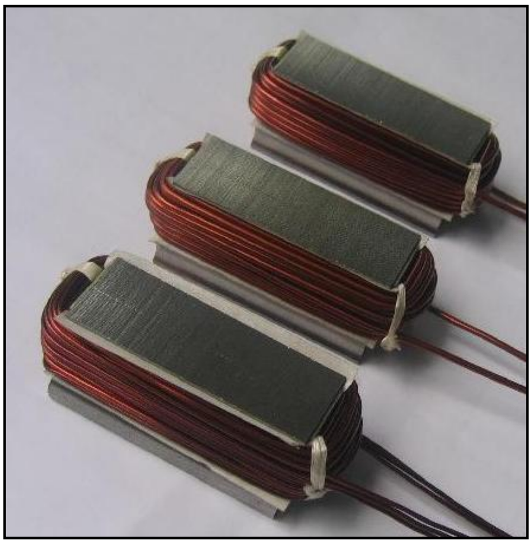

Figure 3-11: Stator teeth wounded individually

In some machines, there is no stator frame (or outer cylindrical shell) and the individual stator segments or teeth are assembled by means of connection structures like screws or clamps fitted between two adjacent teeth. These different assembling methods have been described in Patent [Tat2009].

A clamp with a square U-shaped metal can be press-fitted into the holes in the teeth bodies (see Fig. 3-12). Thus, the adjacent teeth are fixed to each other.

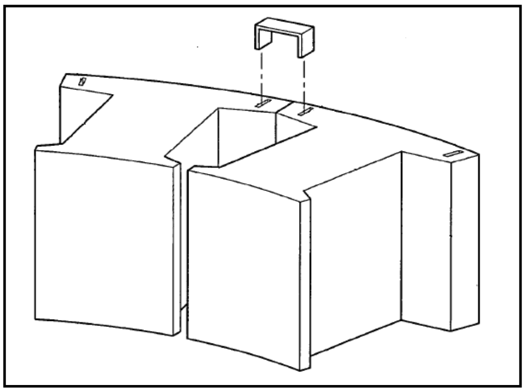

Figure 3-12: U-shaped clamp [Tat2009]

The U-shape clamp consists of metal plates that can serve as a connection member straddles over the screw openings available in the teeth bodies (see Fig. 3-13a). However, Fig. 3-13b shows a stator segment or tooth which has a cut-off portion of a rectangular parallelepiped shape at one end on its top side, this cut-off portion is provided with a cylindrical hole which extends downward. A projecting section is formed on the other end of the tooth and a cylindrical hole is formed in the vertical direction. The bolt is inserted through the holes and provides a connection structure between the teeth of the stator.

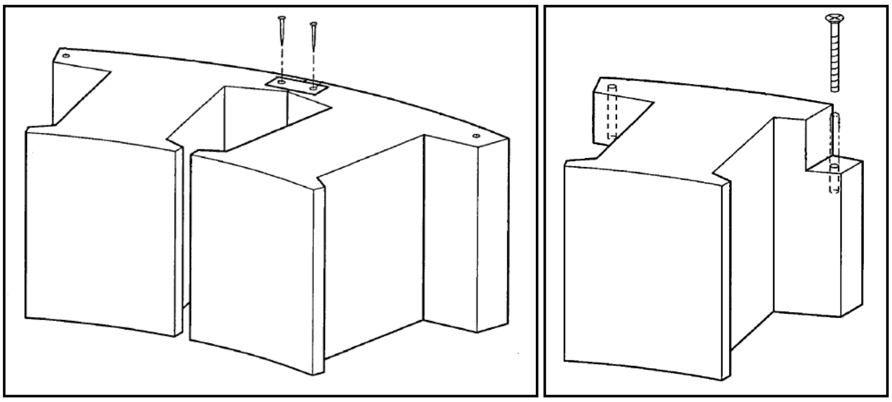

Figure 3-13:Member straddles (a) and screws (b) for teeth connection [Tat2009]

A connection structure has to be used in assembling the individual stator teeth, especially when a stator frame is not excitable, but the existence of the frame gives the opportunity to implement other assembling methods. This technology is described in the literature [Yos2004] and used for large motors where a frame or housing is disposed separately (see Fig. 3-14). This technology of assembling uses the press-fitting or shrinkage fitting concept in order to insert the stator segmented teeth into the cylindrical frame or housing.

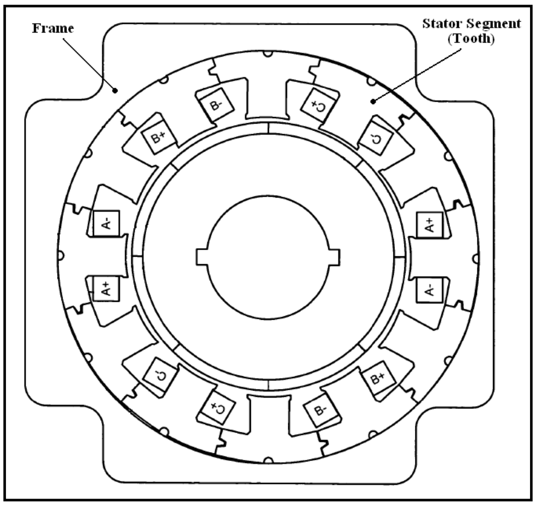

Figure 3-14: Individual teeth with a stator frame [Hor2005]

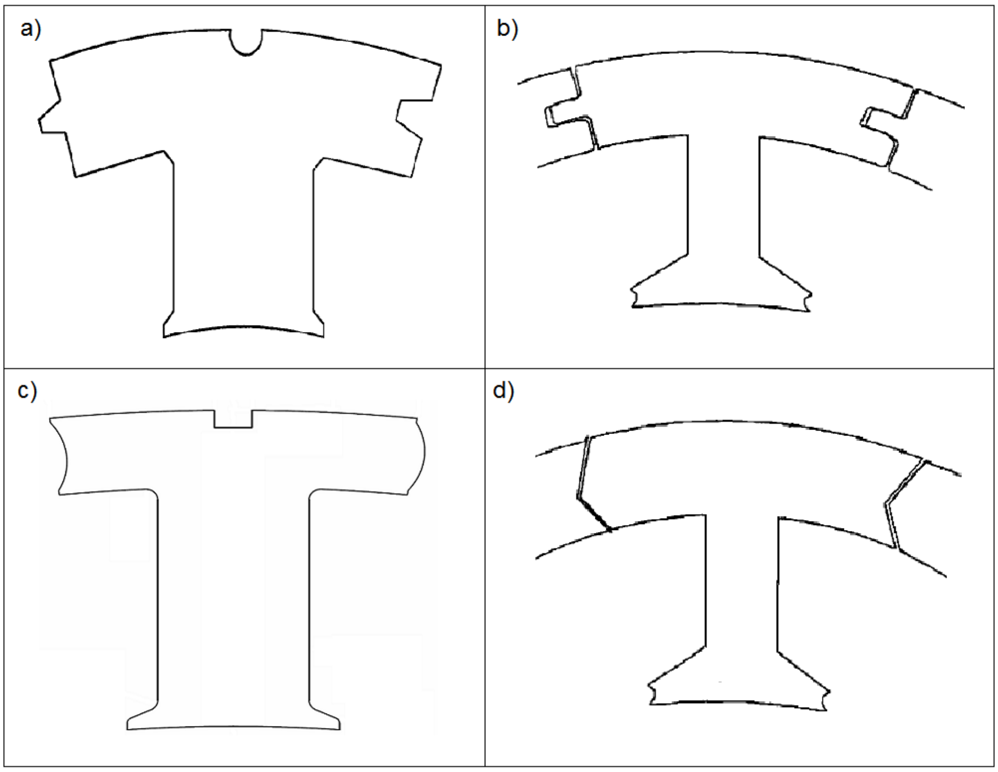

Figure 3-15:Different shape designs for individual teeth [Kol2005]

In this technology, the shape of the stator segment also plays an important role in holding the teeth together. The stator teeth align with each other via the tongues and the grooves formed on the side edges of each tooth. The various shape designs of the individual tooth differ from each other by different shapes of tongues and grooves. These grooves can have a “V” shape, a “C” shape, a rectangular or a trapezoidal shape (see Fig. 3-15).

Electrical and mechanical characteristics

The electrical and the mechanical characteristics of the individual teeth concept have to be verified in order to evaluate the motor performance and to indicate the strength as well as the weakness of this concept in comparison with other applied manufacturing theories. For the individual teeth concept, where the teeth are arranged circularly and pressed onto the stator frame, the high circularity and rigidity have to be maintained in order to achieve a low level of noise and vibration [Aki2003]. For this reason, the shrink-fit procedures have to be proved and checked experimentally by measuring the tolerances on contact surfaces and by defining an acceptable range for the axial pressing force exerted during the assembly process. The pressing force has to be defined according to the motor size and to the teeth areas subjected to this pressure. It is also necessary to mention that the pressing process for those motors can be performed by cold shrink fit as well as by hot shrink fit. At the end, the rigidity can be improved so that it is similar to that of the non-separate core.

In the non-separate stator cores, the coils are wound by inserting the winding needle in the slot opening area between the teeth, and letting the needle take up some of the stator slot area, thus reducing significantly the slot fill factor. However, with separate teeth, which receive pre-wound coils or which can be wound individually before being assembled, a high slot fill factor can be achieved. Also, the use of concentrated winding technology causes a reduction in the coil length in comparison with that of the distributed winding technology. The reduction in the coil length decreases the coil resistance and consequently reduces the copper losses in the windings and improves the thermal behavior of the machine.

Test description

An experimental modal analysis for the stator without windings is performed using a shaker excitation system, but with two different receptions systems, firstly, with acceleration sensors and, secondly, with a 3D laser Scanning Vibrometer. The aim is to cover a high frequency range up to 10 KHz and to recognize the boundary conditions between the teeth and the frame, as well as to check the rigidity of the stator. Here, the rigidity of the stator can be checked by recognizing the movement occurring between two consecutive teeth and between the inner surface of the stator frame and the outer radial surfaces of the teeth. This point was actually the reason for the implementation of two different reception systems and especially the reason behind the use of the 3D laser Scanning Vibrometer.

Shaker excitation

Actually, not all structures can be tested by applying an impact force. This is because this method has a limited frequency range or a low energy density over a wide spectrum, so the impacting force will not be sufficient to excite adequately the modes of interest. Therefore, an artificial excitation with one or more shakers that are attached to the stator can be used to stimulate the structure.

In these experimental tests, electro-dynamic shakers are used. A shaker is usually attached to the structure using a stinger (long slender rod), so that the shaker will only impart force to the structure along the axis of the stinger (the axis of force measurement). A force sensor is then attached between the structure and the stinger to measure the excitation force.

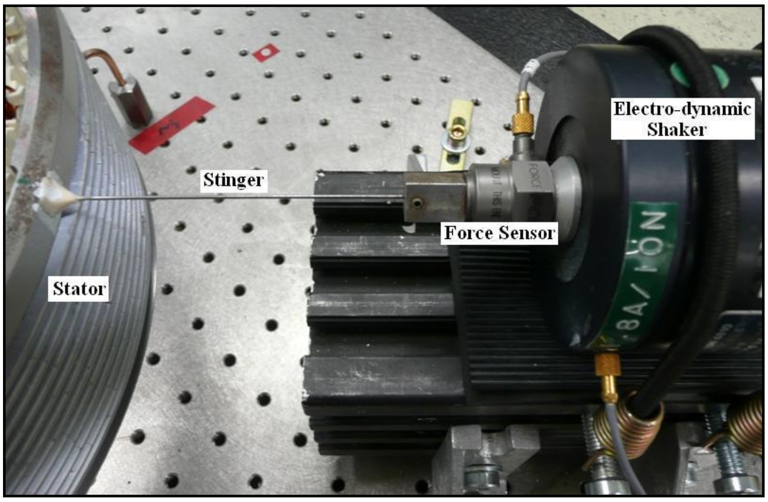

Figure 3-16: Shaker used for excitation

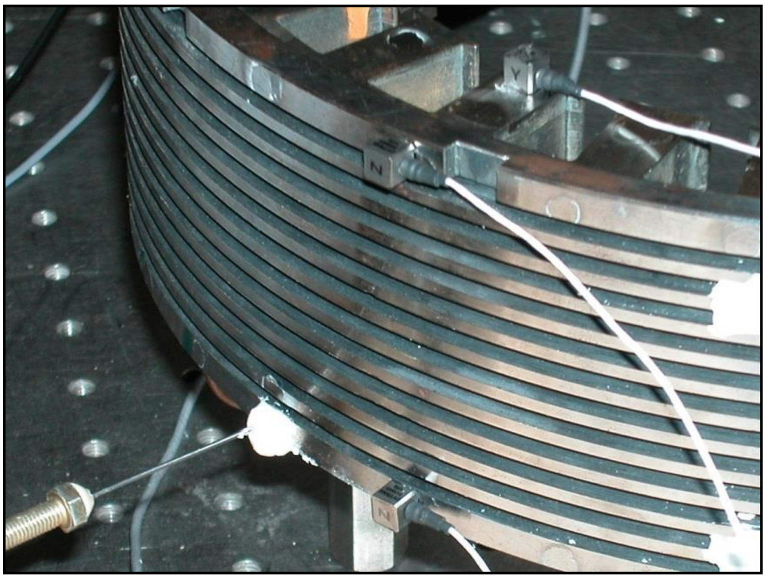

Figure 3-17: Acceleration sensors in all directions

Reception System 1

The signal is retrieved using multiple acceleration sensors mounted on the stator bodies. These sensors are glued onto the stator in different positions and directions. For the radial direction, many acceleration sensors have been mounted on both sides of the stator frame as well as on the individual tooth body (see Fig. 3-17).

Reception System 2

The “3D Laser Scanning Vibrometer” is used to enable an accurate determination of the operating deflection shapes and Eigen modes across a wide range of frequencies. The system is non-contact, so there is no need to attach sensors or run cables. The vibrations are measured exactly without any interference caused by the surface features [Pol2010]. The 3D Scanning Vibrometer comprises three scanning heads, each with an integrated laser interferometer, scanner and video camera, an instrumentation cabinet with a central computer and three data acquisition and control units for the three scanning heads (see Fig. 3-18).

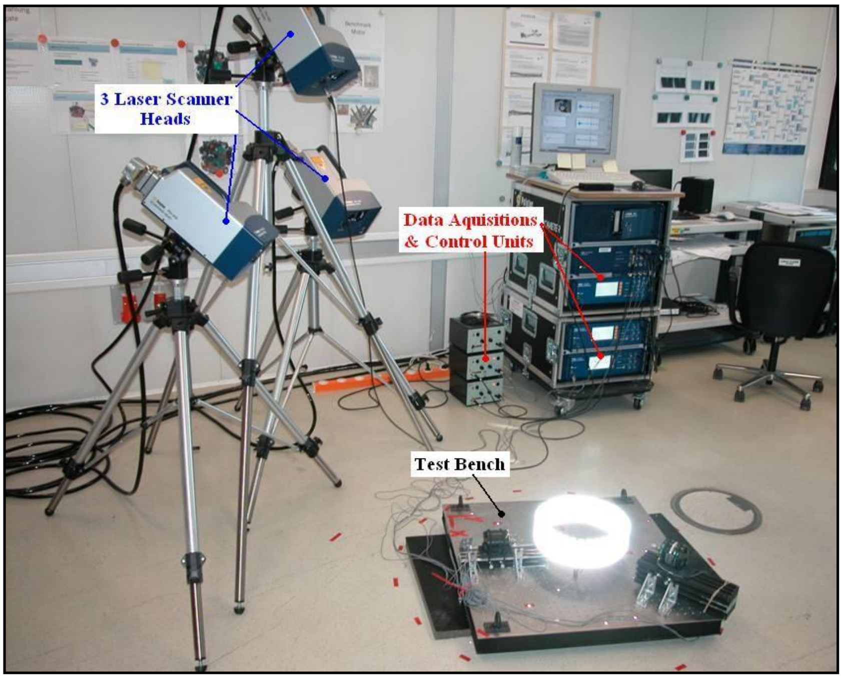

Figure 3-18: 3D Laser Scanning Vibrometer

Test bench description

The stator on the test bench was suspended as a free-free system on three spring struts or legs in order to record the vibration velocity in the three dimension coordinates. The excitation is achieved by two shakers which are mounted on the outer surface of the stator with one on the upper side and the second on the lower side. The shift angle between the shakers is 135°.

The shaker is glued onto the outer surface of the stator by using the HBM X60 adhesive bonding. The stator is completely covered by reflexion foils to achieve an optimal Signal to Noise Ratio “SNR” (see Fig. 3-19).

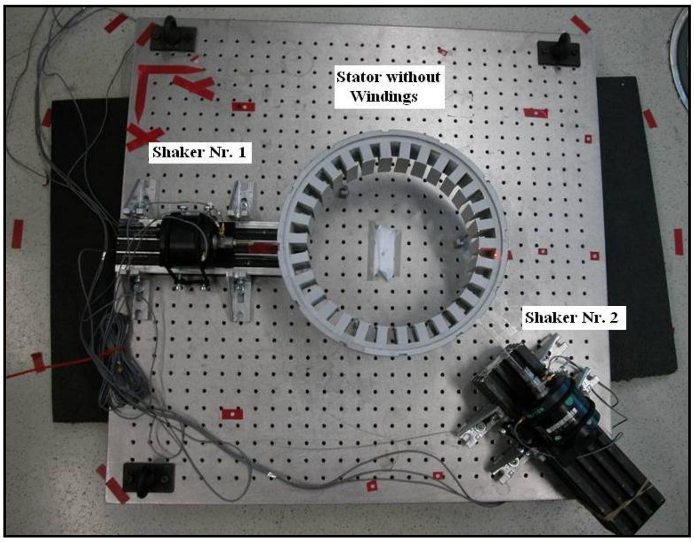

Figure 3-19: Stator with shakers on the test bench

Results

The vibration velocities of the stator surfaces are detected by the 3D Laser scanning system and displayed in domains of time and frequency. The detection is precisely performed by applying digital meshing nets on the stator surfaces and then recording the movement and velocity of each node existing on the nets (see Fig. 3-20). The shaker forces are measured by the PCB force sensors and are also displayed in time and frequency domains.

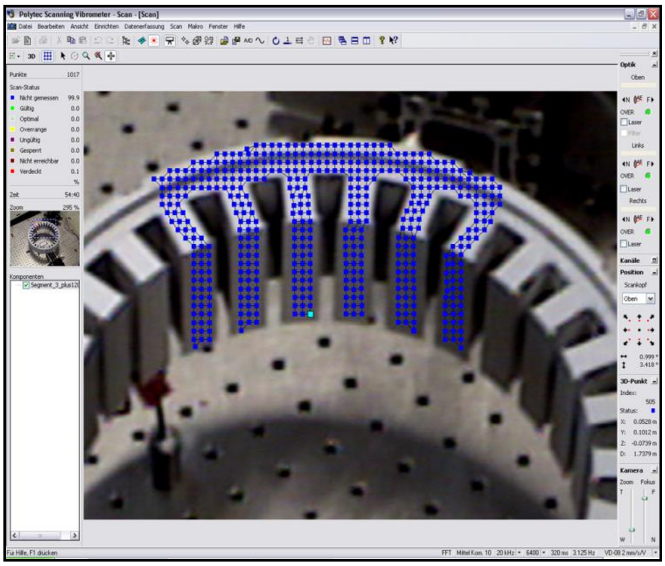

Punkte 1017

Scan-Status
Nicht gemessen 99.9
Gültig 0.0
Optimal 0.0
Overrange 0.0
Ungültig 0.0
Gesperrt 0.0
Nicht erreichbar 0.0
Verdeckt 0.1
%

Zeit 54:40

Zoom 295 %

Komponenten
☑ Segment_3_plus12

Scankopf: Oben
0.999 °
3.418 °

3D-Punkt
Index: 505
Status:
X: 0.0528 m
Y: 0.1012 m
Z: -0.0739 m
D: 1.7379 m

FFT Mittel Kom. 10 20 kHz 6400 320 ms 3.125 Hz VD-08 2 mm/s/V

Figure 3-20: Fine digital mesh for better accuracy

Correlation

To ensure reliable simulation results and to recognize the right boundary conditions which have to be applied between the stator frame and the teeth, and also between the teeth themselves, the simulation results with different boundary conditions have to be compared with the experimental data. In fact, it is not enough to find the right boundary conditions just by comparing the values of the Eigen frequencies with those of the ones obtained experimentally; but, in addition, they have to be correlated and validated using statistical methods like the Modal Assurance Criterion (MAC).The correlation actually measures the consistency of the data, guarantees realistic high fidelity simulations, and helps to decide which FE model has to be used for the computation of the modal and dynamic properties and later for the vibro-acoustic simulations. This correlation process also allows the quantification of the geometrical and dynamic (FRF and Modal) resemblance between the test model and the corresponding FE model.

Two FE Models of the stator with different boundary conditions are correlated with the experimental results. The stator frame and the teeth are firstly taken as one solid model. The second model is built by inserting a contact element between the stator frame and the outer surfaces of the teeth. Two correlations are performed to compare the results of each assumption with the measured data.

Correlation 1 “Solid Model”

The considered frequency range is decomposed into four domains (P1 to P4), which makes it possible to find out clearly all synchronized modes with their MAC values. The four domains have a frequency range from zero up to 6000 Hz in order to cover the first 10 radial modes. In this phase, the observation is focused on the MAC values because the simulation results used in the correlation are done with zero damping factors. This explains the difference between the simulation results of the Eigen frequencies and those of the experimental test. This point will be discussed further in the observation of the damping and friction effects on the simulations results. The MAC values for the solid model are shown on Tab. 3-5:

Mode	MAC values “solid”
2	1.0
3	0.9
4	0.8
5	0.7
6	0.5
7	0.5
8	0.3
9	0.7
10	0.5

Table 3-5: Correlation results between experimental and FEM solid model

The MAC values are greater or equal to 0.5 for all modes except for mode 8, which reveals a MAC value of 0.3. The correlation results show that the solid boundary condition can be applied for the simulation of the stator system. However, it is still necessary to look at the values of the Eigen frequencies in order to ensure that this boundary condition also gives an acceptable accuracy in the calculation of the Eigen frequencies.

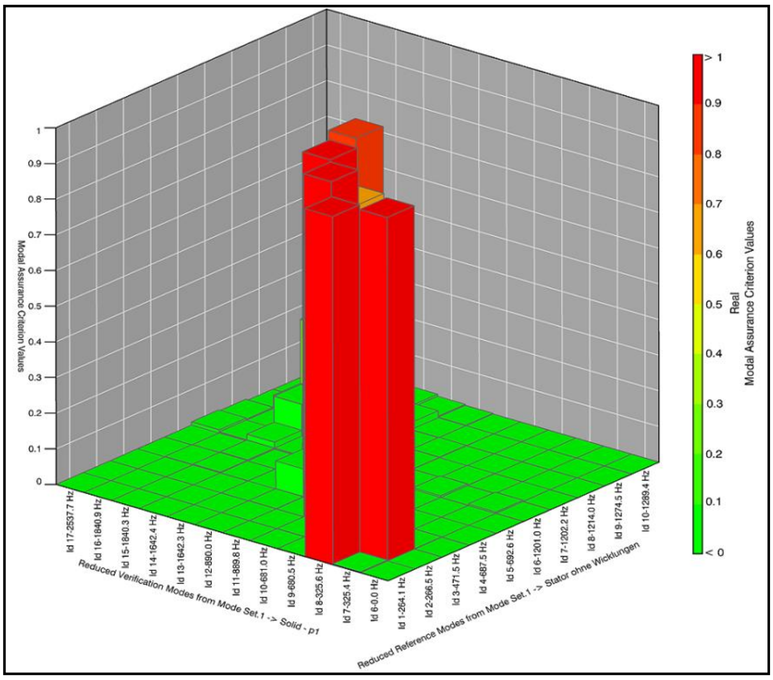

Figure 3-21: 3D representation of the P1 MAC values

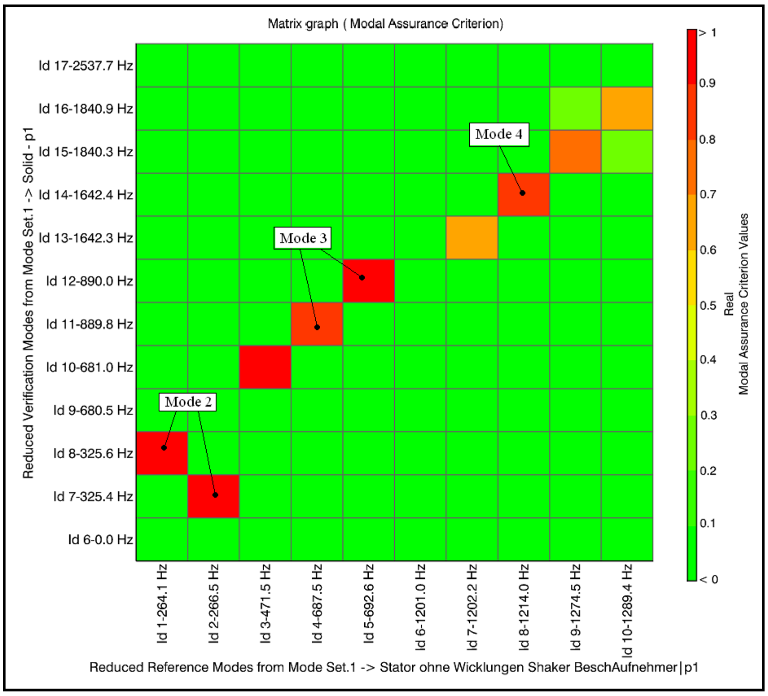

Figure 3-22: 2D representation of the P1 MAC values

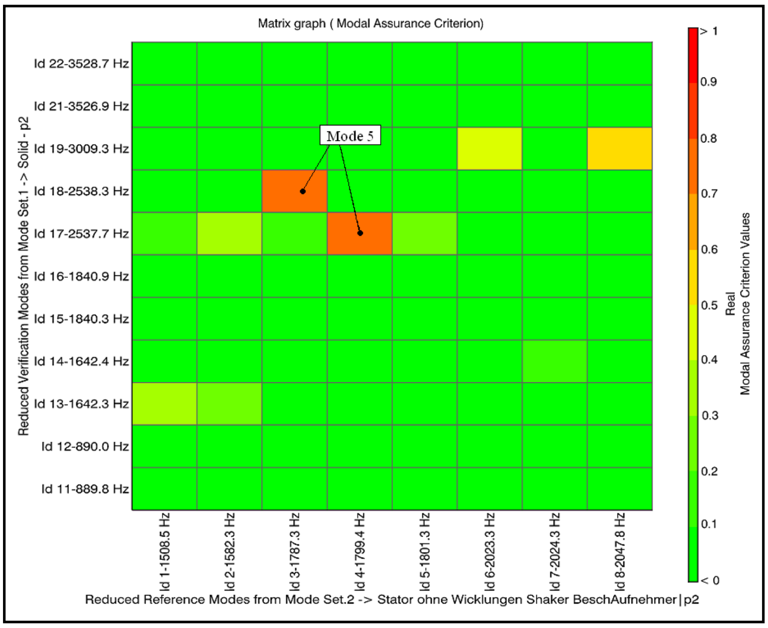

Figure 3-23: 2D representation of the P2 MAC values

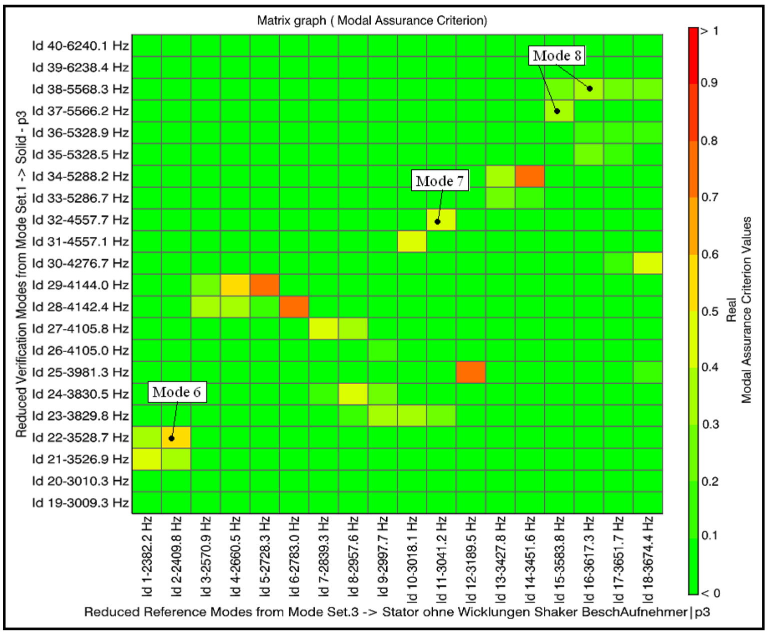

Figure 3-24: 2D representation of the P3 MAC values

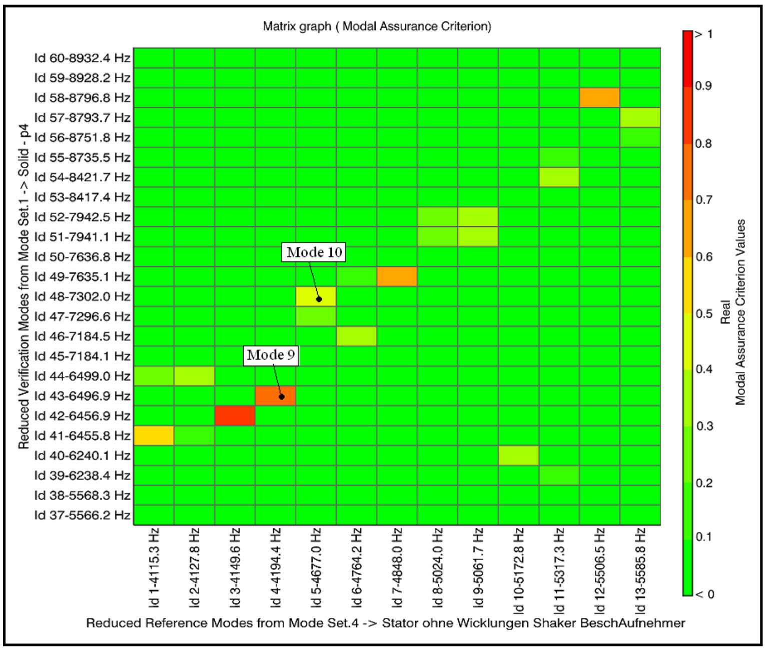

Figure 3-25: 2D representation of the P4 MAC values

Correlation 2 "Model with Contact Element"

The simulation is performed with zero-friction and damping factors. Table 3-6 shows the correlation results based on the MAC values. Modes 8 and 10 have MAC values of 0.3, but all the other modes reveal MAC values greater than or equal to 0.5.

Mode	MAC values "Contact"
2	1.0
3	0.7
4	0.9
5	0.6
6	--
7	0.5
8	0.3
9	0.5
10	0.3

Table 3-6: Correlation results between experimental and FEM model with contact element

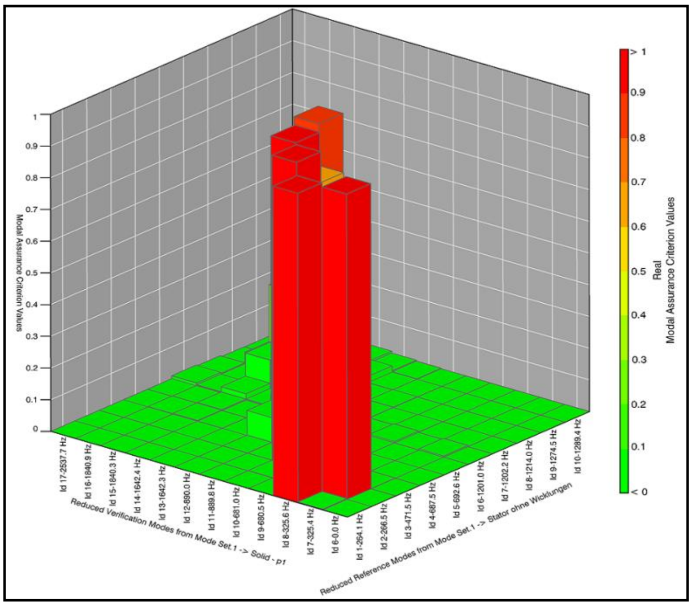

Figure 3-26: 3D representation of P1 MAC values

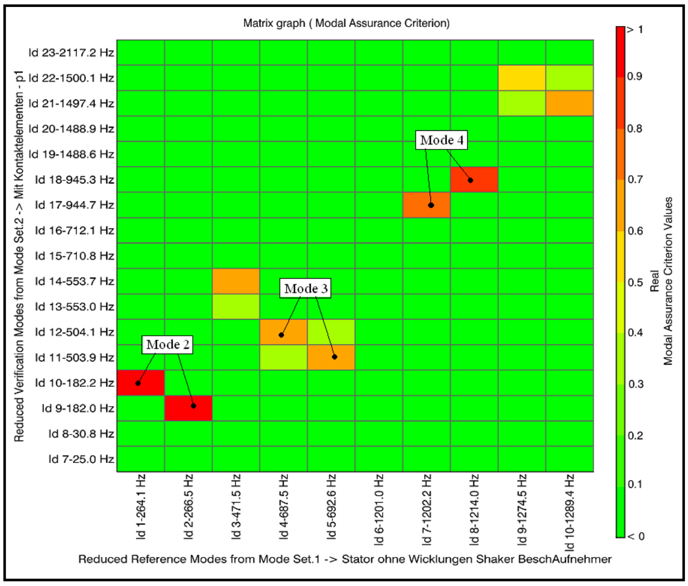

Figure 3-27: 2D representation of the P1 MAC values

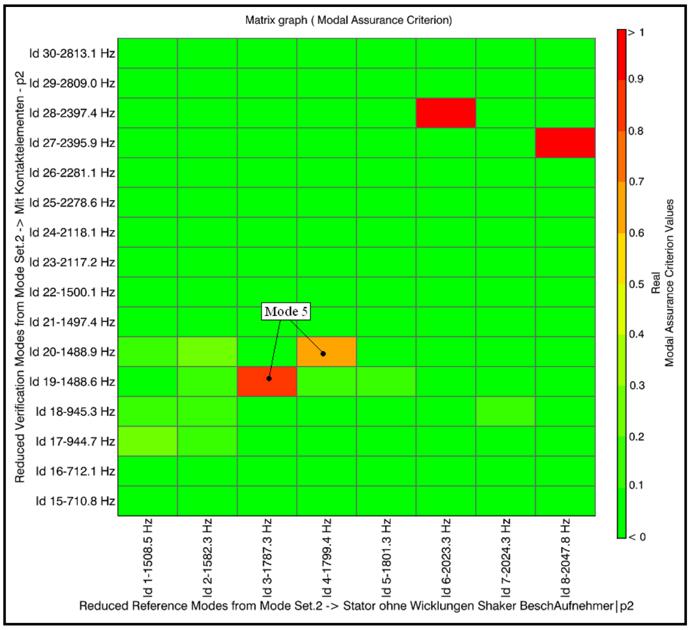

Figure 3-28: 2D representation of the P2 MAC values

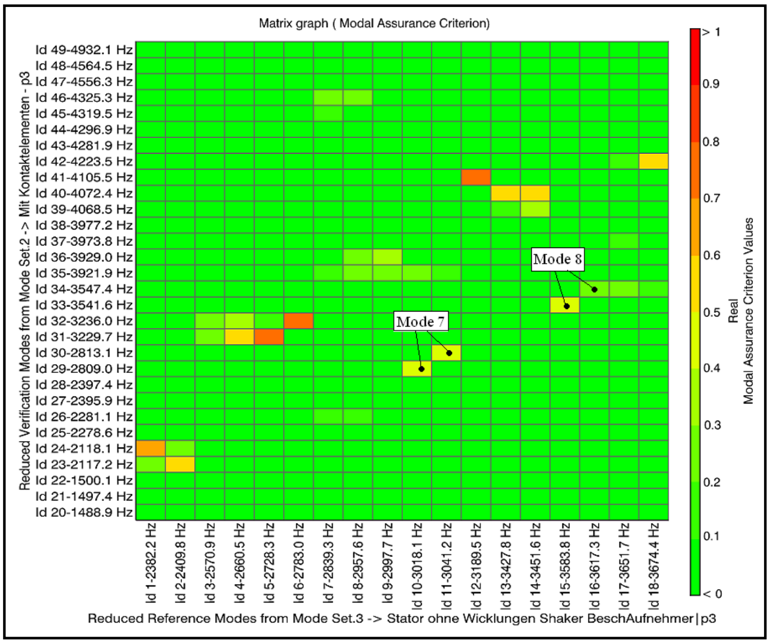

Figure 3-29: 2D representation of P3 MAC values

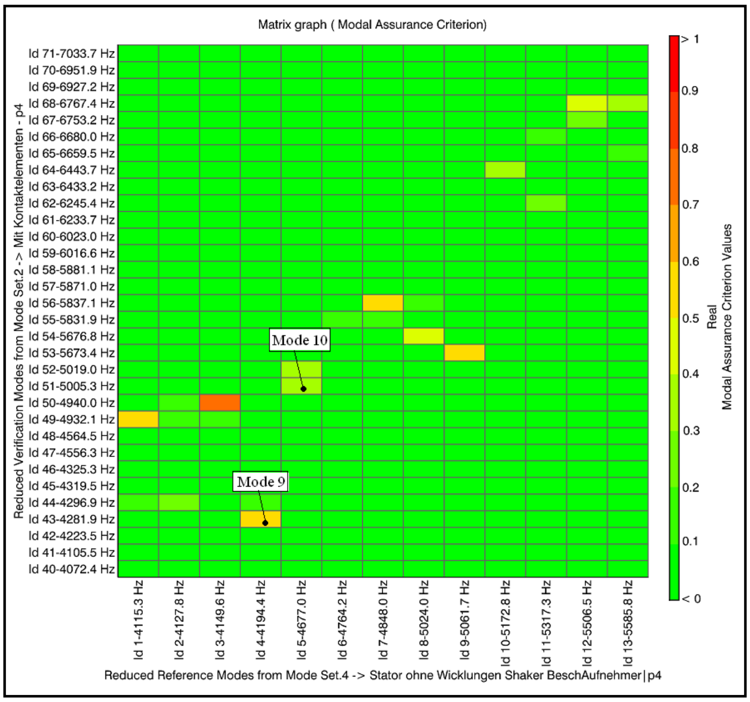

Figure 3-30: 2D representation of P4 MAC values

Effect of friction factor

Different options can be selected by inserting contact elements between surfaces in the FEM software. However, the simulation with contact elements used in the second correlation was performed by applying the frictional option which allows specifying a friction factor between the contact surfaces. Firstly, the friction factor was taken equal to zero; in this case the simulation values of the Eigen frequencies have revealed a considerable difference in comparison with the experimental results (see Tab. 3-7).

Mode	Eigen frequencies experimental (Hz)	Eigen frequencies with frictional contact factor zero
0	--	4223
2	264	182
3	693	504
4	1214	945
5	1799	1489
6	2410	2117
7	3041	2813
8	3617	3542
9	4194	4282
10	4677	5005

Table 3-7: Experimental results compared with those of the simulation “friction factor zero”

Mode	Simulation results of Eigen frequencies with different frictional factors (Hz)			
	0	**0.05**	**0.1**	**0.3**
0	4223	4200	4200	4200
2	182	340	310	310
3	504	860	860	860
4	945	1540	1540	1620
5	1489	2200	2400	2400
6	2117	2990	3160	3330
7	2813	3900	4050	4050
8	3542	4750	5000	5100
9	4282	5500	5700	6000
10	5005	6100	6550	6850

Table 3-8: Simulation results with different friction factors

In order to show the effect of the friction factor on the amplitudes of the Eigen frequencies, many simulations with different friction factors were performed. The results are shown in Table 3-8. It is clearly seen that the values of the Eigen frequencies with frictional factors different from zero show a large difference in comparison with the simulation results performed with a zero friction factor. In fact, for the modes m>2, which are called flexural modes (radial-circumferential modes) the friction factor affects the circumferential deformations and varies the structural properties. This introduces a differentiation in the values of the Eigen frequencies.

Effect of damping factors

It is necessary here to mention that the simulation results represented in Table 3-8 are done with zero damping factors. Therefore, in order to evaluate these results and to verify the values of the Eigen frequencies, many simulations have been performed using the experimental damping factors deduced from the modal test (see Tab. 3-9). Using the experimental damping factors, the circumstances of the simulations are then similar to those of the experimental test.

Mode Index	Experimental results of Eigen frequencies (Hz)	Simulation results of contact model with different friction factors including the effect of damping factors (Hz)			
		0	0.05	0.1	0.3
0	--	3545	3450	3523	3591
2	264	157	272	275	278
3	693	434	750	763	774
4	1214	711	1219	1257	1289
5	1799	1300	1763	2075	2129
6	2410	1500	2272	2371	2442
7	3041	2198	2946	3048	3344
8	3617	2813	3755	3851	4049
9	4194	3545	4226	4568	4723
10	4677	3922	4452	4905	5087

Table 3-9: Experimental and simulation results, including the effect of the damping factors

Experimental results of Eigen frequencies (Hz)	Simulation results of the solid model, without the inclusion of damping factors (Hz)	Simulation results of the solid stator including damping factors (Hz)
--	4277	3528
264	325	322
693	890	785
1214	1642	1324
1799	2533	2189
2410	3527	2538
3041	4557	3527
3617	5566	4557
4194	6497	5308
4677	7297	5568

Table 3-10: Simulation results of the solid model, including the effect of the damping factors

For the solid model, the simulation including the effect of the damping factor is performed and the results are shown in Tab. 3-10.

Interpretation

In order to define the correct boundary conditions in the stator system, it is necessary to perform a realistic simulation that takes into consideration all factors which can affect the simulation results. It means that the friction factors as well as the damping factors have to be considered in the simulation. In this way, it is then possible to compare the simulations results of both FEM models “solid and contact models” with the experimental results. It is also necessary to examine carefully the correlation results performed with both models.

Mode	MAC values “solid”	MAC values “contact”
2	1.0	1.0
3	0.9	0.7
4	0.8	0.9
5	0.7	0.6
6	0.5	--
7	0.5	0.5
8	0.3	0.3
9	0.7	0.5
10	0.5	0.3

Table 3-11: Correlation results of FEM models with the experimental test

Regarding the values of the Eigen frequencies, the FE model with contact elements including the experimental damping factors and with a frictional factor of “0.05” reveals better results than the solid model. A comparison with those of the experimental test is shown in Tab. 3-12.

Experimental results of Eigen frequencies (Hz)	Eigen frequencies for solid stator model including damping factors (Hz)	Eigen frequencies with contact element, friction factor "0.05" and including damping factors (Hz)
	3528	3450
264	322	272
693	785	750
1214	1324	1219
1799	2189	1763
2410	2538	2272
3041	3527	2946
3617	4557	3755
4194	5308	4226
4677	5568	4452

Table 3-12: Comparison of the FEM results with those of the experimental test

So it is possible to declare that the best boundary conditions which can be used in the simulation of the stator system are:

1. Inserting contact elements between the stator frame and the outer surfaces of teeth.
2. Selecting the frictional option for the contact type and applying a non-zero friction factor.
3. Applying non-zero damping factors (it is preferable to use the damping factors deduced experimentally).
4. For the individual tooth concept in stator, the teeth can be simulated as solid stator core without any partition and without applying any contact element between the teeth. The confirmation of this is based only on the experimental results of the experimental modal analysis. However, it is necessary here to mention that the pressing forces and the tolerances have to be verified and confirmed before and during the assembly process.

3.1.4 Boundary Conditions in Transmission

In order to be realistic in the evaluation of the Eigen frequencies, the stator simulations need to take into account the external boundary conditions between the stator systems, especially the stator frame with the transmission housing. Also, the tolerances as well as the mounting and the attachment method of the stator system in the transmission housing play an important role in the definition of these external boundary conditions.

There are actually four possible constraints which can be activated, depending on the mounting method and on the design of the transmission housing. Firstly, the stator can be supported in radial direction based on the ribs of the seal rings on both sides. Also, it can be supported axially by subjecting an axial pressure on the front circumferential area of the stator frame from the combustion motor side; from the transmission side, the chamfered wedge area of the stator frame meets a correspondent area on the transmission housing (see Fig. 3-31).

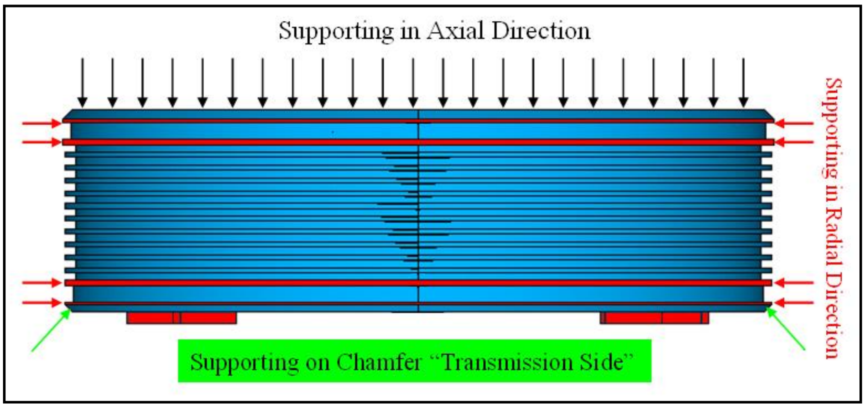

Figure 3-31: The possible external boundary conditions

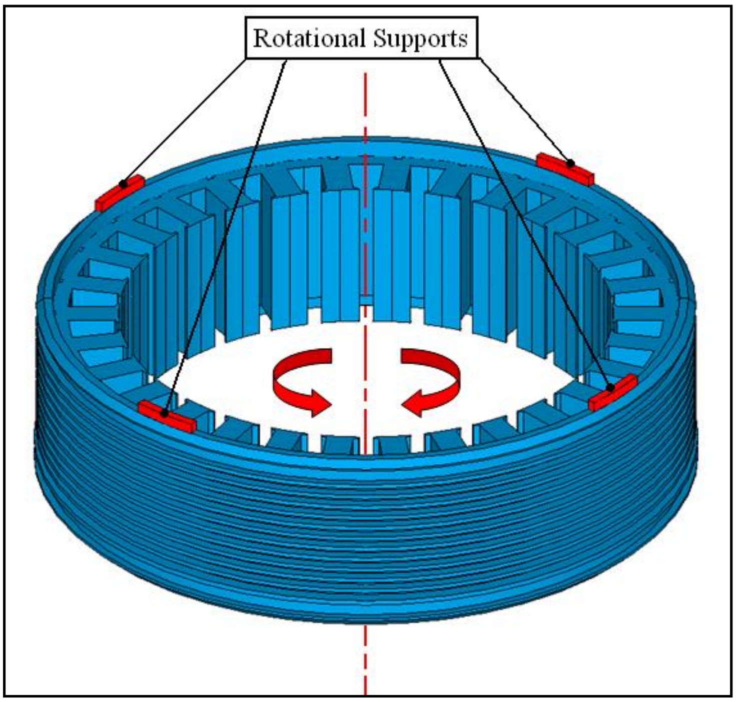

Figure 3-32: Rotational supports

The stator system is not allowed to rotate due to four noses which go through four slots in the front side of the transmission bell housing (see Fig. 3-32). To show the effect of each constraint on the values of the Eigen frequencies, many simulations have been performed on the solid model without including the damping effect.

According to Table 3-13, the axial and rotational supports do not affect the values of the Eigen frequencies. This means that the system can be modeled with or without these restrictions for the modal analysis as well as for the harmonic analysis.

The displacement constraint applied on the chamfered wedge shifts the Eigen frequencies strongly upward for all modes except for modes 0 and 10, where the values are not highly changed. However, applying radial constrictions on the model does not allow the radial modes to appear anymore (see Tab. 3-14). This makes these radial restrictions unrealistic and inapplicable, and this is because the radial modes are the most critical types of behavior which can be firstly excited in such stator designs.

Returning to the results of the displacement constraint applied on the chamfered wedge, the tolerances play an important role here because they can be greater than the mode deformations resulting in the harmonic analysis. At any rate, this constraint restricts the radial deformation and the produced structure-borne sound. Furthermore, this constraint does not affect significantly the Eigen frequencies of modes 0 and 10, which represent the critical modes from electromagnetic side. Thus, in order to compute the maximum deformations produced due to the radial magnetic forces located in the air gap and to evaluate the maximum behavior of vibrations and noises of the machine, this constraint has been disregarded in the harmonic analysis; keeping in mind that this constraint has to be considered in case of another electromagnetic design where the Eigen frequencies of the dominant modes could be highly affected by it.

Mode	Simulation results of Eigen frequencies	
	Free-Free	Axial & rotational supports
0	4277	4263
2	325	325
3	890	890
4	1642	1642
5	2533	2538
6	3527	3528
7	4557	4559
8	5566	5569
9	6497	6500
10	7297	7299

Table 3-13: Results of a free-free model and model with axial and rotational supports

Mode	Simulation Results of Eigen Frequencies	
	Supports on Chamfer	Radial Supports
0	4166	--
2	2157	--
3	2670	--
4	3054	--
5	3709	--
6	4500	--
7	5368	--
8	6234	--
9	7028	--
10	7687	--

Table 3-14: Simulation results with radial supports and supports on chamfered wedge

3.2 Harmonic Response Analysis

The harmonic response analysis is a technique used to apply harmonic loads on the structures in order to calculate the structure response at several frequencies and to obtain a representation of some response quantity like displacements and surface velocities versus frequency.

It is profitable for such applications to use the mode superposition analysis which utilizes the results of the modal analysis done previously and calculates the deformations and the stresses based on the resulting natural frequencies.

3.2.1 Force Shapes for Modes

To calculate the deformations for every mode, the magnetic forces need to be distributed on the inner surfaces of the teeth as harmonic forces. It means that the force amplitudes depend on time and position. These forces are inserted in ANSYS Workbench as equations that are functions of the mode index, the stator radius, and the maximal force amplitude. This formula has been already introduced in the electromagnetic analysis in Chapter 2. The frequencies are automatically recognized by ANSYS workbench based on the modal analysis. It means that there is no need to insert the frequencies in these equations because they are already considered by ANSYS as harmonic functions.

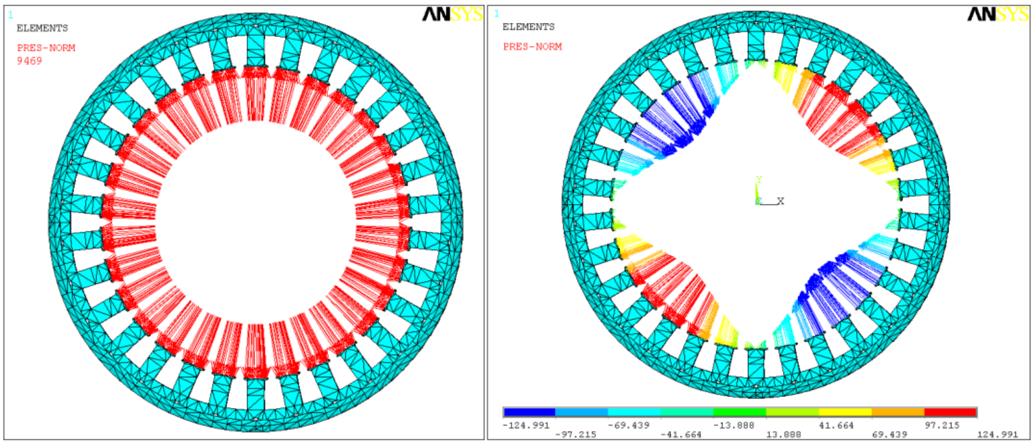

Figure 3-33: Force distribution for mode 0 and 2

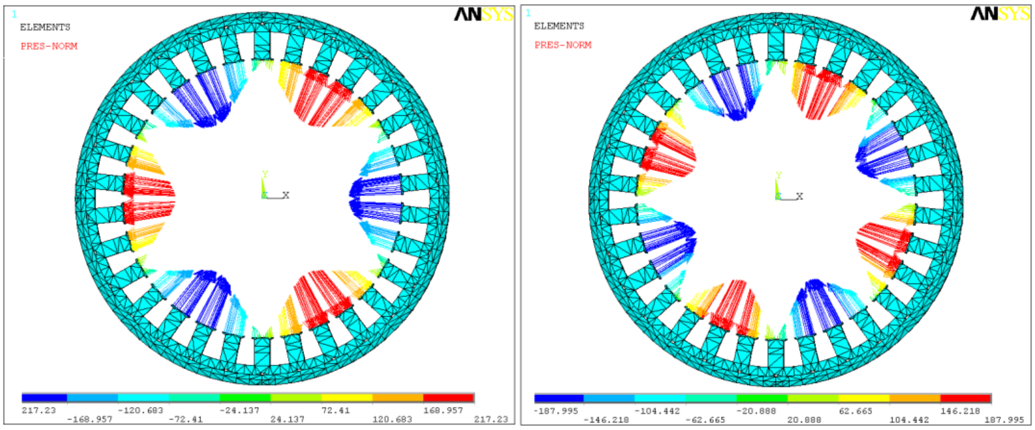

Figure 3-34: Force distribution for mode 3 and 4

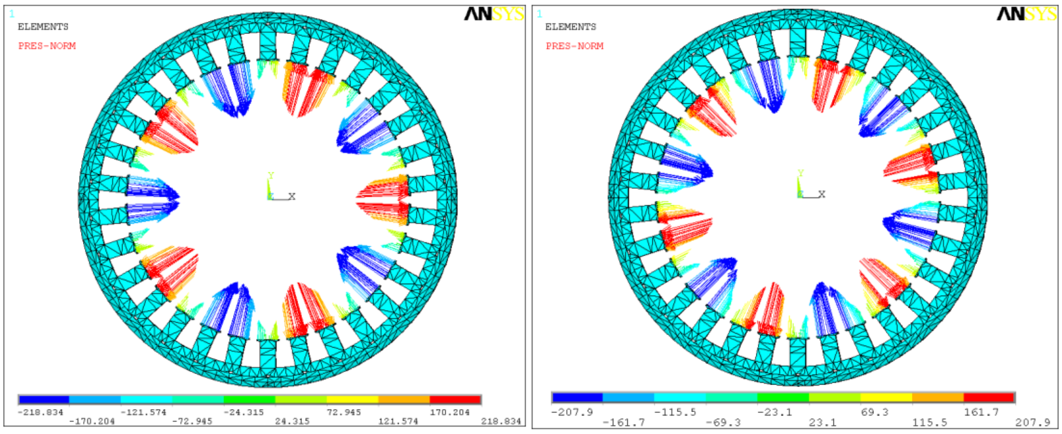

Figure 3-35: Force distribution for mode 5 and 6

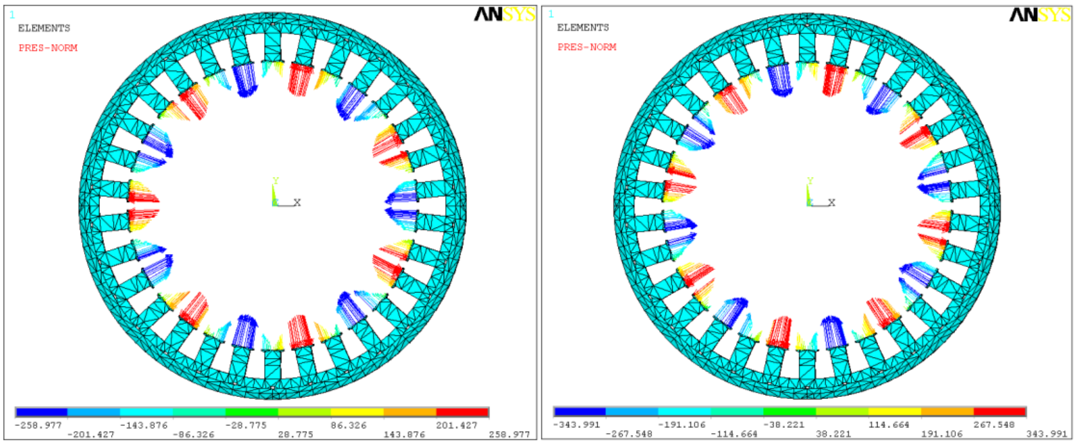

Figure 3-36: Force distribution for mode 7 and 8

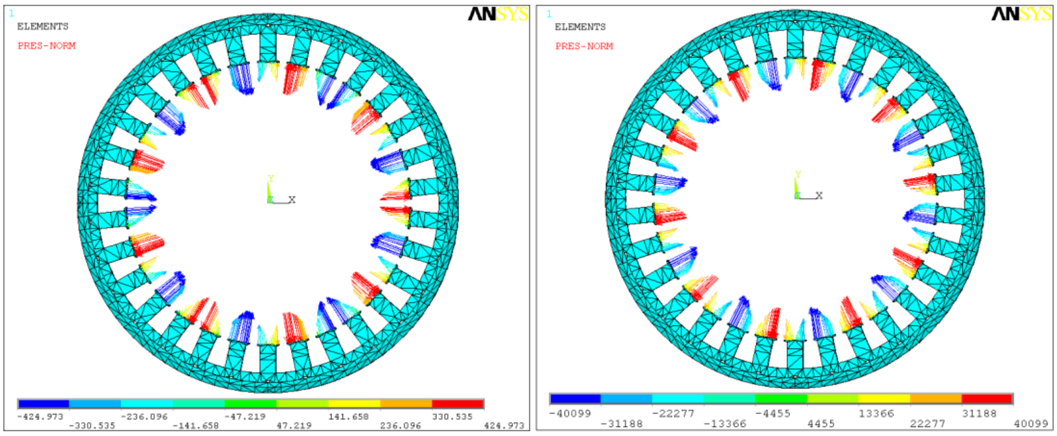

Figure 3-37: Force distribution for mode 9 and 10

3.2.2 Harmonic Results

The deformation results show that mode 0 and mode 10 reveal maximum deformations in comparison with other modes. It is also clear that mode 2 reveals a considerable deformation even though its Eigen frequency does not exceed 300 Hz (see Tab. 3-15); it means that this eccentricity mode has to be carefully treated, regardless of the small amplitude of its force.

Mode Index	FEM (contact) with damping factors (Hz)	deflection (mm)
0	3450	0.000134
2	272	0.000103
3	750	0.000028
4	1219	0.0000069
5	1763	0.0000044
6	2272	2.1469E-06
7	2946	1.996E-06
8	3755	2.068E-06
9	4226	2.0002E-06
10	4452	0.000136

Table 3-15: Mode deformations resulting in the harmonic analysis

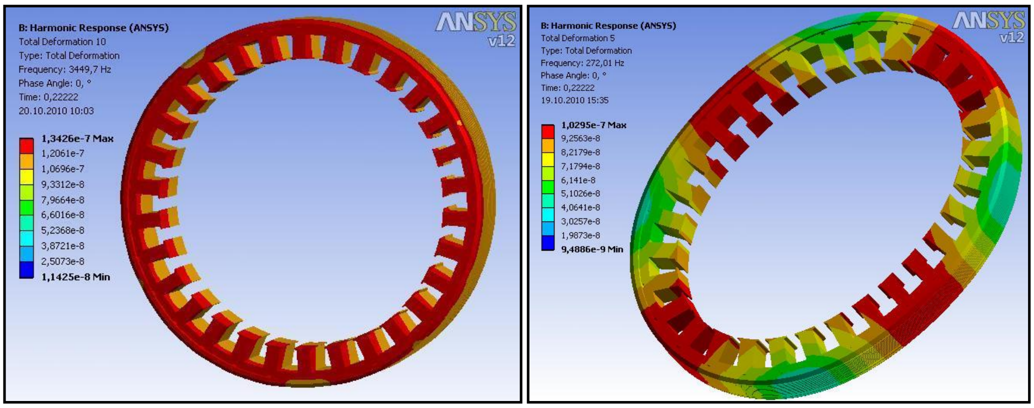

Figure 3-38: Deformation results of mode 0 and 2

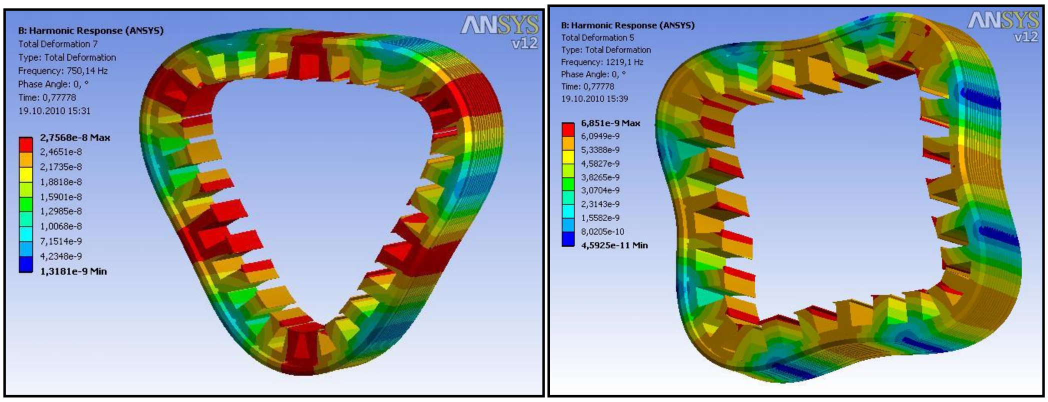

Figure 3-39: Deformation results of mode 3 and 4

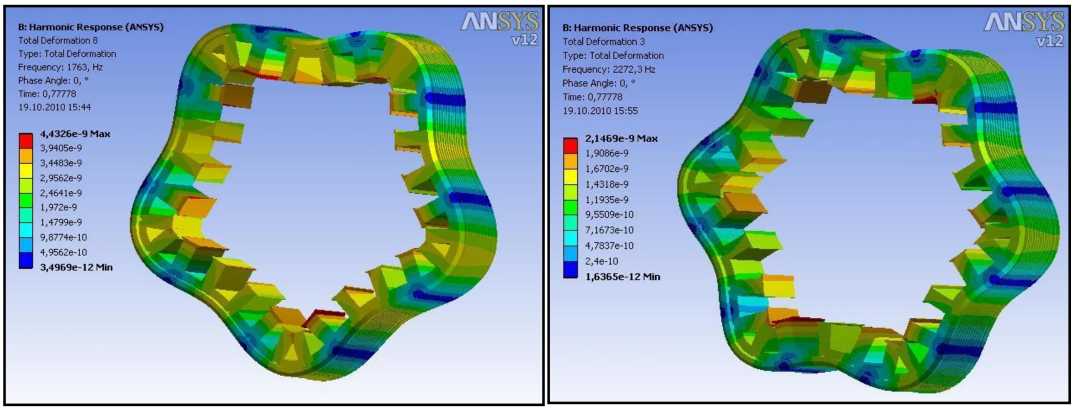

Figure 3-40: Deformation results of mode 5 and 6

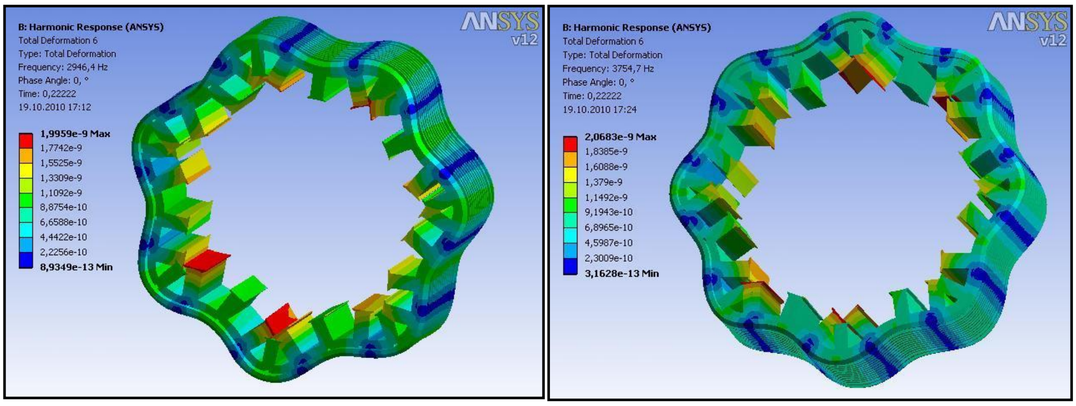

Figure 3-41: Deformation results of mode 7 and 8

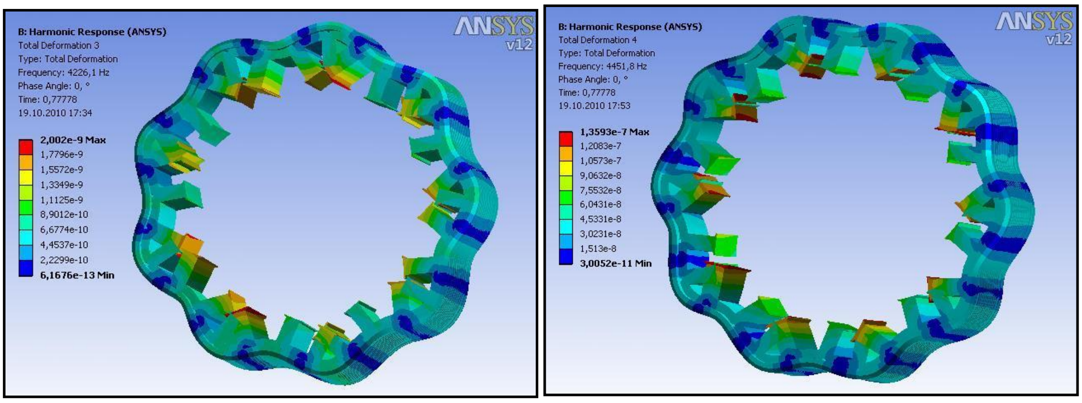

Figure 3-42: Deformation results of mode 9 and 10

4 Structural Vibrations and Acoustics

4.1 General Acoustics

Sound is defined as the pressure variations or oscillations in an elastic medium like gas, liquid and solid. It can be described by mechanical waves with a frequency range from 16 Hz to 16 KHz. This range represents the human hearing domain and it may be up to 20 KHz depending on the person's age. The best sound sensitivity lies in the range of 1000 Hz to 6000Hz [Kar2007] (see Fig. 4-1). Since the infrasound field is located between 0 Hz and 16 Hz, the ultrasound field is positioned to be between 20 KHz to 1GHz. The area above the 1 GHz domain is known as the hypersonic field.

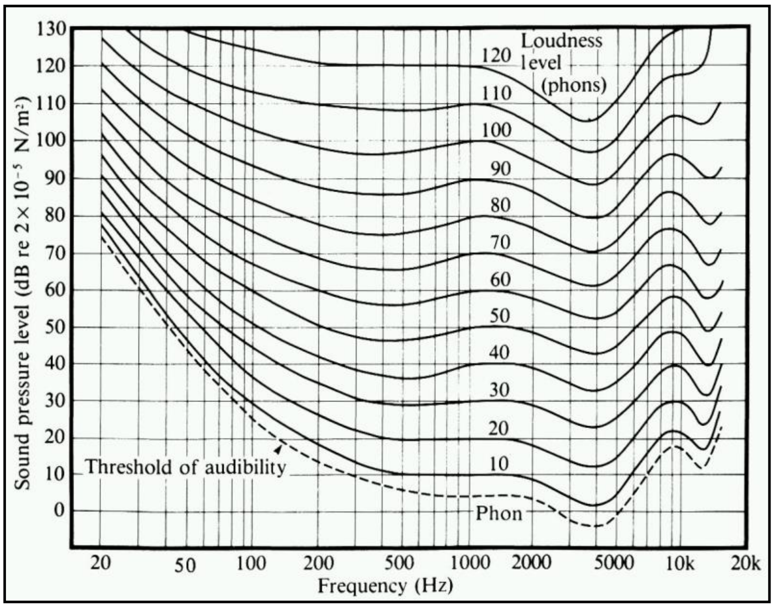

Figure 4-1: The Fletcher-Munson curves of equal loudness (1933)

Sound can be differentiated by four types [Eic2007]:

1- Tone: is constituted by one sinusoidal wave with constant frequency.
2- Ring: results from the interaction of many tones with different frequencies.
3- Noise: results from waves of different frequencies with different amplitudes.
4- Bang: results from waves with different frequencies but almost constant amplitudes.

Noise generation: Noise can be defined as "disagreeable or undesired sound or other disturbance". The understanding of noise generation mechanisms is very essential for analyzing the process of noise. The generation process can be classified into two different types: direct and indirect generation (see Fig. 4-2).

Direct noise generation: the transient fluid phenomena lead to pressure fluctuations and consequently to sound or noise radiation without passing through a structural vibration process.

It is caused primarily by the flow streaming processes which excite the air particles and set them into vibration [Mös2007].

Indirect noise generation is carried out by seismic radiation of structures that are excited by alternating forces, and thus driven into vibration [Mös2007]. The excitation can be mechanic, magnetic, fluid mechanic or any other excitation mechanism. These structural vibrations stimulate the emission from the surfaces of the structures to generate indirectly the radiated noise [Mor2010].

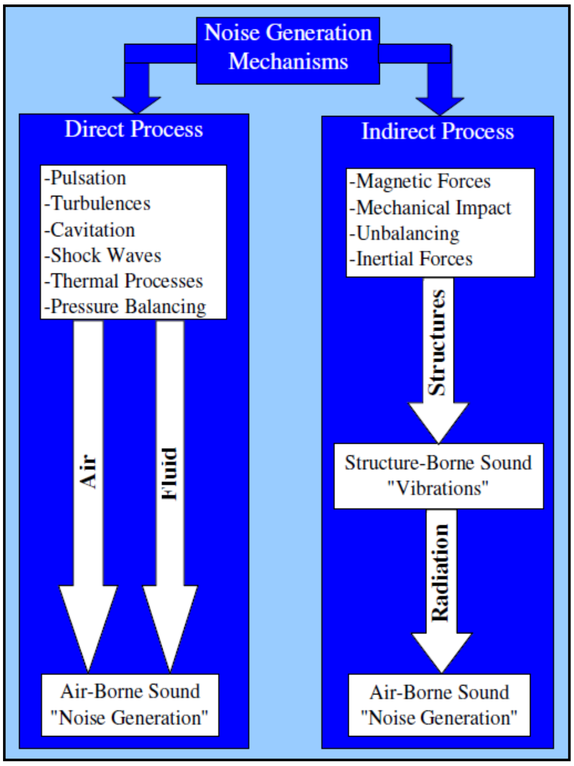

Figure 4-2: Direct and indirect noise generation

4.2 Theoretical Foundations

A major portion of noise or sound exciting the air originates from, or is transmitted through, vibrating solid structures. The field of physics, which encompasses the vibrations and waves in solid structures, is termed to be structure-borne sound. In many cases it is the structure-borne sound that is responsible for the resulting sound in air (or sound in liquids). Even the transmission through walls, ceilings, windows, etc. is essentially a structural problem [Mös2009].

The structure borne sound plays a very important role in building acoustics, in noise control and in vehicle acoustics. It is a very complex field, but its structural acoustic process can be described by four main stages as shown in Fig. 4-3.

The first stage, “Generation”, comprises the origin or the external mechanism of oscillation which is responsible for the vibration generation. The second stage, “Transmission”, represents the transfer of external excitations from the generation mechanism to the structures. The third stage, “Propagation”, covers the distributed energy throughout the structural system. The fourth stage, “Radiation”, is recognized when a part of the vibrational energy is emitted into the air as audible sound or noise.

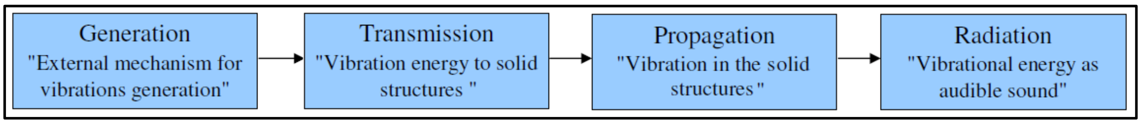

Figure 4-3: Stages of the structural acoustic process

Due to the complexity of this process, it is necessary to deal with each stage separately.

The structure excitation in the generation phase is usually performed by applying external forces which result from mechanical, magnetic or inertial causes. These forces are transferred to the solid structures and propagated in the form of vibration all over the structure body. Then the surfaces of the structure vibrate and emit into the surrounding air an undesirable sound which we call “noise”.

The generation of waves directly in the air by speaking, by playing music, or by the propagation of waves from vibrating surfaces of solid structures in the surrounding air is referred to as “airborne sound”.

4.2.1 Waves

A vital and fundamental difference exists between sound waves in air and sound waves in structures. In fact, a “wave” can be defined as a periodic disturbance in a medium. This wave transmits energy from one point to another and needs two elements for its realization: a source and a medium of propagation.

A gas (or a liquid) reacts with a change in pressure if its volume is changed [Mös2009]. However, a solid stores energy through the change in volume and in form; consequently, solids experience a higher number of wave types than fluids or gases.

Sound waves propagating through air are just longitudinal waves. They consist of a series of pressure fluctuations above and below atmospheric pressure.

4.2.2 Variables in Acoustic

In acoustic, there are some variables of particular relevance which are always used to describe the sound and noise within a space.

Wave length (λ_s)

The distance over which the shape of a wave repeats itself is its wave length. It depends on the frequency (f) and the speed of sound propagation (c).

$$\lambda_s = c / f \, , \tag{4.1}$$

where: (c) in m/s and (f) in Hz.

Wave number

The wave number (k_n) is the number of waves per unit meter.

$$k_n = 2\pi / \lambda_s \tag{4.2}$$

Speed of sound

The speed of sound is the distance travelled during a unit of time by a sound wave propagating through an elastic medium. It is a constant result from the multiplication of the wave length (λ_s) by the frequency (f).

$$c = \lambda_s f \tag{4.3}$$

The speed of sound is usually referred to as the speed of sound waves in air, but the speed of sound in solids and fluids is faster than in air. It varies from substance to substance.

Speed of sound in solids

The speed of sound waves in solids depends on the stiffness of the solid material as well as on its compressibility and density.

For solids with dimensions much greater than the wave length, the speed of sound of the longitudinal wave depends only on the density, and the Young modulus.

$$c_{SL} = \sqrt{\frac{E}{\rho}} \tag{4.4}$$

In most cases where one dimension is smaller than the wave length and then a contraction in the cross-section occurs, the Poisson's ratio has to be included in the equation of the sound speed [Kar2007].

$$c_{SL} = \sqrt{\frac{E(1-\nu_p)}{\rho(1-\nu_p-2\nu_p^2)}} \tag{4.5}$$

For transverse wave, the speed of sound is determined by using the shear modulus G_m instead of the Young modulus.

$$c_{ST} = \sqrt{\frac{G_m}{\rho}} \tag{4.6}$$

As is the case with the longitudinal wave, the Poisson’s ratio can be also included in the equation of the speed of sound for a transversal wave [Kar2007]:

$$c_{ST} = \sqrt{\frac{G_m}{2\rho(1+\nu_p)}} \tag{4.7}$$

Speed of sound in air

The speed of sound in air (c_a) is determined by the bulk modulus K and the density (ρ):

$$c_a = \sqrt{\frac{K}{\rho}} \tag{4.8}$$

The bulk modulus is defined by the difference in pressure (Δp_s) and the relative change in volume ($\Delta V/V$) [Eic2007]:

$$K = -\frac{\Delta p_s . V}{\Delta V} \tag{4.9}$$

The pressure change in the air is quick, so the heat during the compression is not dissipated. Therefore, by an adiabatic compression, the following relation can be used:

$$p_s V^{k_T} = const., \tag{4.10}$$

where (k_T) is the adiabatic exponent.

The partial differentiation of Eq. 4.10 yields:

$dp_s V^{k_T} + k_T\, p\left(V^{k_T}\right)^{-1} dV = 0$, subsequently:

$$\frac{dV}{dp_s} = -\frac{V}{k_T\, p_s} \tag{4.11}$$

Applying Eq. 4.11 to Eq. 4.9, the bulk modulus yields:

$$K = k_T\, p_s \tag{4.12}$$

For ideal gases the pressure can be expressed by:

$$p_s = \rho R' T, \tag{4.13}$$

where (R') is the universal gas constant, T is the temperature in Kelvin (K°).

Using Eq. 4.13 and Eq. 4.12, the speed of sound in air can then be expressed as follows:

$$c_a = \sqrt{kR'T} \tag{4.14}$$

According to Eq. 4.14, there is also an approximation for calculating the speed of sound:

$$c_a = (331.4 + 0.6\upsilon / C°) m/s, \tag{4.15}$$

where (υ) is the temperature in Celsius (C°).

Sound pressure (p_s)

The pressure deviation above the atmospheric value occurring during the wave propagation is defined as the sound pressure of a wave.

Sound particle velocity (v_s)

The alternating velocity of oscillating particles around their original positions as they transmit waves in a medium such as air is defined by the sound particle velocity. It should not be confused with the speed of the wave as it passes through the medium.

Impedance

The term impedance is often used in engineering. In relation to structural systems, the mechanical impedance can always be used to determine the behavior and the transfer functions of the structures. In acoustics, impedance relates the complex amplitude of fluid pressure, or the corresponding force, to the complex amplitude of fluid particle velocity or volume velocity [Fah2003].

Mechanical impedance

The term mechanical impedance is related principally to solid structures. It is the ratio of the complex amplitude of a sinusoidally varying force to the complex amplitude of the resulting velocity at a point on a vibrating object [Ros2007]

$$Z_{mech} = \frac{F}{v_s}, \tag{4.16}$$

with (F) being the force and (v_s) being the particle velocity.

Acoustic impedance

It expresses the ratio of complex amplitude of harmonic pressure (or associated force on a surface) to the associated particle velocity (or associated volume velocity through a surface). It takes a variety of forms, and the terminology used to label them varies from one source to another. Here only the necessary definitions will be introduced; more information and details are available in [Fah2003].

a) Specific acoustic impedance

It can be also called the specific radiation impedance or the specific field impedance and involves the ratio of sound pressure to particle velocity [Fah2003] [Ben2004]. However, the ratio of the sound pressure to the outward normal component of particle velocity at a vibrating surface is defined by the normal specific acoustic impedance

$$Z_{rad} = \frac{\hat{p}_s}{\hat{v}_s} \quad . \tag{4.17}$$

b) Characteristic specific acoustic impedance (characteristic field impedance)

The specific acoustic impedance or the field impedance in a plane wave is a quantity that is specific to the medium which is called the characteristic field impedance [Bla2008]. For air, it is equal to $Z_a = \rho c_a$.

Sound intensity

Instantaneous sound intensity is a vector quantity determined as the product of instantaneous sound pressure at a point and the associated particle velocity [Iso9614].

$$\vec{I}_s(t) = p_s(t).\vec{v}_s(t) \tag{4.18}$$

The sound intensity is the time-averaged value of the instantaneous sound intensity ($\vec{I}_s(t)$).

$$\vec{I}_s = \lim_{T\to\infty}\frac{1}{T}\int_0^T \vec{I}_s(t)dt \,, \tag{4.19}$$

where (T) is the integration period.

However, the normal sound intensity is the component of the sound intensity in the direction of the normal vector defined by the unit normal vector ($d\vec{S}$).

$$\vec{I}_n = \vec{I}_s.d\vec{S} \tag{4.20}$$

It is expressed as watts per square meter (W/m^2).

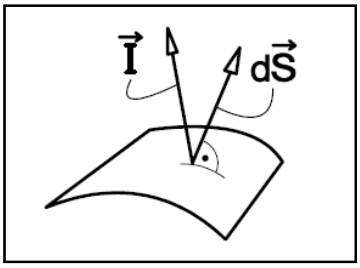

Figure 4-4: The unit normal vector $d\vec{S}$ [Kar2007]

Sound power

The total sound energy emitted by a source per unit time is the sound power. It is obtained by integrating the sound intensity over an imaginary surface surrounding a source [Coh2004].

$$P_s = \int_A I_n dA, \tag{4.21}$$

where (P_s) is the sound power, (I_n) the normal sound intensity and (dA) the element unit area of (A).The result of the integral obviously depends on the sound waveforms.

Radiation efficiency

It is an important and useful quantity for describing the radiated sound power from the vibrating structures. It is defined as the ratio of the radiated sound power (P_s) to the maximal possible sound power of a matched source of area (A) and the averaged mean square velocity (v_s):

$$\sigma_s = \frac{P_s}{\rho c_a A |\bar{v}_s|^2}. \tag{4.22}$$

4.2.3 Levels and Logarithmic Scales

Levels are the logarithmic ratios of fields and energy quantities to similar reference quantities. They were introduced in order to compress a wide range of several orders of magnitude of a physical quantity by a logarithmic scale. The following level definitions are common in acoustics, with lg = log10.

Sound pressure level (L_p)

It is ten times the logarithm to the base 10 of the ratio of the mean-square sound pressure to the square of the reference sound pressure. The reference sound pressure is p_{ref}=20.10^{-5} Pa.

$$L_p = 10.\lg \frac{p^2}{p_{ref}^2} \tag{4.23}$$

Sound velocity level (L_v)

It is ten times the logarithm to the base 10 of the ratio of the mean-square sound particle velocity to the square of the reference sound particle velocity. The reference sound particle velocity is v_{ref}=5.10^{-8} m/s.

$$L_v = 10.\lg \frac{v_s^2}{v_{ref}^2} \tag{4.24}$$

Normal sound intensity level (L_{I_n})

It is the logarithmic measure of the unsigned value of the normal sound intensity (I_n) given by:

$$L_{I_n} = 10.\lg\frac{I_n}{I_0}, \tag{4.25}$$

where I_0 is the reference sound intensity (I_0=10^{-12} W/m^2).

Sound power level (L_w)

It is the logarithmic measure of the sound power generated by a source and is given by:

$$L_w = 10.\lg\frac{P_s}{P_0}, \tag{4.26}$$

where is (P_s) the magnitude of the sound power of the source, (P_0) the reference sound power (P_0=10^{-12}W).

4.2.4 Wave Equation

For ideal compressible fluids (liquids or gases), the Navier-Stokes equation represents the base of the linear acoustic equations. If viscosity and thermal conductivity are neglected, the Navier-stokes equation can be reduced to the Euler equation:

$$\rho\frac{Dv_s}{Dt} = -\nabla p_s + g\rho, \tag{4.27}$$

where (v_s) is the particle velocity, (ρ) the density of air, (p_s) the sound pressure and (g) the acceleration associated with gravity.

Neglecting the gravity effect at the outset, the linearization of Eq. 4.27 leads to:

$$\rho\frac{\partial v_s}{\partial t} = -\nabla p_s. \tag{4.28}$$

Using the energy equation for an isentropic flow, the mass conservation equation for fluid can be expressed as:

$$\frac{Dp_s}{Dt} + \rho c_a^2 \nabla.v_s = 0. \tag{4.29}$$

The derivation of this equation is described in detail in [Ros2007].

Assuming a zero ambient fluid velocity and then a constant ambient pressure, the linearization of Eq. 4.29 leads to:

$$\frac{\partial p_s}{\partial t} + \rho c_a^2 \nabla.v_s = 0. \tag{4.30}$$

The partial derivative of Eq. 4.30 yields:

$$\frac{\partial^2 p_s}{\partial t^2}+\rho c_a^2\nabla.(\frac{\partial v_s}{\partial t})=0\,. \tag{4.31}$$

Applying Eq. 4.28 to Eq. 4.31results in:

$$\frac{\partial^2 p_s}{\partial t^2}-\rho c_a^2\nabla.\left(\frac{1}{\rho}\nabla p_s\right)=0\,. \tag{4.32}$$

This last equation can be also arranged as:

$$\nabla.\left(\frac{1}{\rho}\nabla p_s\right)-\frac{1}{\rho c_a^2}\frac{\partial^2 p_s}{\partial t^2}=0\,. \tag{4.33}$$

When the ambient density is independent of position, then Eq. 4.33 can be expressed by:

$$\nabla^2 p_s-\frac{1}{c_a^2}\frac{\partial^2 p_s}{\partial t^2}=0\,. \tag{4.34}$$

Equation 4.34 is termed the wave equation of linear acoustics.

For disturbances that vary sinusoidally with time and propagate without change of frequency, a complex number representation can be utilized; this means that the acoustic pressure and the particle velocity can be written as follows:

$$p_s=\mathrm{Re}(\hat{p}_s e^{-i\omega t}) \tag{4.35}$$

$$v_s=\mathrm{Re}(\hat{v}_s e^{-i\omega t})\,. \tag{4.36}$$

Here ($\hat{p}_s$) and ($\hat{v}_s$) are the complex amplitude of the acoustic pressure and particle velocity which vary in general with position.

The time derivatives of all field variables can then be deduced using the substitution:

$$\frac{\partial}{\partial t}\rightarrow -i\omega$$

Applying this to Eq. 4.28 and Eq. 4.30:

$$-i\omega\hat{p}_s+\rho c^2\nabla.\hat{v}_s=0\,, \tag{4.37}$$

$$i\omega\rho\hat{v}_s=\nabla\hat{p}_s\,. \tag{4.38}$$

Also Eq. 4.34 results in:

$$\nabla^2 \hat{p}_s + \frac{\omega^2}{c_a^2} \hat{p}_s = 0 \tag{4.39}$$

Introducing the wave number (k_n) to Eq. 4.39 yields:

$$\nabla^2 \hat{p}_s + k_n^2 \hat{p}_s = 0, \tag{4.40}$$

which is the Helmholtz equation for the complex pressure amplitude.

The general solution for these equations can be in the form of:

$$p_s = Ae^{-ik_n r_s} \tag{4.41}$$

or

$$p_s = Ae^{-i\frac{\omega}{c_a} r_s} \tag{4.42}$$

Accordingly the particle velocity equation can be written as:

$$v_s = Be^{-ik_n r_s} \tag{4.43}$$

or

$$v_s = Be^{-i\frac{\omega}{c_a} r_s}, \tag{4.44}$$

where (A and B) are constants, (ω) is the angular frequency, (r_s) is the radius or distance from sound source, and (k_n) is the wave number.

4.2.5 Types of Sound Field

Free field

The free field is a region in space where sound may propagate free from any form of obstruction. In practice, it is a field in which reflections at the boundaries are negligible over the frequency range of interest [Iso3744].

Near field

The near field of a source is the region close to the source where the sound pressure and acoustic particle velocity are not in phase. The near field is limited to a distance from the source equal to about a wavelength of sound or equal to three times the largest dimension of the sound source (whichever is the larger). The near field condition for spherical sound source can be estimated by:

$$r_s < \lambda_s / 2\pi \text{ or } k_n r_s < 1 \tag{4.45}$$

Far field

The far field of a source begins where the near field ends and extends to infinity. Note that the transition from near to far field is gradual in the transition region. In the far field, the direct field radiated by most machinery sources will decay at the rate of 6 dB or 3 dB each time the distance from the source is doubled, depending on the type of wave front. The far field condition for spherical sound source can be determined by:

$$r_s > \lambda_s / 2\pi \text{ or } k_n r_s > 1 \tag{4.46}$$

Direct field

The direct field of a sound source is defined as that part of the sound field which has not suffered any reflection from any room surfaces or obstacles.

Reverberant field

The reverberant field of a source is defined as that part of the sound field radiated by a source which has experienced at least one reflection from a boundary of the room or enclosure containing the source.

4.2.6 Waveforms

It is essential not to confuse waveform with wave type. The wave type - as shown before - describes how the wave propagates in solids, fluids and in the air. However, the waveform is an imaginary surface joining all points in space that are reached at the same instant by a wave propagating through a medium [Ans2010]. It can be clearly observed by dropping a stone in water, as a consequence, some ripples propagate on the water surface in circular forms. The wave front is then represented by this circle which is the collection of all points whose particles are in same phase of oscillation. It is always perpendicular to propagation of the wave [Roy2010].

The geometrical form of the wave fronts is generally complicated. The most common wave fronts are:

Plane radiator (plane waves)

The plane waves are a special case of the airborne sound waves. They have uniform (constant) properties (pressure, velocity, etc.) in a plane perpendicular to their direction of propagation. A uniform plane wave propagating in the *x* direction is shown in Fig. 4-5. At each level, which is perpendicular to the coordinate direction *x*, all acoustic variables are constant.

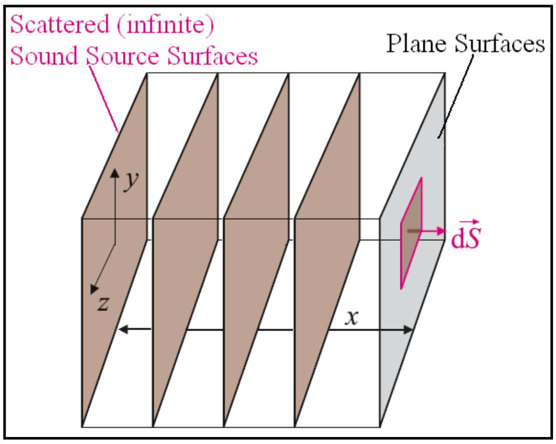

Figure 4-5: Plane waveform [Kur2008]

The mathematical representation of a plane wave is such that all acoustic field quantities vary with time and with one Cartesian coordinate. That coordinate is taken here as x; consequently, all the acoustic quantities are independent of y and z. Consequently, Eq. 4.34 can be written as:

$$\frac{\partial^2 p_s}{\partial x^2} - \frac{1}{c_a^2}\frac{\partial^2 p_s}{\partial t^2} = 0 \tag{4.47}$$

or

$$\left(\frac{\partial}{\partial x} - \frac{1}{c_a}\frac{\partial}{\partial t}\right)\left(\frac{\partial}{\partial x} + \frac{1}{c_a}\frac{\partial}{\partial t}\right)p_s = 0\,. \tag{4.48}$$

The solution of this equation is a sum of two expressions and can be represented by:

$$p_s(x,t) = f(x - c_a t) + g(x + c_a t)\,, \tag{4.49}$$

where (f and g) are two arbitrary functions. The argument combination ($x-c_a t$) of the first term is such that the function (f) with that argument represents a plane wave travelling forward in the (+) x-direction at a velocity (c_a). The argument combination ($x-c_a t$) of the second term is such that the function g similarly represents a plane wave travelling backwards in the (−) x-direction, also at a velocity (c_a) [Ros2007]. For a plane wave travelling along the (+) x-axis at a velocity (c_a) and with a constant-frequency acoustic pressure disturbance, Eq. 4.49 can be represented by the expression:

$$\hat{p}_s = |p_s|\cos[k(x - c_a t) + \phi_0] = \mathrm{Re}(p_s e^{ik(x-c_a t)})\,, \tag{4.50}$$

with the angular frequency $\omega = k_n c_a$.

The particle velocity that corresponds to the plane wave solution can then be deduced from Eq. 4.38:

$$
\begin{aligned}
i\omega\rho\hat{v}_s &= \frac{\partial \hat{p}_s}{\partial t} = ikp_s(e^{ik(x-c_at)}) \\
\hat{v}_s &= \frac{1}{\rho c_a}\mathrm{Re}\left(p_s(e^{ik(x-c_at)})\right)
\end{aligned}
\tag{4.51}
$$

The radiation impedance for the plane wave can be deduced from Eq. 4.50 and Eq. 4.51:

$$
Z_{rad} = \frac{\hat{p}_s}{\hat{v}_s} = \rho c_a \tag{4.52}
$$

Spherical sound source (breathing sphere)

It is a sound wave where all parameters only depend on the distance from the origin; it always spreads out radially from the sound sources or from scatters (see Fig. 4-6). This type of wave, where a sound source emits a spherical wave, is called a spherical source of 0th order.

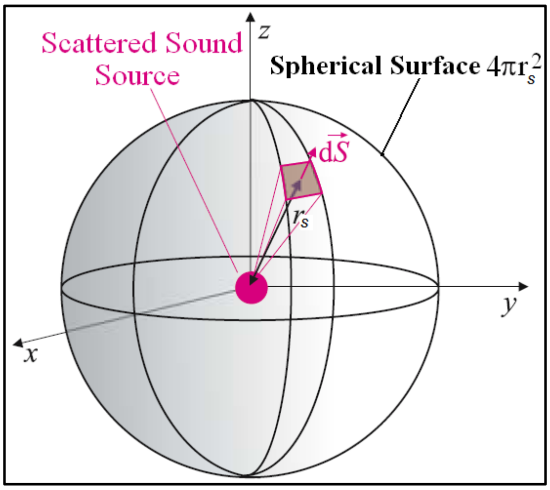

Figure 4-6: Spherical waveform [Kur2008]

To derive the appropriate wave equation, it is helpful to transform Eq. 4.40 from Cartesian coordinates, x, y, z, into spherical coordinates, r_s, φ, ϑ . In that case, Eq. 4.40 can be represented as follows:

$$
\frac{1}{r_s^2}\frac{\partial}{\partial r_s}\left(r_s^2\frac{\partial \hat{p}_s}{\partial r_s}\right) + \frac{1}{r_s^2 \sin\vartheta}\frac{\partial}{\partial \vartheta}\left(\sin\vartheta\frac{\partial \hat{p}_s}{\partial \vartheta}\right) + \frac{1}{r_s^2\sin^2\vartheta}\frac{\partial^2 \hat{p}_s}{\partial \varphi^2} + k_{n0}^2\hat{p}_s = 0 . \tag{4.53}
$$

According to Eq. 4.38, the radial velocity component can be introduced by:

$$
\hat{v}_s = -\frac{1}{i\omega\rho}\frac{\partial \hat{p}_s}{\partial r_s} . \tag{4.54}
$$

For the radiation of spherical sound source, the field quantities depend only on the radius (r_s); consequently the differential terms, which depend on (φ) and (ϑ) in Eq. 4.53, vanish and the spatial pressure takes the form:

$$p_s = \frac{C}{r_s} e^{-ik_n r_s} \ . \tag{4.55}$$

Using Eq. 4.55, the radial velocity component can be expressed as follows:

$$v_s = -\frac{C}{i\omega\rho}\left(-\frac{1}{r_s^2} - \frac{ik_n}{r_s}\right) e^{-ik_n r_s} \tag{4.56}$$

or

$$v_s = C\left(\frac{1}{c_a \rho r_s} + \frac{1}{i\omega\rho r_s^2}\right) e^{-ik_n r_s} \ . \tag{4.57}$$

The constant (C) can be determined from the boundary condition at (r_s = a), where (a) is the radius of the spherical sound source:

$$v_a = -\frac{C}{i\omega\rho}\left(-\frac{1}{a^2} - \frac{ik_n}{a}\right) e^{-ik_n a} \tag{4.58}$$

Also:

$$C = \frac{i\omega\rho a^2}{1 + ik_n a} v_a e^{-ik_n a} \tag{4.59}$$

Replacing (C) in Eq. 4.55 and Eq. 4.56, the sound pressure and the radial velocity component can be developed as:

$$p_s = v_a \frac{i\omega\rho a^2}{1 + ik_n a} \frac{e^{-ik_n(r_s - a)}}{r_s} \tag{4.60}$$

$$v_s = v_a \frac{a^2}{1 + ik_n a} \frac{1 + ik_n r_s}{r_s^2} e^{-ik_n(r_s - a)} \ . \tag{4.61}$$

The specific radiation impedance can then be calculated at the outer surface of the sound source where (r_s = a) using Eq. 4.55 and Eq. 4.57:

$$Z_{rad} = \frac{\hat{p}_s}{\hat{v}_s} = \frac{\frac{C}{a}}{C\left(\frac{1}{\rho c_a a} + \frac{1}{i\omega\rho a^2}\right)} = \frac{1}{\left(\frac{1}{\rho c_a} + \frac{1}{i\omega\rho a}\right)} = \frac{1}{\frac{1}{\rho c_a}\left(1 + \frac{1}{ik_n a}\right)} = \rho c_a \frac{ik_n a}{1 + ik_n a} \ . \tag{4.62}$$

From the same equations, the radiated power can be deduced as follows:

$$W = \frac{1}{2}\mathrm{Re}\left[\int_S p_s v_s dS\right] = 2\pi a^2 |v_a|^2 \rho c_a \frac{(k_n a)^2}{1+(k_n a)^2}. \tag{4.63}$$

Referring to Eq. 4.63, the radiation efficiency can be deduced:

$$\sigma_{r(a)} = \frac{W}{\rho c_a S |v_a|^2 / 2} = \frac{2\pi a^2 |v_a|^2 \rho c_a \frac{(k_n a)^2}{1+(k_n a)^2}}{\rho c_a S |v_a|^2 / 2} = \frac{(k_n a)^2}{1+(k_n a)^2}, \tag{4.64}$$

where (*S*) is the spherical surface induced by$4\pi r_s^2$.

For the 1st order spherical sound source (dipole radiators) as well as for the nth order, the solutions of the wave equation are described in [Bla2008] and [Cre2005].

The spherical waveform in a far propagation can be treated as a plane wave because the term $k_n a$ increases strongly and makes the spherical equations similar to those of the plane wave (see Fig. 4-7).

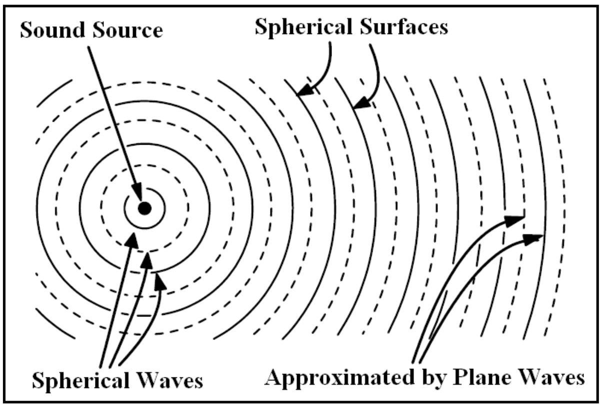

Figure 4-7: Far propagation of spherical waves [Kar2007]

Cylindrical sound source

From dense traffic roads, railway trains, band-conveyor, vibrating pipes, tubes and ducts, the radiation consists of multiple scattered point sources along an imaginary line which represents the axis of a cylindrical surface with length (*l*) (see Fig. 4-8). In this case, it is helpful to know the radiation characteristics of the cylindrical sound source (cylindrical radiator).

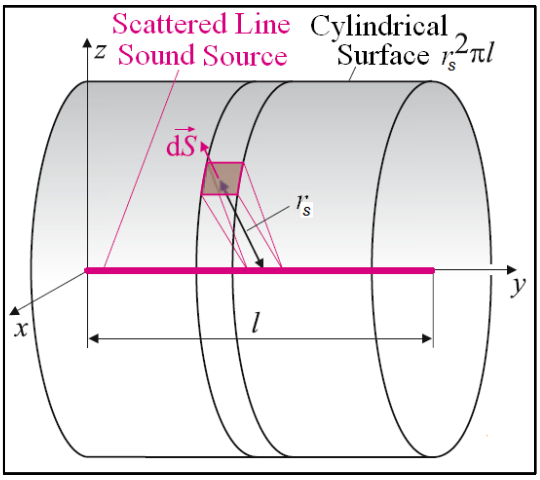

Figure 4-8: Cylindrical waveform [Kur2008]

Consider an infinitely long cylinder with a nominal radius (r_s). The cylinder vibrates at an angular frequency (ω); the circumferential velocity distribution is:

$$v_s(\varphi) = v_n \cos(r\varphi)\,, \tag{4.65}$$

where (r) is the mode index.

Eq. 4.40 can be written, in cylindrical coordination, as follows:

$$\frac{1}{r_s}\frac{\partial}{\partial r_s}\left(r_s \frac{\partial \hat{p}_s}{\partial r_s}\right) + \frac{1}{r_s^2}\frac{\partial^2 \hat{p}_s}{\partial \varphi^2} + k_{n0}^2 \hat{p}_s = 0\,, \tag{4.66}$$

which yields a dependence in the form:

$$p_s \rightarrow \frac{1}{\sqrt{r_s}} e^{-jk_{n0}r_s}\,;\ r_s \rightarrow \infty\,,$$

at large distances, and hence describes outwardly propagating cylindrical waves [Cre2005].

Using this condition, Eq. 4.38 can be represented by:

$$i\omega\rho \hat{v}_s(\varphi) = \left.\frac{\partial \hat{p}_s}{\partial r_s}\right|_{r_s=a} \tag{4.67}$$

Equations 4.65, 4.66 and 4.67 are fulfilled by:

$$\hat{p}_s(r_s,\varphi) = -v_n \frac{j\rho c_a}{H_n^{(2)'}(k_{n0}a)} \cos(r\varphi) H_n^{(2)}(k_{n0}a)\,, \tag{4.68}$$

$$\hat{v}_s(r_s,\varphi) = -v_n \frac{\cos(r\varphi)}{H_n^{(2)\prime}(k_{n0}a)} H_n^{(2)\prime}(k_{n0}a) \cdot \tag{4.69}$$

Herein, ($H_n^{(2)}$) is the Hankel function of the second kind and of the nth order, and ($H_n^{(2)\prime}$) is the first derivative with respect to ($k_{n0}r_s$).

According to [Cre2005] and [Abr1972], the two limiting forms of the Hankel function are:

$$\begin{aligned} H_n^{(2)}(k_{n0}r_s) &\approx \left\{ \begin{matrix} 1 - j\dfrac{2}{\pi}\ln\left(\dfrac{\gamma k_{n0}r_s}{2}\right); n = 0 \\ \left(\dfrac{k_{n0}r_s}{2}\right)^2 + j\dfrac{(n-1)!}{\pi}\left(\dfrac{2}{k_{n0}r_s}\right)^{2n}; n \geq 1 \end{matrix} \right\}; k_{n0}r_s << n+1, \\ H_n^{(2)}(k_{n0}r_s) &\approx \sqrt{\frac{2}{\pi k_{n0}r_s}} e^{j\frac{\pi}{2}\left(n+\frac{1}{2}\right)} e^{-jk_{n0}r_s}; k_{n0}r_s >> n+1, \end{aligned} \tag{4.70}$$

where Euler's constant is $\gamma = 1.781$.

The radiation impedance can then be deduced by:

$$Z_{n,rad} = \frac{\hat{p}_s}{\hat{v}_s} = j\rho c_a \frac{H_n^{(2)}(k_{n0}r_s)}{H_n^{(2)\prime}(k_{n0}r_s)} \ . \tag{4.71}$$

The radially oscillating cylinder with the zero order (n=0) is a classic example for verifying these equations:

$$Z_{0,rad} \approx j\rho c_a \frac{1 - j\dfrac{2}{\pi}\ln\left(\dfrac{\gamma k_{n0}r_s}{2}\right)}{H_n^{(2)\prime}(k_{n0}a)} \ . \tag{4.72}$$

The radiated efficiency can also be defined as [Cre2005]:

$$\sigma_n = \frac{2}{\pi}\frac{\omega}{c_a}\frac{1}{\left|H_n^{(2)\prime}(k_{n0}a)\right|^2}\frac{1}{k_{n0}^2 a} \ . \tag{4.73}$$

4.3 Structure-Borne Sound Results

As mentioned in Chapter 2, the magnetic forces first excite the stator structure, and then deduced Eigen frequencies (f) and mechanical deformations (y) are employed in the calculation of the particle velocity (v_s) and the sound pressure (p_s) at the outer surface of the structure. Theoretically, the derivation of the mechanical deformation with respect to time gives the vibrational velocities on the structure, and after that the wave equation can be applied to compute the sound pressure. This is simply the way to explore the vibrational behavior of a structure, and it is illustrated in Fig. 4-9.

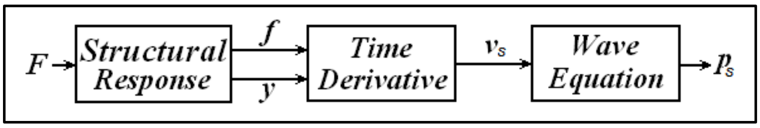

Figure 4-9: Stages and variables used in the structural-borne process

The simulation of the structure-borne sound is performed using the **B**oundary **E**lement **M**ethod (BEM). The BEM has been developed in order to reduce the element matrices of large problems and to solve them numerically in a short-time compared with the traditional **F**inite **E**lement **M**ethod (FEM). It is normally used in acoustic simulations, where the computations have to be performed on large spaces like machines and their surroundings, ducts, and rooms, which could be filled by air or fluids. For this purpose, the acoustic software “WAON” is used with its implemented BEM techniques. These techniques are moreover developed by applying the Fast Multipole algorithm to the BEM, which, in addition, permits us to decrease the calculation time of the simulation and also to reduce the required memory [Wao2010]. This Fast Multipole Boundary Element Method (FMBEM) preserves the same accuracy of the conventional BEM. The simulation time obviously depends on the frequency, the element number, and the shape irregularities of the geometrical model.

4.3.1 Interfacing Process “Mesh Mapping”

The interfacing process between the harmonic analysis and the acoustic simulation can be performed by mapping a 3D surface mesh from the 3D model and by transferring the nodes and elements results of the 3D model to the acoustic simulation field. This 3D surface mesh has to be imported into the acoustic simulation space in order to subject the nodes and elements by the corresponding deformations and particle velocities resulting from the harmonic analysis.

Meshing the 3D solid model of ANSYS by a shell element converts it to a 3D surface model called the Boundary Element Model. This action represents the first step in the interfacing process between ANSYS and WAON. This BE model has to be checked with awareness, in order to eliminate any superimposed elements existing between the interfacing surfaces of the different parts of the model. The existence of these superimposed elements dramatically increases the simulation time and introduces unnecessary computations into the model. Another important point is the size of the element. It plays a significant role in defining the maximal reachable frequency that could be considered for the acoustic computations. In WAON, the rule is based on taking at least six elements per acoustic wavelength.

The second step is to specify for WAON the “.res” file of the harmonic analysis performed by ANSYS (see Fig. 4-10). This file contains the results of the structural response that are needed for the acoustic computation. Actually, it contains the element matrix and the corresponding deformation values.

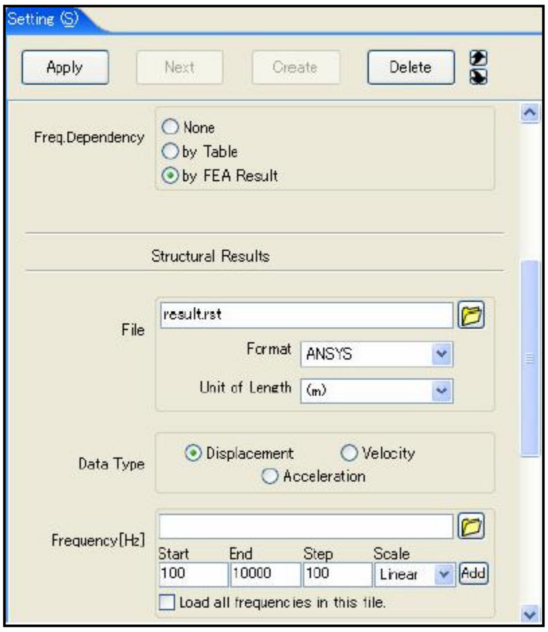

Freq.Dependency ○ None ○ by Table ● by FEA Result

File: result.rst
Format: ANSYS
Unit of Length: (m)

Data Type ● Displacement ○ Velocity ○ Acceleration

Frequency[Hz]
Start: 100 End: 10000 Step: 100 Scale: Linear Add
☐ Load all frequencies in this file.

Figure 4-10: WAON Menu for reading the structural results of ANSYS

Afterwards, the configuration of parameters in WAON has to be carefully selected to visualize the right boundary conditions, in order to represent the reality as accurately as possible; more details, concerning the configuration of BEM-simulation in WAON are discussed in [Alr2010].

To compute the particle velocities and sound pressures on the external surface of the stator system, the simulations are performed for every mode separately and the results are shown in Fig. 4-11 to Fig. 4-15.

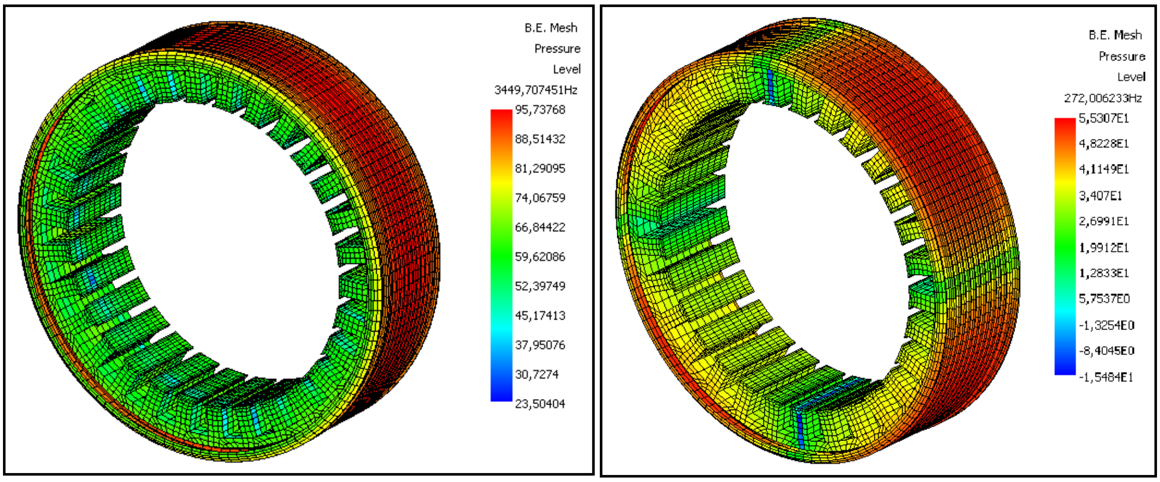

Figure 4-11: Structure-borne sound results of mode (0) and (2), respectively

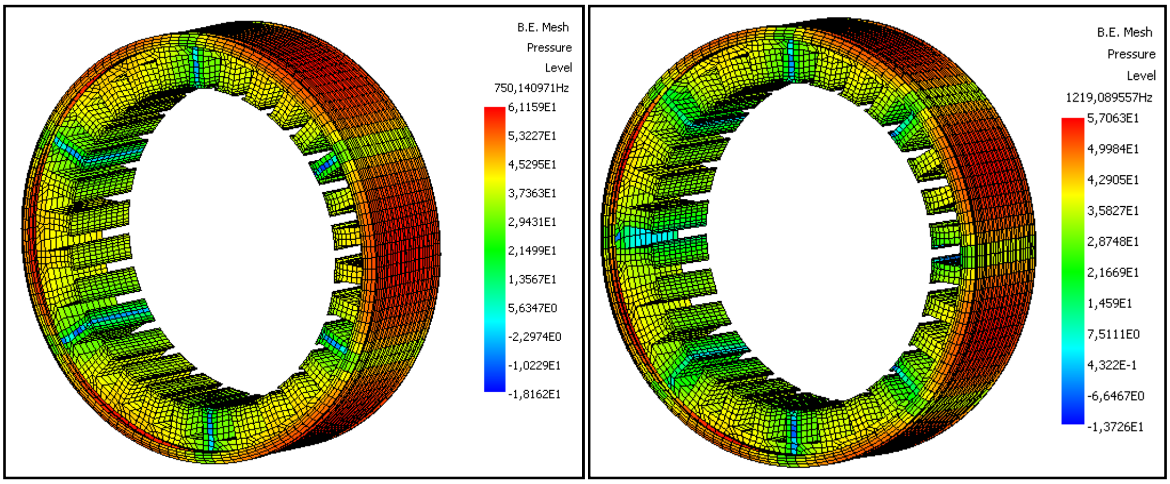

Figure 4-12: Structure-borne sound results of mode (3) and (4), respectively

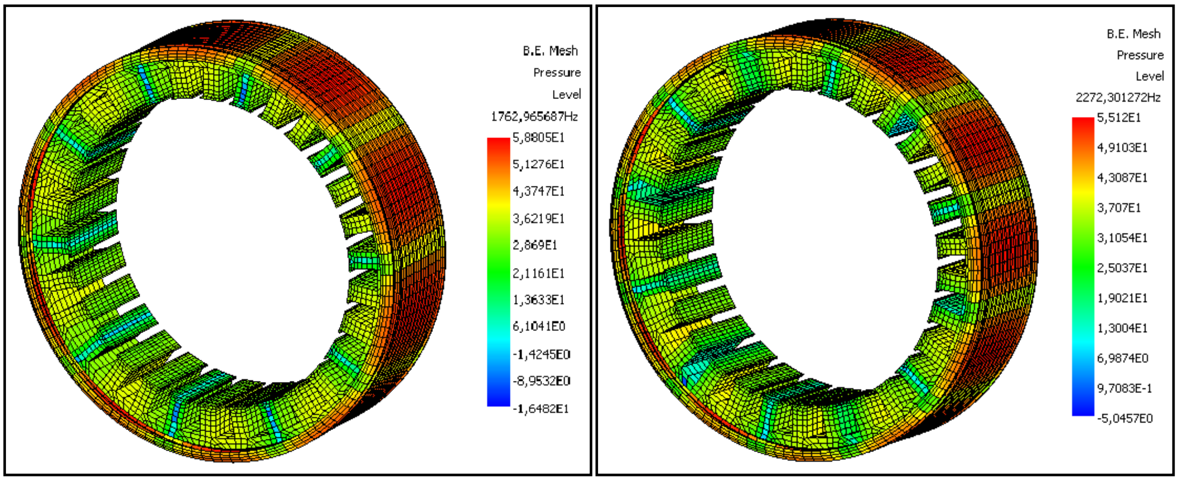

Figure 4-13: Structure-borne sound results of mode (5) and (6), respectively

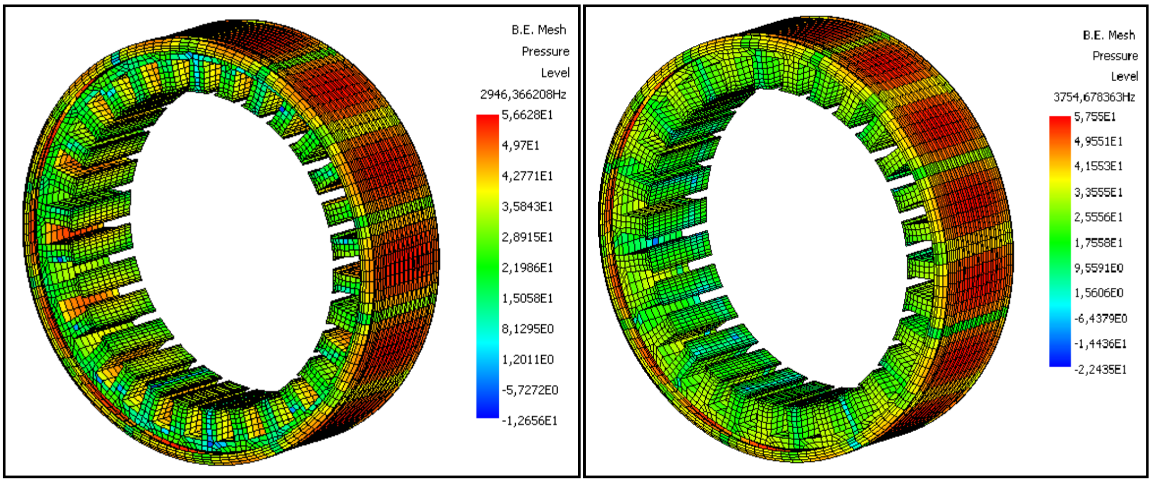

Figure 4-14: Structure-borne sound results of mode (7) and (8), respectively

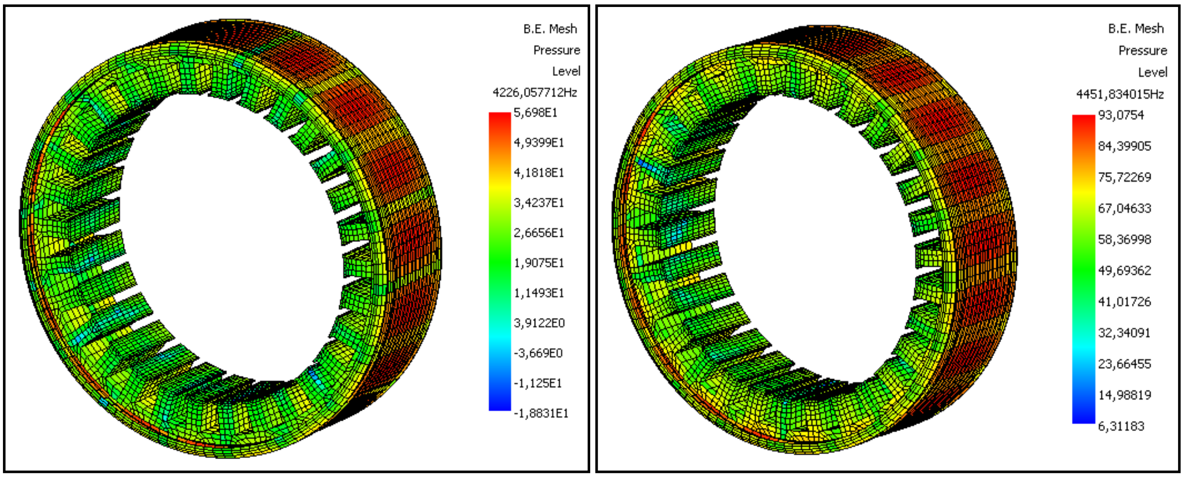

Figure 4-15: Structure-borne sound results of mode (9) and (10), respectively

In Fig. 4-16, the decibel levels of the ten modes are plotted against their Eigen frequencies; the purpose is to display the dominant modes with respect to their frequency domains.

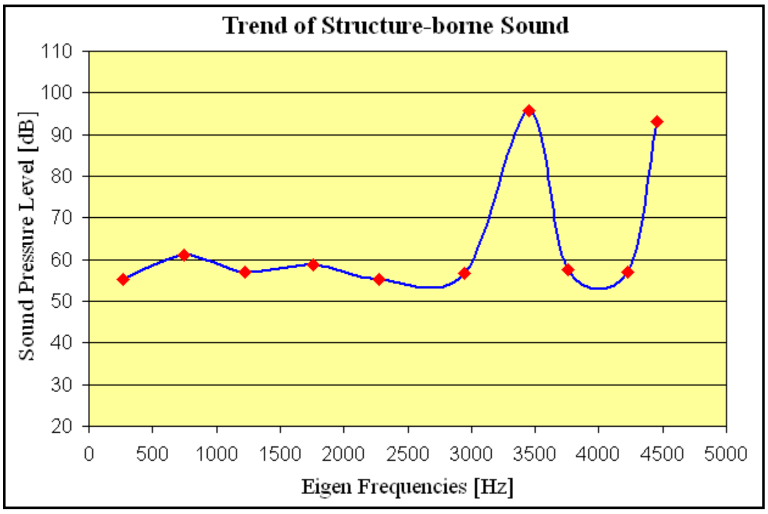

Figure 4-16: Plot of the structure-borne sound for the first 10 modes

4.4 Air-Borne Sound Results

The vibrational velocity on the external surfaces attacks the air particles in the surroundings and lets them vibrate. In this case, the particle velocity is approximately equal to the vibrational velocity of the structure. The corresponding sound pressure (p_1) can be accordingly computed by applying the wave equation. The sound propagation theory has to be used presently to compute the sound pressure (p_2) (see Fig. 4-17). In fact, the calculation of (p_2) depends on the waveform, the distance from the source and the operating frequency.

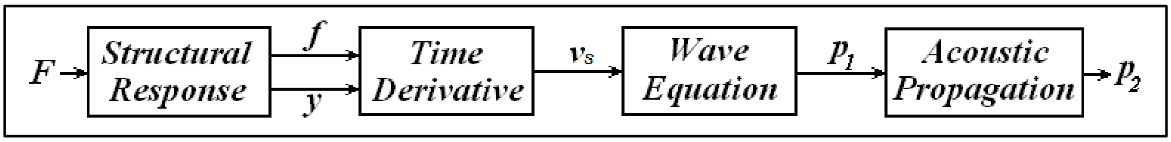

Figure 4-17: Parameterization of the air-borne process

The stator frame symbolizes the sound source of noise to the external surroundings. Consequently, the elements of the stator frame represent the sound sources for the BEM simulation. In order to check this statement and to investigate the effect of stator core surfaces (stator teeth surfaces) on the radiated acoustic energy, simulations with different configurations are performed in WAON. Some of them are done by selecting all elements of the stator system (including the stator teeth elements) and the others are done by selecting only the frame elements.

Maximal levels of BEM simulations in [dB]		
Mode number	All elements	Frame elements
0	132	127
2	74	73
3	92	91
4	106	101
5	108	108

Table 4-1: Simulations results with "All elements" and "Frame elements"

The result in Table 4-1 shows that a maximum deviation of 5[dB] can sometimes occur. However, the calculation time needed "with all elements" is up to six times longer than the time needed when calculating with "frame elements" only. More options for WAON-configuration are tested and analyzed in [Alr2010].

The air-borne computations are actually achieved on a spherical surface with a radius of 0.5m and this spherical lattice is defined in WAON by the Field Point Mesh (FPM). The radius has been selected in such a way that a far field range can be realized for all modes (see Tab. 4-2). According to Eq. 4.46, the required condition for achieving a far field range is:

$$\frac{2\pi r_s}{\lambda_s} > 1 \ .$$

Mode Number	λ_s[m]	$2\pi r_s / \lambda_s$
0	0.10	31.6
2	1.26	2.5
3	0.46	6.9
4	0.28	11.2
5	0.19	16.1
6	0.15	20.8
7	0.12	27.0
8	0.09	34.4
9	0.08	38.7
10	0.08	40.7

Table 4-2: Achieving a far field range for all modes using a FPM-radius of 0.5m

The air-borne results in WAON for every mode are presented in Fig. 4-18 to Fig. 4-22.

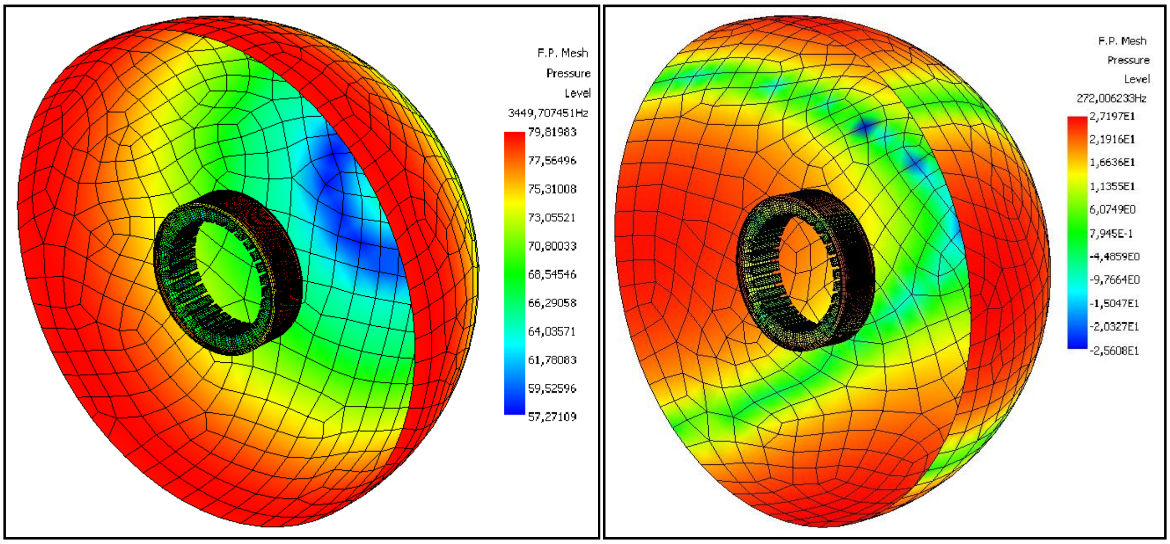

Figure 4-18: Air-borne computation in [dB] for mode 0 and 2, respectively

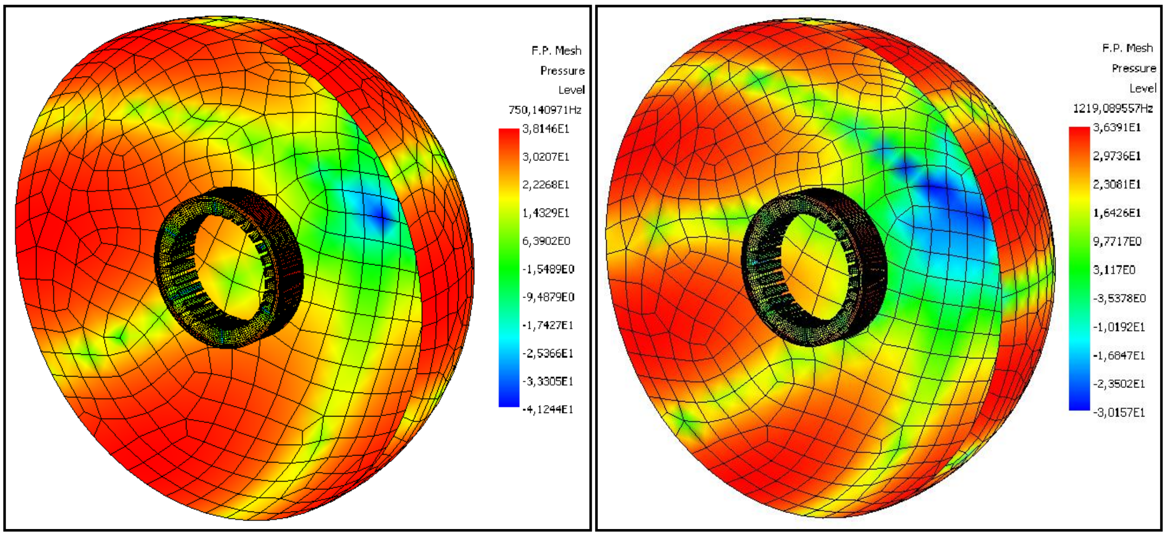

Figure 4-19: Air-borne computation in [dB] for mode 3 and 4, respectively

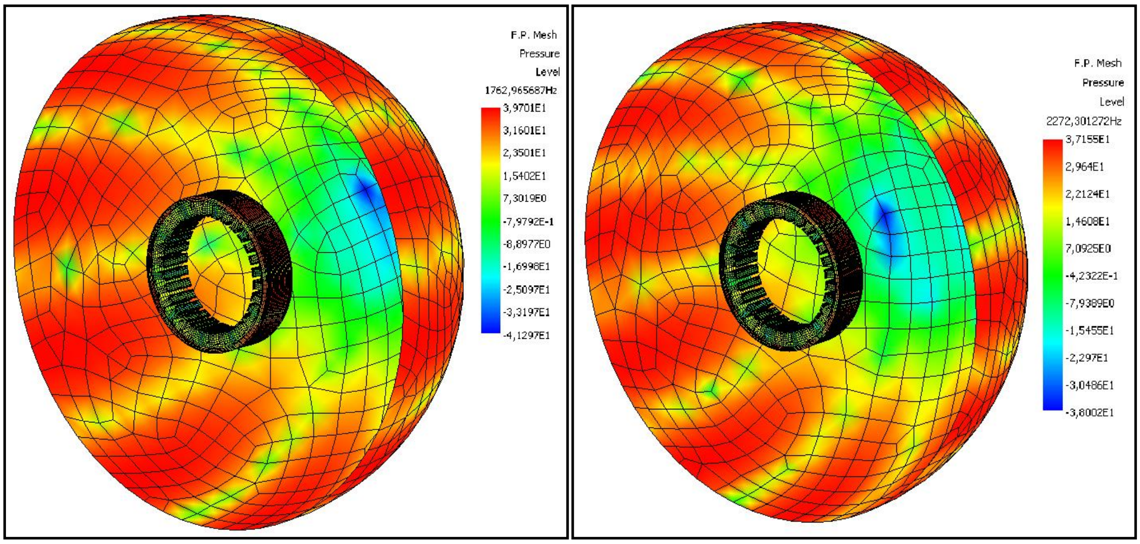

Figure 4-20: Air-borne computation in [dB] for mode 5 and 6, respectively

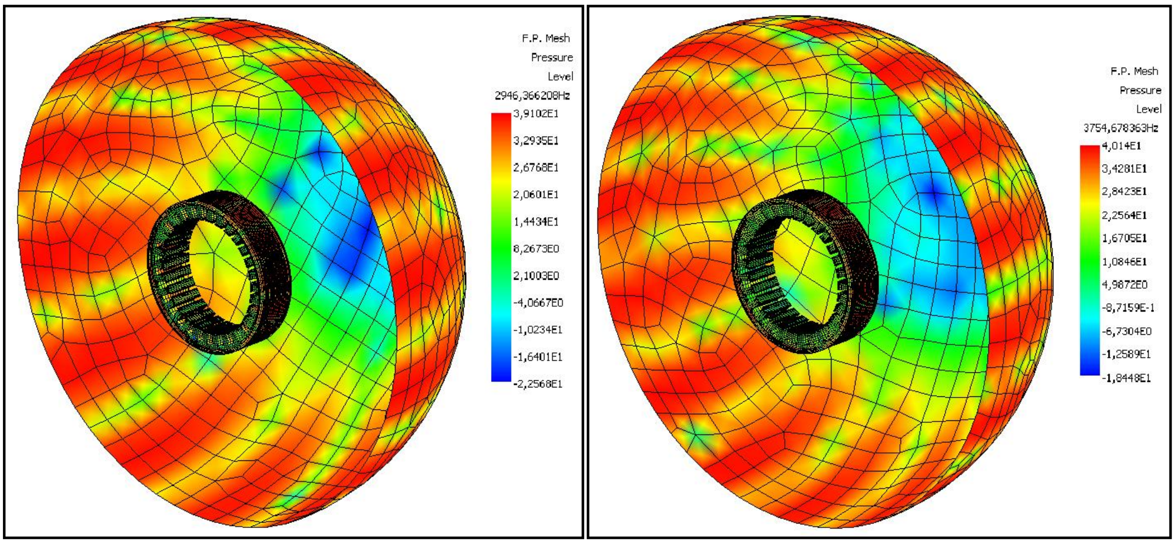

Figure 4-21: Air-borne computation in [dB] for mode 7 and 8, respectively

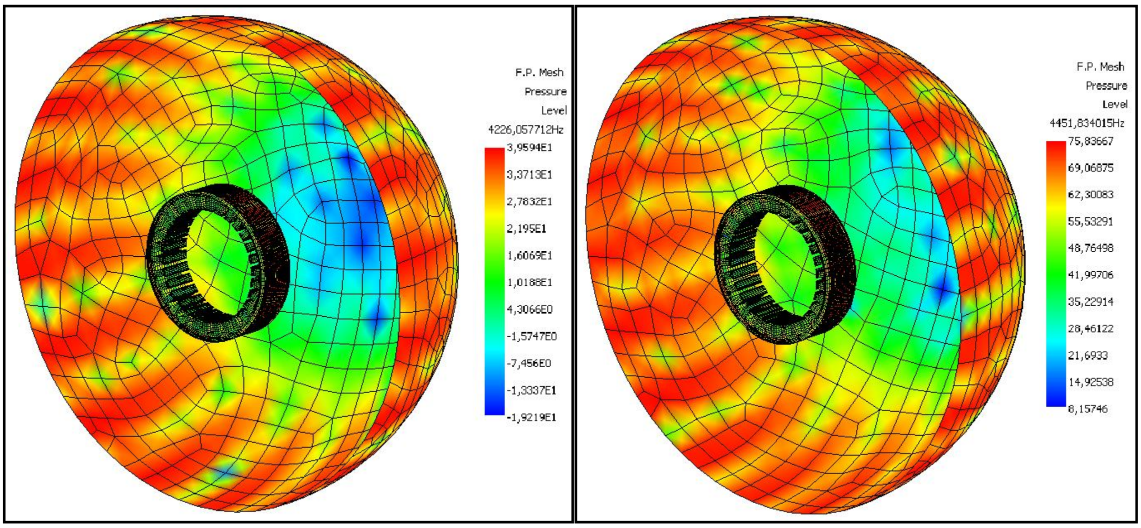

Figure 4-22: Air-borne computation in [dB] for mode 9 and 10, respectively

4.5 Interpretation

The results show that mode 0 and 10 are the dominant modes with air-borne sound levels of 80 and 76 [dB], respectively. Of course, these two modes have high frequencies (see Fig. 4-23). This result is already expected and inspected in Chapter 2, where the electromagnetic design of this electric machine is analyzed thoroughly.

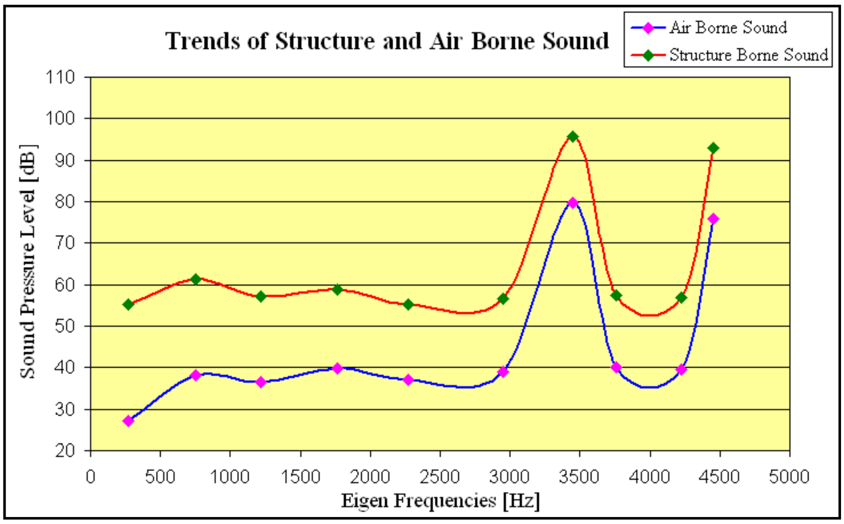

Figure 4-23: Sound pressure levels with respect to frequency

The difference in levels between the structure and air-borne results is located in an average range of 19 [dB] as shown in Tab. 4-3. These results are useful in the analytical modeling of the acoustical behavior for this electric machine. They can be also used with the **S**tatistical **E**nergy **A**nalysis (SEA), in order to find the transfer functions of the acoustic model.

Mode Number	Frequency [Hz]	Air-borne Level [dB]	Structure-borne Level [dB]	Difference [dB]
0	3450	80	96	16
2	272	27	55	28
3	750	38	61	23
4	1219	36	57	21
5	1763	40	59	19
6	2272	37	55	18
7	2946	39	57	18
8	3755	40	58	17
9	4226	40	57	17
10	4452	76	93	17

Table 4-3: Difference between structure-borne and air-borne results

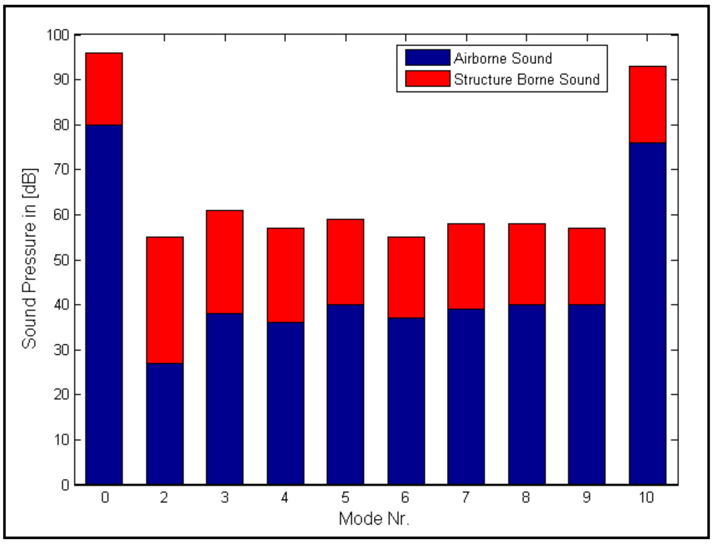

Figure 4-24: Structure and Air-Borne levels for the first 10 modes

Moreover, the simulation environment was chosen in such a way to be as realistic as possible. The purpose was to provide an exact simulation environment for the mounted stator system in the transmission housing. However, there is a point that could not be considered in the simulation and it is represented by the effect of the cooling fluid in the stator jacket, which can also have impact upon the damping factors of the stator system.

5 Electromagnetic Sensibility for Optimization

5.1 General Idea

In order to optimize the electromagnetic design of the IPM machine, two distinct methods have been processed; the first is the geometrical optimization of the lamination sheet design and the second is the skewing process. The optimization of the lamination sheet geometry is performed using FEM by investigating the critical geometrical parameters. For every parameter a definite range has been proposed, based on electromagnetic, mechanic and geometric considerations. In the first stage, each parameter is analyzed separately by keeping all other parameters constant. Then the optimal values of all parameters are combined in order to evaluate their whole effect on the entire performance of the IPM machine. Finally, a skewing process was applied to the optimized geometry in order to reach a high performance level and to improve the acoustic behavior of the machine.

5.2 Geometrical Optimization

The design optimization of an electric motor is a systematic method, performed with the goal of finding a set of scales for the geometrical parameters of the lamination sheet. These optimized parameters lead jointly to the best possible results that can be reached with the existing electric, magnetic and materials resources.

In the IPM optimization, it is better to use the numerical computation methods, in which the results can be much more realistic in comparison with the analytical calculations, which often need to be adjusted by introducing correction factors. Moreover, the FEM computations are essentially employed in exploring the field distribution and its harmonics, which are the most useful properties in the noise and vibration analysis. In this sense, an optimization process would be numerically realized, in order to ascertain an optimal shape of the lamination sheet and to find out the best combinations of all geometrical variables with their optimal values for a most favorable electromagnetic design.

In fact, the machine parameters usually have a non-linear impact on the performance of the machine, while, at the same time, they are highly coupled [Ouy2006]. Thus, in reality, an optimal design of the IPM machine structure is always a difficult task.

Therefore the optimization targets have been defined here as follow:

a) Low number of harmonics in the air gap

b) Reduction of the amplitude for the radial magnetic forces

c) Improvement of the noise and vibration behavior of the electric machine

d) Reduction of the torque ripple

e) Small volume of the magnets

As illustrated in Fig. 5-1, the stator and rotor geometries of such IPM Machines are basically optimized by a list of main parameters. These parameters and their limits are summarized in Tab. 5-1.

These parameters are carefully selected and can be optimized without changing the entire size of the machine. The yoke thickness has been analyzed, but it could not be regarded in this optimization. This is because in case its valve is reduced, the magnetic saturation in the stator yoke increases and affects the whole performance of the machine. However, raising its value brings about an increase in the outer radius of the stator and in the inner radius of the transmission housing, which is fully restricted.

Parameters	**Symbols**	**Range (mm)**
Lower tooth width	bz	[12.5 - 19.5]
Slot opening	bs	[11.4 - 4.4]
Pole shoe height	hs	[0.7 -1.3]
Bridge thickness	tb	[0.9 -1.2]
Magnet width	Wmag	[24- 28]

Table 5-1: Geometrical parameters and their limits

The slot opening “bs” is actually related to the lower tooth width. Both are computed from the arc length corresponding to one slot pitch angle at the inner radius of the stator. Consequently, these two parameters can be investigated in one step.

The bridge thickness “tb” also plays an important role in determining the leakage flux in the rotor. It has a considerable effect on the electromagnetic design as well as on the mechanical and dynamic rigidity of the rotor. Its range was selected by taking into consideration the reasonable thickness that can sustain the mechanical stress at high speed.

The magnet width “Wmag” and thickness (in magnetization direction) define the magnet volume in the motor. For small machines, the price of the magnet material can be half of the cost of the motor [Rus1991]. Therefore, this parameter has to be included in the geometrical optimization.

For decision-making, the radial magnetic forces, the torque and the torque pulsation for every parameter are separately represented in the first stage. Then, different simulations are performed by combining these parameters. It is necessary here to mention that all simulations and computations are done with a magnet characteristic of 120°C.

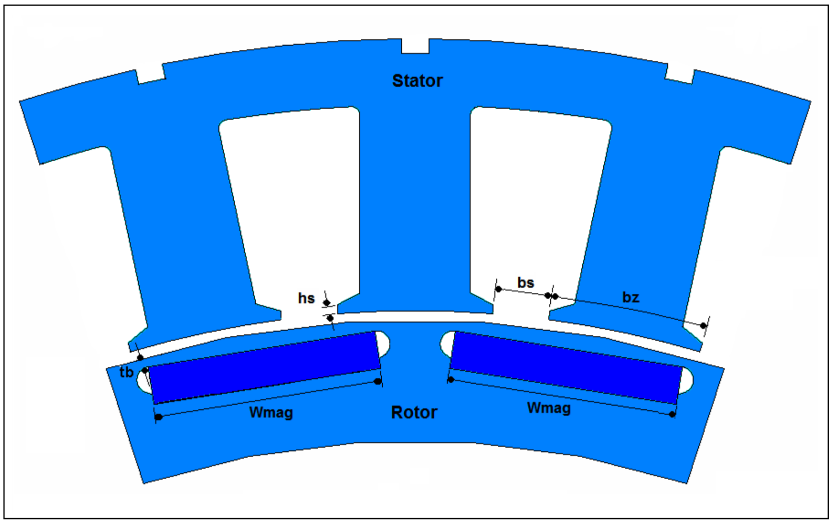

Figure 5-1:Parameters used in the geometrical optimization

5.2.1 Single Observation

Every parameter is inspected individually by keeping all other parameters constant.

Slot Opening

The slot opening “bs” and the lower tooth width “bz” are analyzed together in four different steps as shown in Table 5-2:

step	bz (mm)	bs (mm)
1	12.5	11.4
2	15.5	8.4
3	17.5	6.4
4	19.5	4.4

Table 5-2: The four proposed values of bz and bs for optimization

The maximum value of “bz” is 19.5mm, and the corresponding value of “bs” is 4.4mm. Theoretically, it is possible to make “bz” greater than 19.5mm, but, in this case, the path along the pole shoe becomes longer and thinner, enough to assure a high magnetic saturation in these regions. On the other hand, the teeth become straight forwarded with the value bz =12.5mm (bs =11.4mm) (see Fig. 5-2). This means that the coils, in this case, have to be clamped mechanically by creating tongues and grooves along the tooth sides and on the coil carrier bodies, respectively. This concept cannot be realized by applying the individual tooth concept, because each tooth has to be separately winded and the winded teeth have to be assembled later to form the stator core.

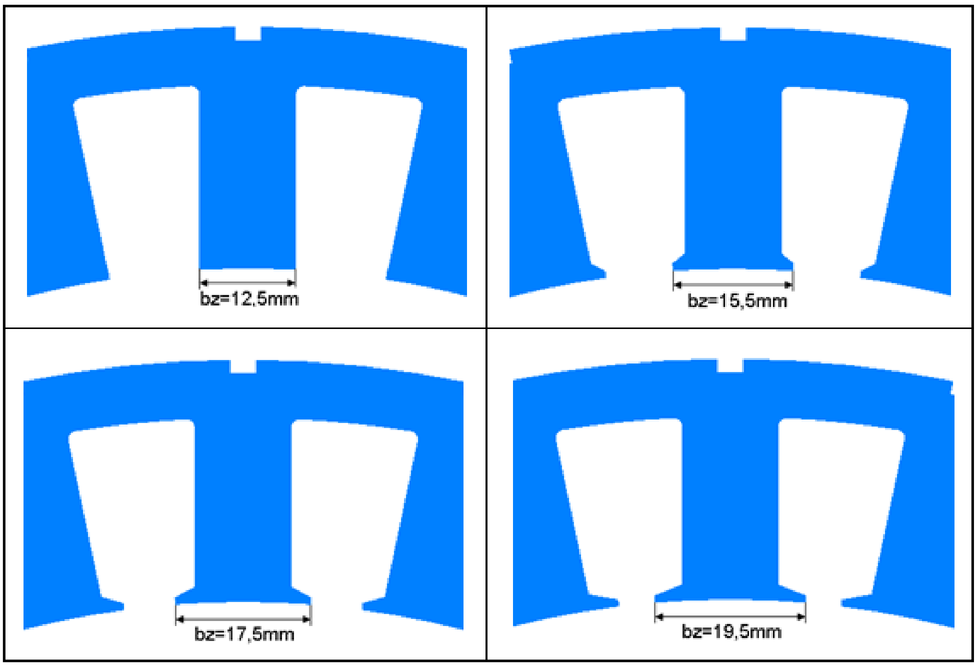

Figure 5-2: The tooth shapes corresponding to the four values of bz

The flux density curves of the four proposed values of “bz” differ from each other as shown in Fig. 5-3.

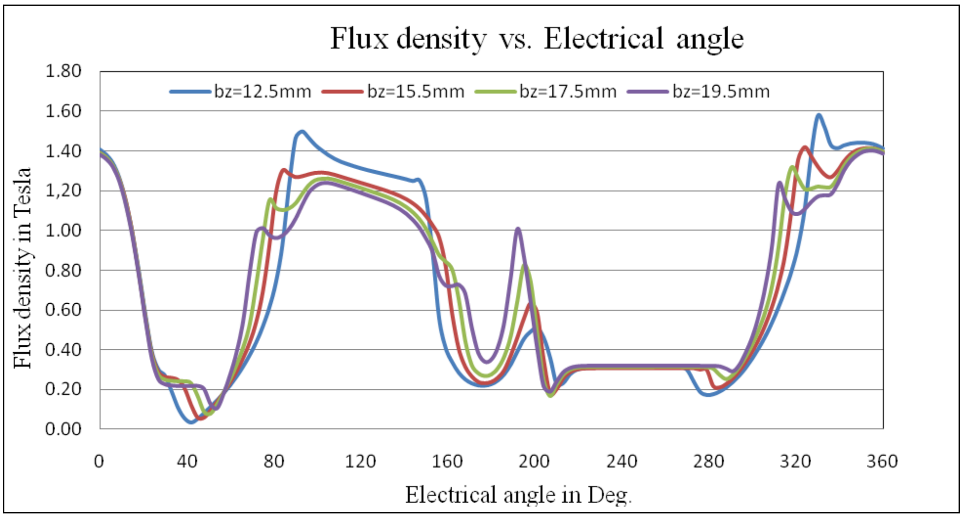

Figure 5-3: Flux density curves for the four values of “bz”

In order to evaluate the tangential forces, the torque curves along an electrical period are plotted in Figure 5-4. The torque mean values and the torque ripples, shown in Table 5-3, demonstrate that bz=12.5mm gives the minimal torque ripple, but this cannot be realized, as mentioned before. For the three remaining values, the bz =15.5mm brings about an improvement of 26% on the torque ripple, in comparison with the original value (bz=17.5mm) and 33% in comparison with the value bz=19.5mm. Based on this result, the bz=15.5mm can be considered a feasible solution to substitute the original value, but its effect on the radial force should be checked.

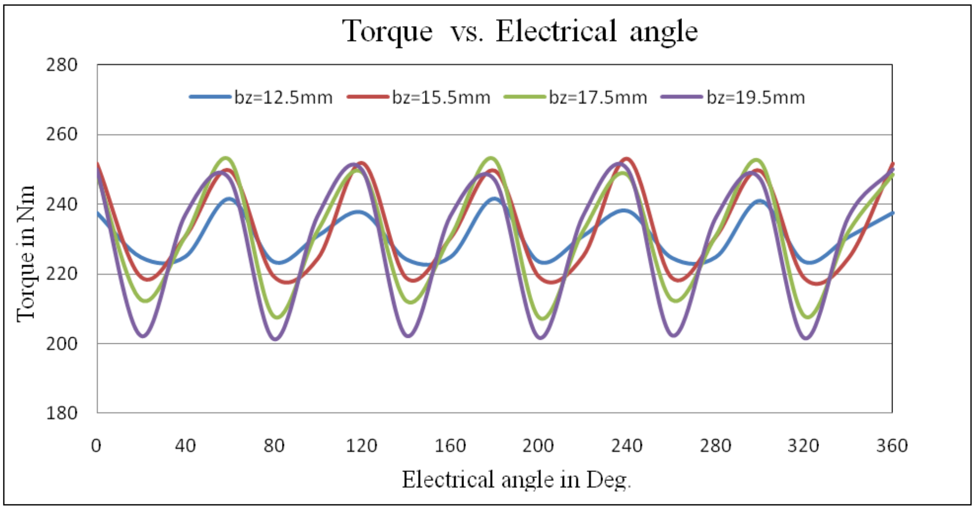

Figure 5-4: Torque curves of the four values of bz

bz (mm)	Torque mean value (Nm)	Torque ripple (Nm)
12.5	231	± 9
15.5	233	± 17
17.5	232	± 21
19.5	230	± 24

Table 5-3: Torques and torque ripples for the four values of bz

Concerning the radial forces, the interpretation is not only performed in spatial domain, but also in temporal domain (time). The representation in the spatial domain shows the distribution of the radial forces at spatial time (t), where the rotor is standing on a specific position (see Fig. 5-5). On the other hand, the temporal domain represents the variation of the radial forces with respect to the time covering a full electrical period. It is also described by the variation of radial forces with respect to the rotor position along an electrical period. In the temporal representation, the result of the original value of “bz” is compared with the alternative value bz=15.5 mm. The effect on the noise and vibration behavior of the machine is analyzed by observing the temporal results for every critical mode separately. Mode 0 and mode 10, as mentioned in Chapter 2, are identified as critical modes for this exemplary machine.

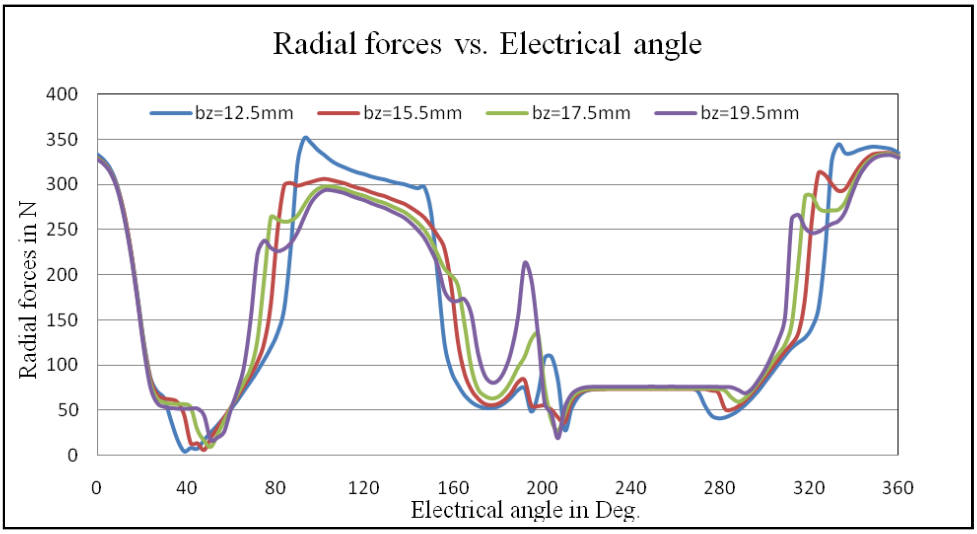

Figure 5-5: Spatial representation of radial forces for the four values of “bz”

In fact, the temporal representation relates the force components of each harmonic to the corresponding frequency orders. Therefore, the temporal illustration in Fig. 5-6 of the zero`s harmonic, which corresponds to mode zero (breathing mode), demonstrates an improvement of 5dB for the frequency order 60th, but the 30th order appears clearly. Concerning the mode 10, the temporal representation of the first harmonic exhibits also the 30th order with 5dB force in comparison with the original representation (see Fig. 5-7). As a result, the temporal representation for the breathing mode and mode 10 shows that the component amplitudes are almost equal to the original, up to the appearance of the 30th order.

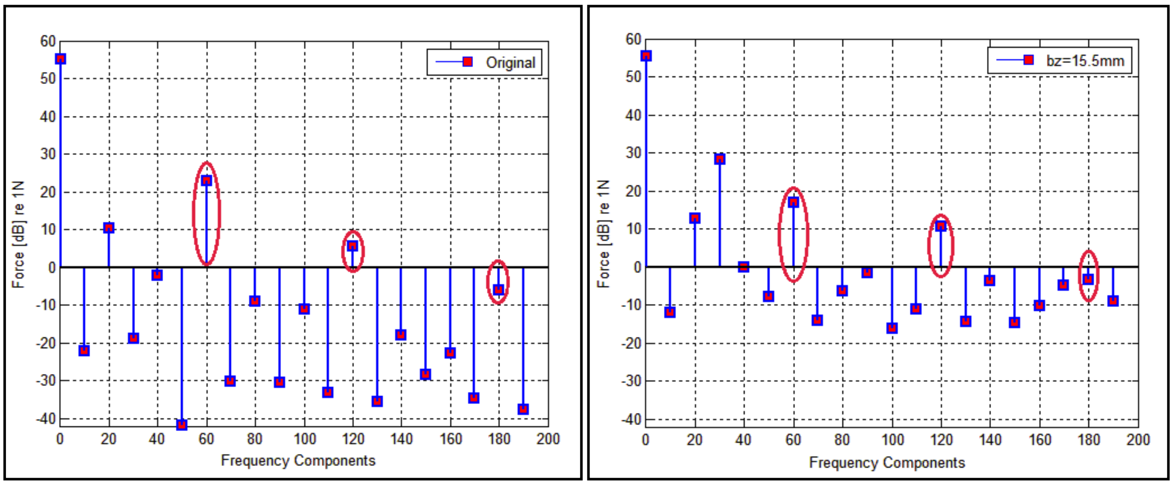

Figure 5-6: Temporal representations of mode zero in original design and with bz=15.5mm

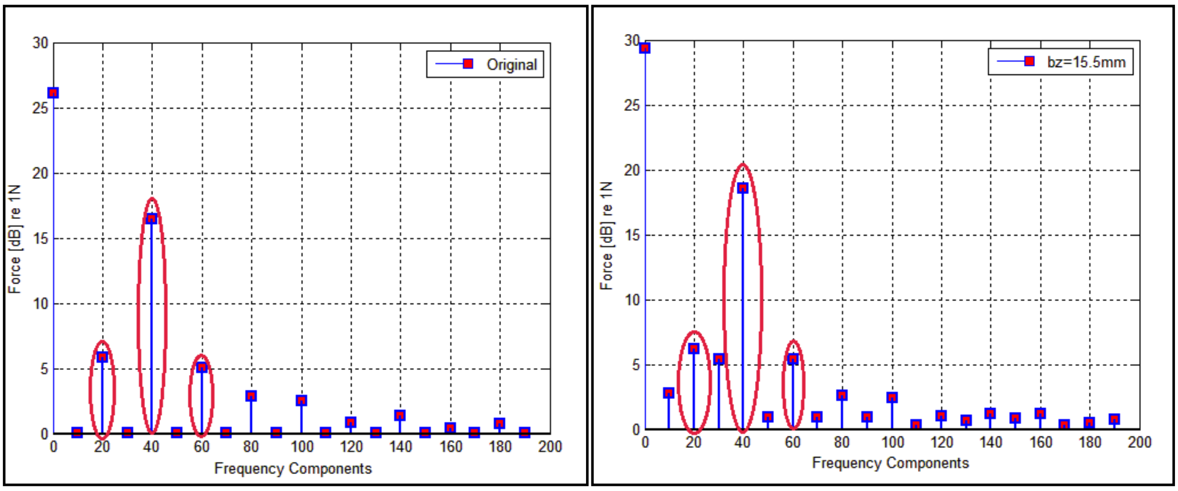

Figure 5-7: Temporal representations of mode 10 “sin” in original design and with bz=15.5mm

Pole shoe height

To analyze the effect of the pole shoe height, two values are proposed in addition to the actual value, one is smaller than the actual and the other is greater (see Tab.5-4). These three values are checked and studied by performing the FEM simulations.

Step	hz (mm)
1	0.7
2	1.0
3	1.3

Table 5-4: The different values of “hz”

The representations of the flux densities and the torques for the three values of “hz” are shown in Fig. 5-8 and Fig. 5-9; they are plotted versus one full electrical period.

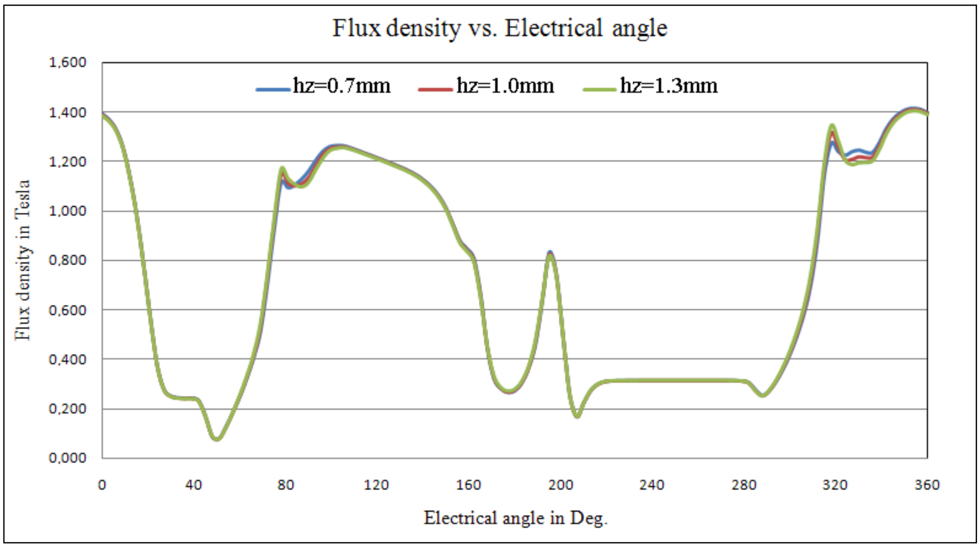

Figure 5-8: Flux density curves for the three values of “hz”

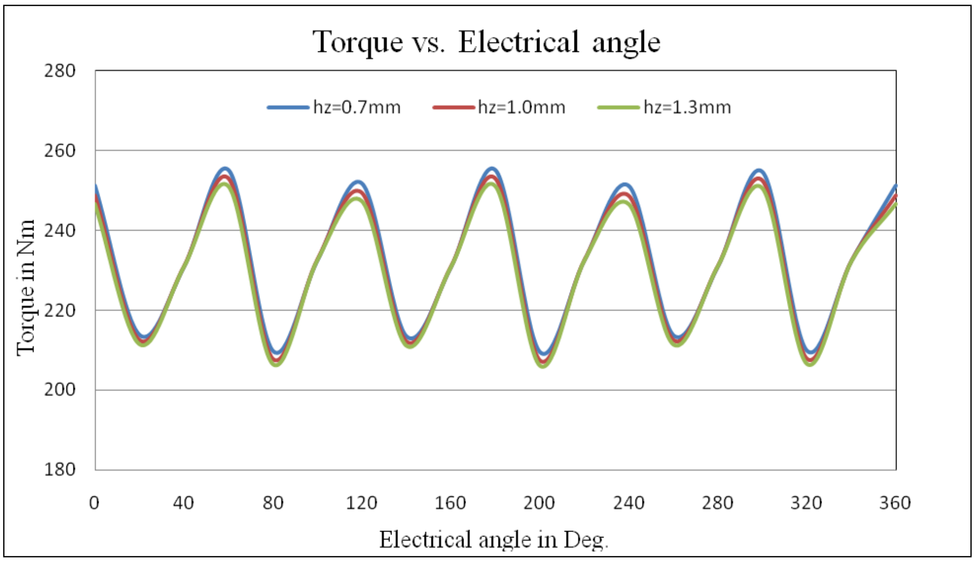

Figure 5-9:Torque curves for the three values of “hz”

Regarding the studied design, these results demonstrate that the change in the height of the pole shoe has no considerable effect on the flux density, nor on the mean value of the torque and the torque ripple in the electrical machine (Tab. 5-5). Consequently, the amplitude of the magnetic forces or, rather, the acoustical behavior of the machine, would not be affected by this variable. Therefore, the height of the pole shoe would not be proposed in the geometrical optimization process of this machine.

hz (mm)	Torque mean value (Nm)	Torque ripple (Nm)
0.7	233	± 21
1.0	232	± 21
1.3	231	± 21

Table 5-5: Torques and torque ripples for the three values of “hz”

Bridge thickness

It is well-known that the bridge thickness has a significant effect on the magnetic design as well as on the mechanical design of the rotor. Therefore, it has to be treated carefully in order to find the optimal value which provides higher torque amplitude and, at the same time, a robust mechanical rotor design. In fact, increasing the bridge thickness makes the rotor mechanically stronger, but this reduces the mean value of the torque. Therefore, the goal is to find out the minimum thickness of the bridge which reduces the leakage flux and, at the same time, ensures a safe mechanical design of the rotor.

The centrifugal forces at high rotational speed introduce a high stress on the bridge body. In fact, the value (tb= 0.9 mm) can be securely applied for this machine up to a rotational speed of 7200 rpm using a steel material with a yield stress of 400 MPa [Elk2007], which is already available on the market.

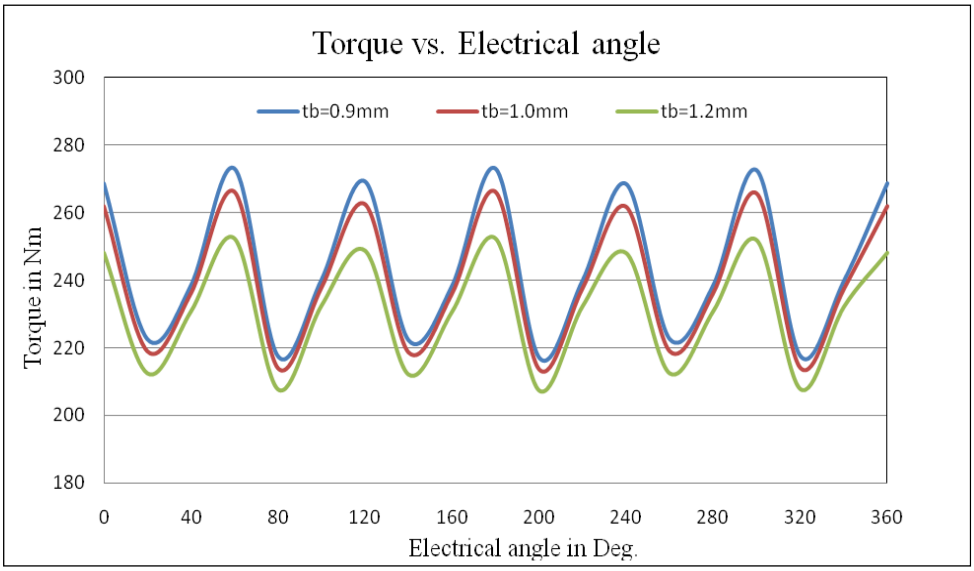

Figure 5-10: Torque curves for the three values of “tb”

tb (mm)	Torque mean value (Nm)	Torque ripple (Nm)
0.9	245	± 28
1.0	240	± 26
1.2	232	± 21

Table 5-6: Torque and torque ripples for the three values of “tb”

Referring to Tab. 5-6, the bridge thickness tb=0.9mm shows an improvement of 5% in torque amplitude from one side, and an increase of 33% in the torque ripple from another side. From the acoustic side, mode 0 reveals an appearance of the frequency orders 90th and 150th in comparison to the original temporal representation. For mode 10, the frequency order 120th appears in addition to the 90th. In spite of these results, the bridge thickness (tb=0.9mm) can be considered an alternative value to the original value, but it should be used in combination with other geometrical variables like “bz”.

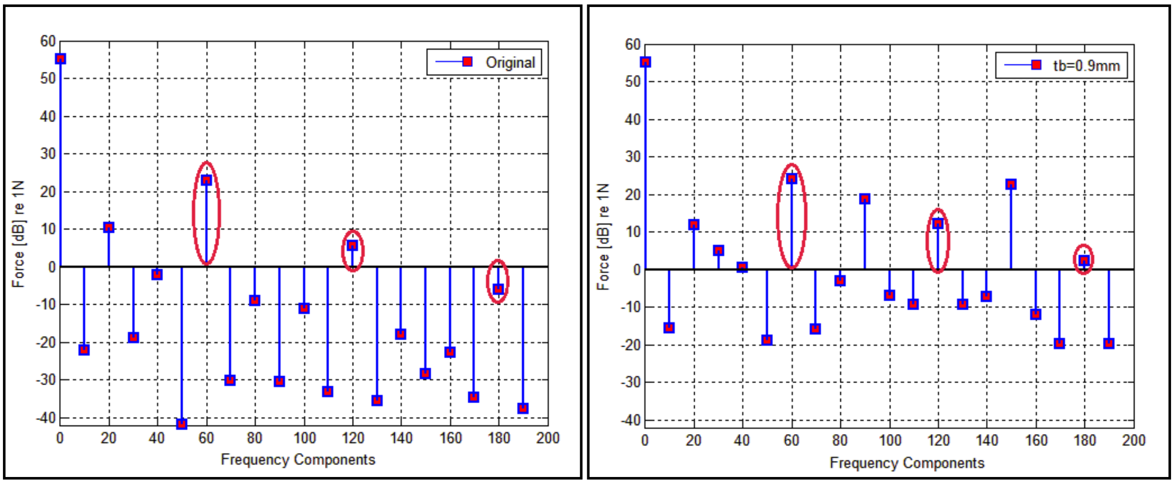

Figure 5-11: Temporal representation of mode 0 with tb=0.9mm and original

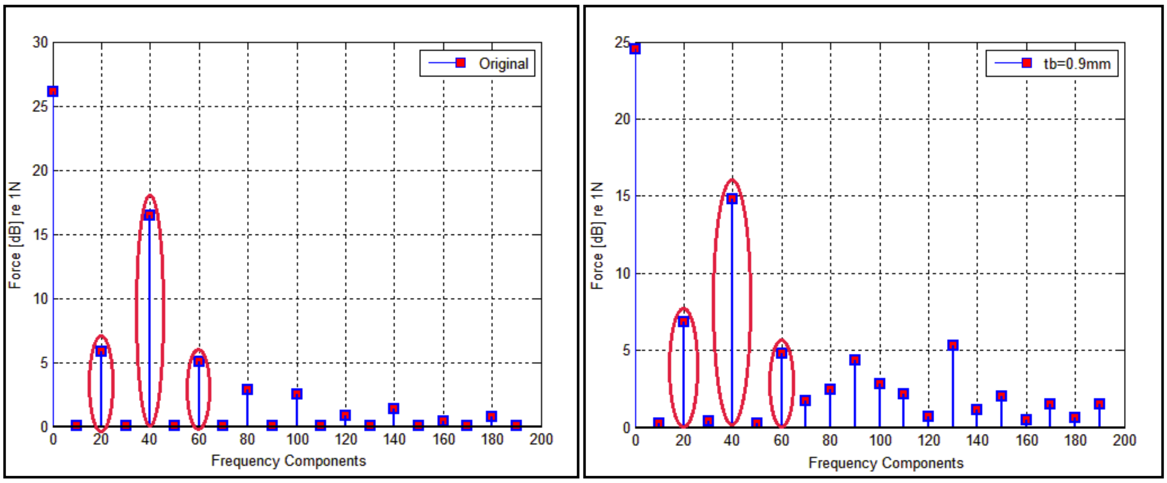

Figure 5-12: Temporal representation of mode 10 with tb=0.9mm and original

Magnet

Two other values are additionally proposed to the actual value of the magnet width “Wmag”. The actual value is Wmag=26 mm, and the two additional values are Wmag=24mm and Wmag=28mm. The torque curves are shown in Fig. 5-13. The torque value increases strongly by 22Nm to 24Nm by enlarging the magnet width by 2mm (see Tab. 5-7).

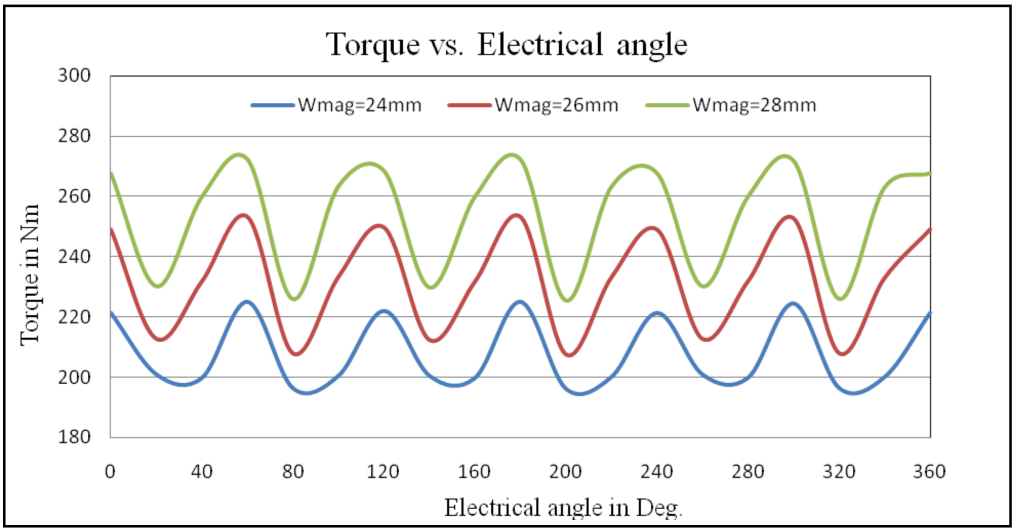

Figure 5-13: Torques curves for the three values of “Wmag”

From one side, a reduction in the magnet width directly affects the torque produced by the machine. This means that this reduction cannot be proposed for the optimization of lamination sheet design because the requested torque needs to be achieved. On the second side, when the magnet width is larger, the volume of the magnets becomes greater and the mass of the magnets increases. This means that the cost of the magnet material, which is the most expensive part in the IPM machine, rises. Due to this finding, it has been considered appropriate to keep the magnet width constant as long as the optimization of other parameters is feasible.

Wmag (mm)	Torque mean value (Nm)	Torque ripple (Nm)
24	208	± 15
26	232	± 21
28	254	± 23

Table 5-7: Torque and torque ripples for the three values of “Wmag”

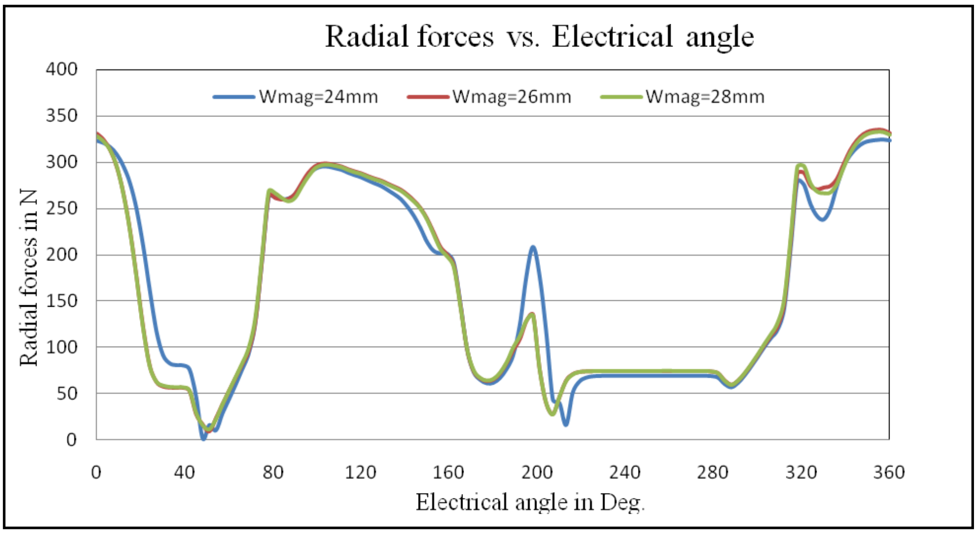

Figure 5-14: Curves of radial forces for the different values of magnet width

5.2.2 Combination

The results of the analysis of each parameter individually, as performed previously, give an idea about the important parameters which can be used in the overall geometrical optimization of the machine. In this phase, these important parameters have to be combined with each other in one lamination sheet design. The purpose is to obtain their overall effect on the entire performance of the machine. The combination is done by using the optimal value of slot opening (or lower tooth width) with the optimal value of the bridge thickness in one lamination sheet design. The other parameters are kept constant. The results of flux density, the torque, the torque ripple and the radial forces are compared with the original design.

As shown in Tab. 5-8, the geometrical optimization using the slot opening or rather the lower tooth width and the bridge thickness together, brings an improvement of 6% to the torque value and, contrarily, an increase of 19% in the torque ripple.

Parameters (unit)	Original Value	Optimal Value	Modification [%]
tb (mm)	1.2	0.9	--
bz (mm)	17.5	15.5	--
Torque (Nm)	232	246	6 %
Torque ripple (Nm)	±21	±26	19 %

Table 5-8: Optimized values of “tb” and “bz” and their effects on the torque and torque ripple

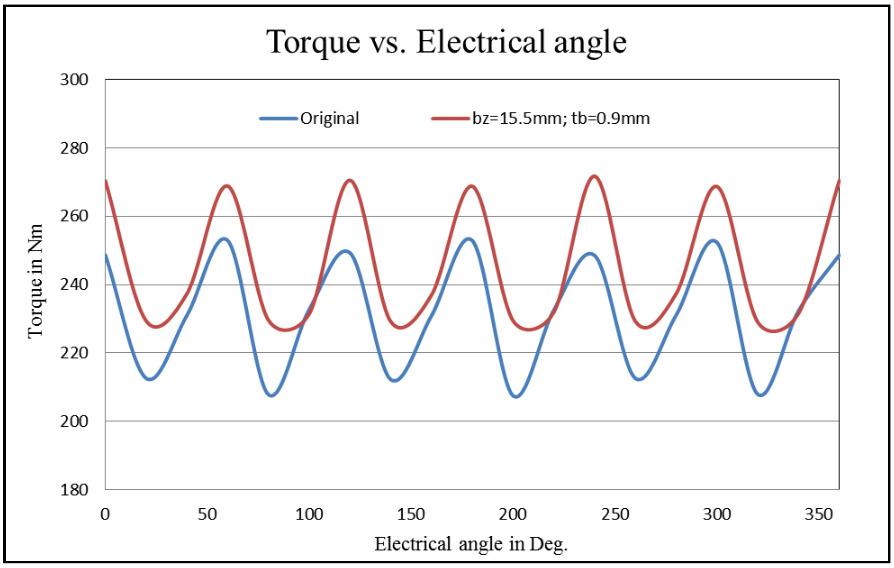

Figure 5-15: Torque curves for the original and optimal designs

The reduction in the lower tooth width decreases the front area of every tooth by at least 2mm^2. It means that the mass of the lamination steel sheets in the stator is decreased. For the large-volume production, this reduction has a considerable value; for example, if 100,000 machines are planned for production according to this optimized geometrical form, the value added can then be summarized by 385 additional stator cores. It can be calculated as follows:

$$N_c = \frac{M_{con}}{M_c} = \frac{3300}{8.56} = 385 \tag{5.1}$$

where M_c is the mass of the stator core in kg, M_{con} the mass of conserved material by using the optimal design for the 100,000 machines, N_c the additional stator core number.

From the acoustic side, Fig. 5-16 shows the influence of the geometrical optimization on the spatial behavior of radial forces. The temporal representation of radial forces on mode 0 and 10 are demonstrated in Fig. 5-17 and 5-18.

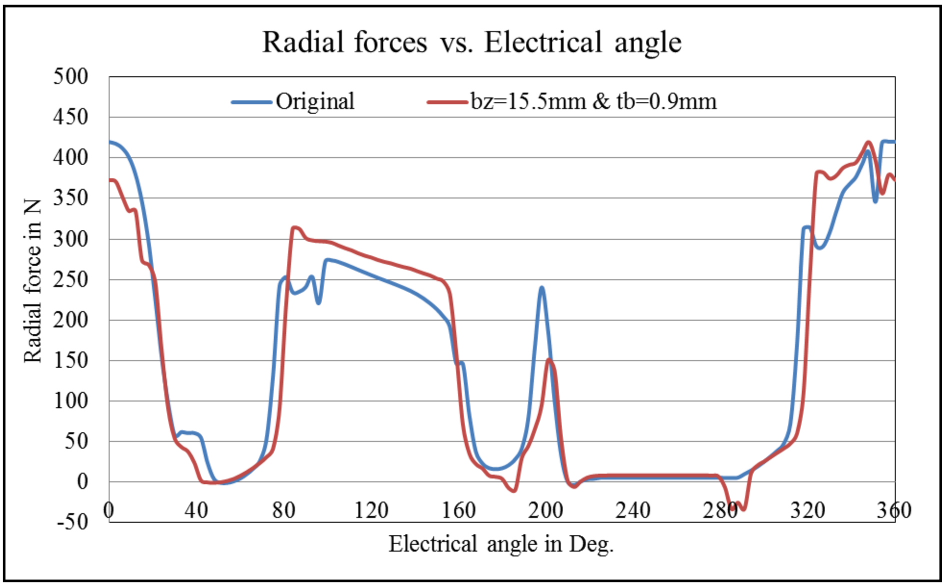

Figure 5-16: Spatial representation of radial forces

Mode 0, which appears with the frequency orders 60th, 120th, 180th and so on, reveals additionally the frequency order 30th with the optimized values of “bz” and “tb”; but, referring to the selected combination of tooth and pole numbers, the frequency order 30th does not excite mode 0 in normal mode operation, where the machine is neither in short-circuit mode nor under open loop mode. On the opposite side, the frequency order 60th is decreased by 9dB force, which demonstrates an improvement of 39%.

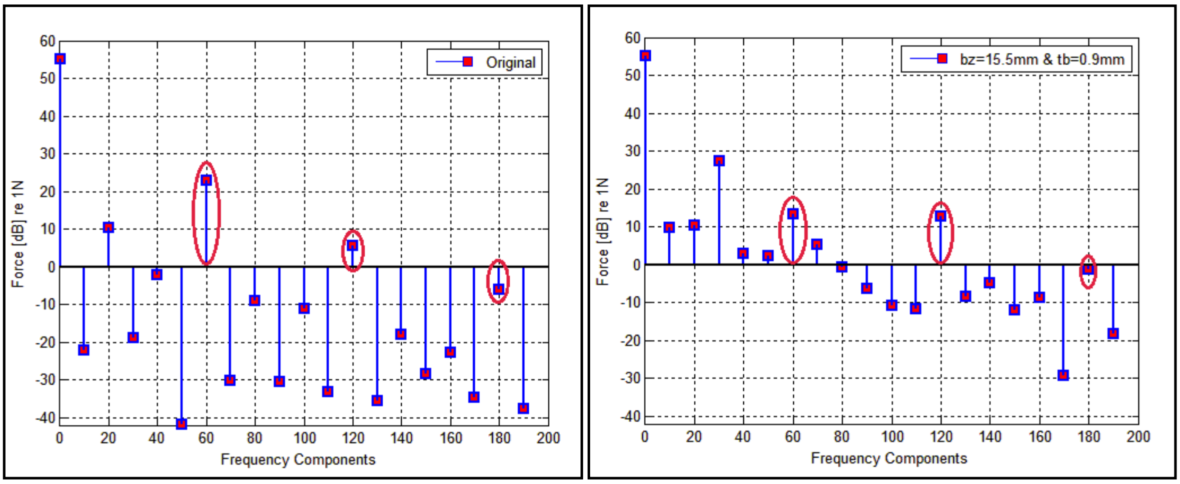

Figure 5-17: Temporal representation of mode “0”

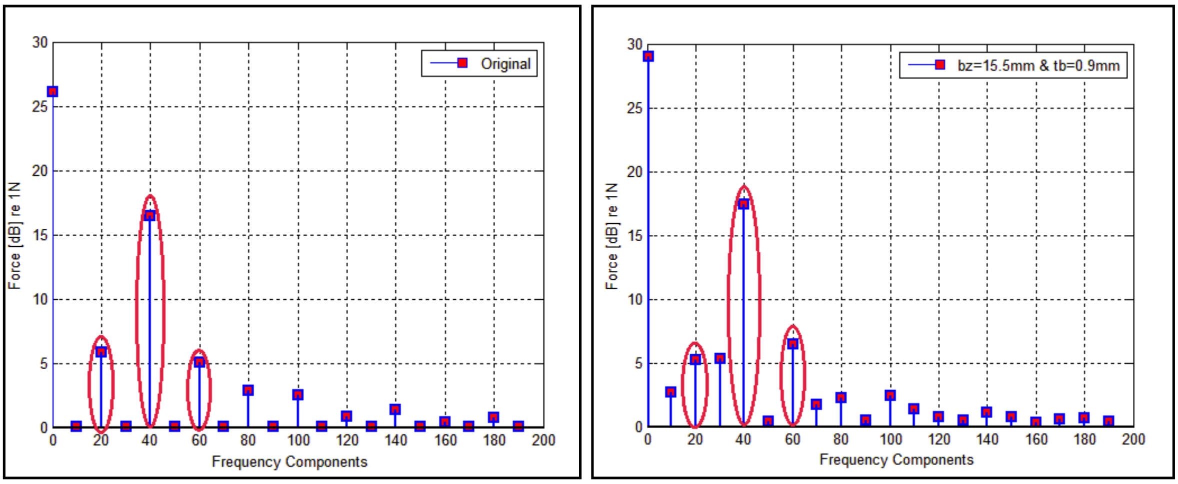

Figure 5-18: Temporal representation of mode “10”

Concerning mode 10, there is no significant effect on its temporal behaviour except for the appearance of the frequency order 30th with an amplitude of 5dB force. As a conclusion, the geometrical optimization has revealed an improvement in the torque mean value. Acoustically, it is expected to reach a better acoustic behaviour in mode 0 and especially with the frequency order 60th, which corresponds to mode 0.

5.3 Step-Skew in Rotor

5.3.1 Overview

In order to reduce the cogging torque, the torque ripple, the vibrations and the noise, the permanent magnet rotors in brushless machines with higher performance are usually skewed [Kai2010 and Yam2006].

A skew in permanent magnet rotor is provided by arranging the magnet stacks successively around the axis of the rotor with an offset angle between them: it is then called a step-skew. In the step-skew structure, the segment magnets are therefore stacked in the magnet stacks of the lamination sheets one upon the other in the axial direction [Oku2011]. The skew pattern is usually defined by the skew angle, which is the angle of rotation about the rotor axis between individual permanent magnets adjacent to each of the skew steps [Kai2010]. As shown in Fig. 5-19, the skew pattern may be symmetric along the rotor axis and may be an axially-symmetric V-shape [Kai2010].

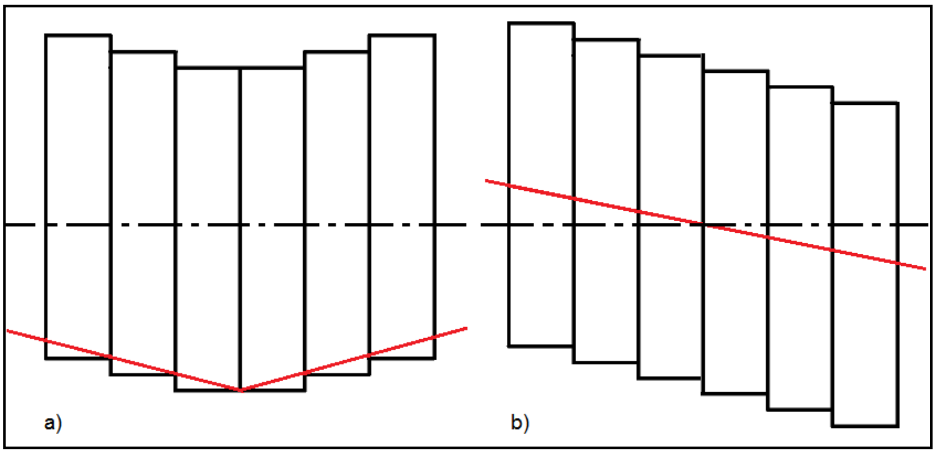

Figure 5-19: Step skewing in V-shape a) and linear b)

In order to determine the skew angle for reducing the torque ripple or, rather, the cogging torque, it is necessary, firstly, to understand the "cogging" phenomenon. In fact, the cogging torque is caused by the variation of the magnetic permeance when the rotor pole passes the slot openings and the stator teeth with un-energized stator windings. When the rotor pole stands on the slot opening where the magnetic circuit reluctance is high (or the magnetic permeance is low), it attempts to align itself with the stator tooth where the magnetic circuit reluctance is low (or the magnetic permeance is highest); so it depends on the rotor pole position with respect to the stator tooth (see also [Wal2007]). The theoretical skew angle, at which the cogging torque is expected to be minimized (see Eq. 5.2) is [Yam2006]:

$$\theta_s = \frac{360}{LCM * N_s}, \tag{5.2}$$

where LCM is the least common multiple of the number of stator teeth and the number of rotor poles, and N_s is the number of permanent magnet rows or stacks in the axial direction.

The theoretical skew angle is sometimes described by the number of skew steps N_{skew} instead of the number of permanent magnet stacks. The relation between the number of permanent magnet stacks and the number of skew steps is:

$$N_s = N_{skew} + 1. \tag{5.3}$$

In fact, the number of skew steps N_{skew} is the number of stacks rotated with respect to the first permanent magnet stack (see Fig. 5-20).

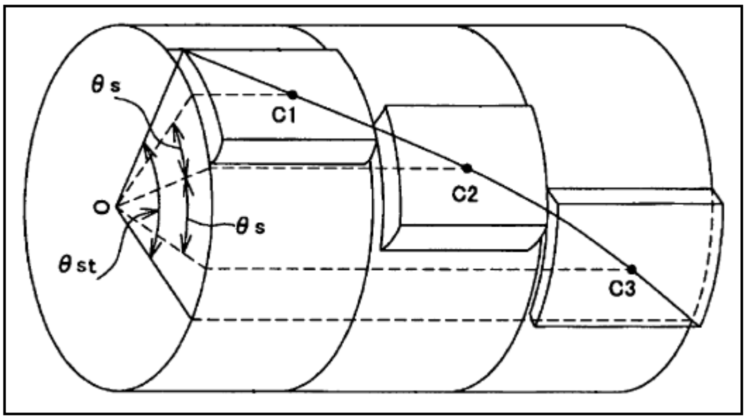

Figure 5-20: Determination of skewing angles [Oku2011]

The calculation of the skew angle is further refined by [Kai2010] into the following formula:

$$\theta_s = \frac{360°}{LCM * (N_{skew} + 1)} \pm \delta_V , \tag{5.4}$$

where δ_V is the variance factor. The variance factor may be up to 20% of the skew angle, and it accounts for manufacturing tolerances and errors and also accounts for design variations from the base equation.

For the studied machine, where the pole number is equal to 20 and the stator teeth are equal to 30, the theoretical angle θ_s is calculated by considering seven permanent magnet rows according to Eq. 5.2:

$$\theta_s = \frac{360°}{60 \times 7} = 0.85° \tag{5.5}$$

Using a negative variance factor δ_V, the skew angle θ_s can be recalculated according to Eq. 5.4:

$$\theta_s = \frac{360°}{60 \times 7} - \frac{360°}{60 \times 7} \times 0.2 = 0.85° \times 0.8 = 0.68° \tag{5.6}$$

The total skew angle θ_{st} is calculated mechanically by:

$$\theta_{st} = \theta_s \times N_s = 0.68° \times 7 = 4.76° .$$

It is also possible to represent the total electrical skew angle θ_{ste} as follow:

$$\theta_{ste} = \theta_{st} \times p = 4.76° \times 10 = 47.6° ,$$

where p is the pole-pair number.

The skew in permanent magnet motors is not only provided to reduce the cogging torque, but also to minimize the torque ripple. In fact, a torque ripple component, corresponding to twice the number of phases (6th harmonic for the 3-phase machine), is particularly detrimental because of its dominance in the distribution of harmonic content [Bri1988]. Generally this torque ripple component is caused by fifth and seventh harmonics of the cogging torque [Yam2006]. Thus, the goal is to reduce these fifth and seventh harmonics of the cogging torque using the skew angle, in order to minimize the torque ripple in the machine. The relationship between the skew angle and the torque ripple is analyzed by the skew factor.

The skew factor $\xi_{sk,v}$ for the v harmonic component of the cogging torque can be represented as in the following expression [Mue2008]:

$$\xi_{sk,v} = \frac{\sin(v\theta_{ste}/2)}{v\theta_{ste}/2} \tag{5.7}$$

The skew factor ξ_{sk} for the first harmonic is defined by:

$$\xi_{sk} = \frac{\sin(\theta_{ste}/2)}{\theta_{ste}/2} \tag{5.8}$$

To demonstrate how to choose the skew angle that gives the minimal possible values for the skew factors of these harmonics, it is necessary to plot the skew factors for the dominant harmonics with respect to the angle $\theta_{ste}/2$, as shown in Fig. 5-21.The skew factors corresponding to the skew angle θ_{ste} are represented by the angle $\theta_{ste}/2$ =23.8° along the x-axis. The skew factors for the fifth and seventh harmonics are then given by 0.42 and 0.08, respectively. Furthermore, it is clearly demonstrated that there is no possibility of bringing the skew factors of these dominant harmonics to zero at the same time. Besides, without skewing the rotor, the skew factors for the harmonics would be equal to one, which means a full presence of the fifth and seventh harmonics in the torque ripple. Using this skew angle θ_{ste}, the cogging torque and the torque ripple are fairly reduced at the same time.

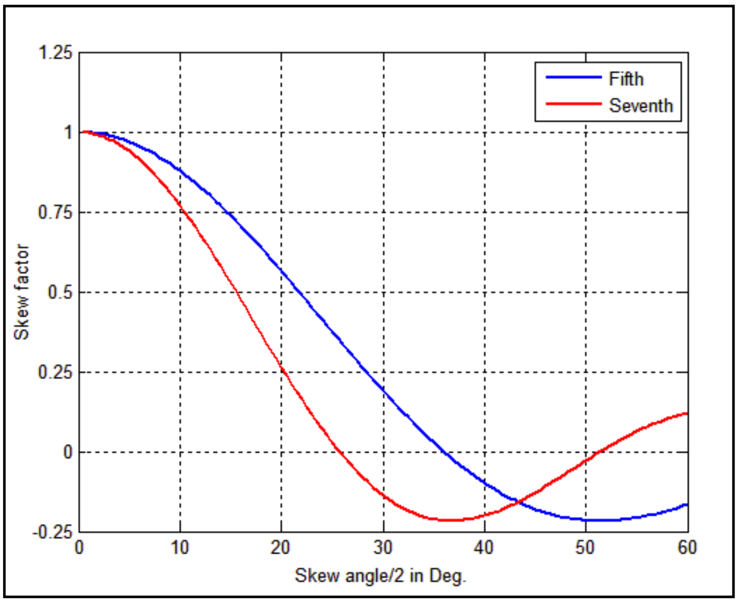

Figure 5-21: Skew factors for the fifth and seventh harmonics versus $\theta_{ste}/2$

5.3.2 Skewing in FEM

As theoretically described, the skew phenomena suppress the harmonics existing in the air gap and minimize their amplitude. Consequently, the tangential and radial forces are clearly affected. The reduction in tangential forces exhibits a significant decrease in the torque ripple, which is strongly recommended. It also influences the torque average value and pulls it slightly down. In order to show the skewing effect, the original and the optimized designs are skewed with the same angle. The results in Tab. 5-9 demonstrate a reduction in the torque ripple between 38% and 42% and a decrease between 4% and 6% in the average value of torque for both models, respectively. In fact, the skewing effect influences efficiently the torque ripple much more than the average torque value (see Fig. 5-22).

	Original design			Optimal design		
Rotor	without skewing	with skewing	Difference [%]	without skewing	with skewing	Difference [%]
Torque [Nm]	232	223	4%	246	232	6%
Torque ripple [Nm]	±21	±13	38%	±26	±15	42%

Table 5-9: Torque results of the original and optimal designs with skewed rotor

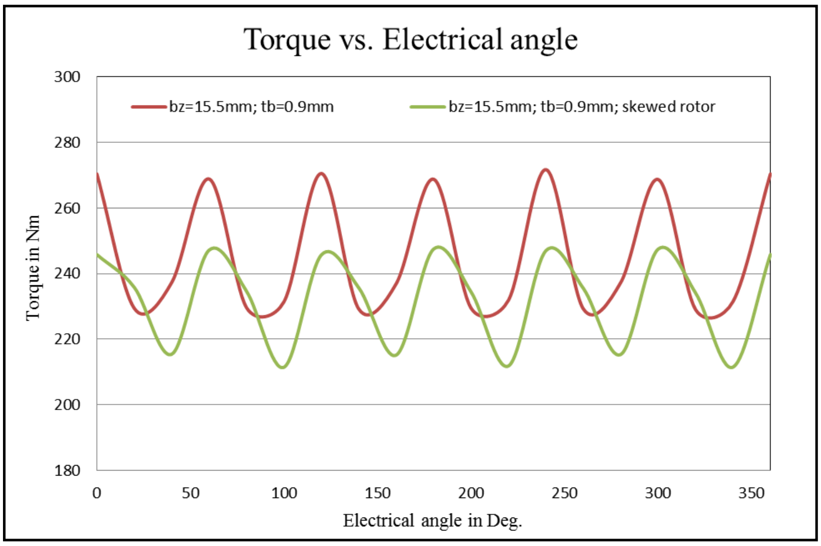

Figure 5-22: Torque curves of the optimal design with and without skewed rotor

Concerning the radial forces, the skewed effect has to be examined in the spatial as well as in the temporal domain. So referring to Fig. 5-23, the spatial representation of the radial forces reveals a considerable reduction in the amplitude of the radial forces with a skewed rotor. However, an increase in the force amplitude at some few points has occurred.

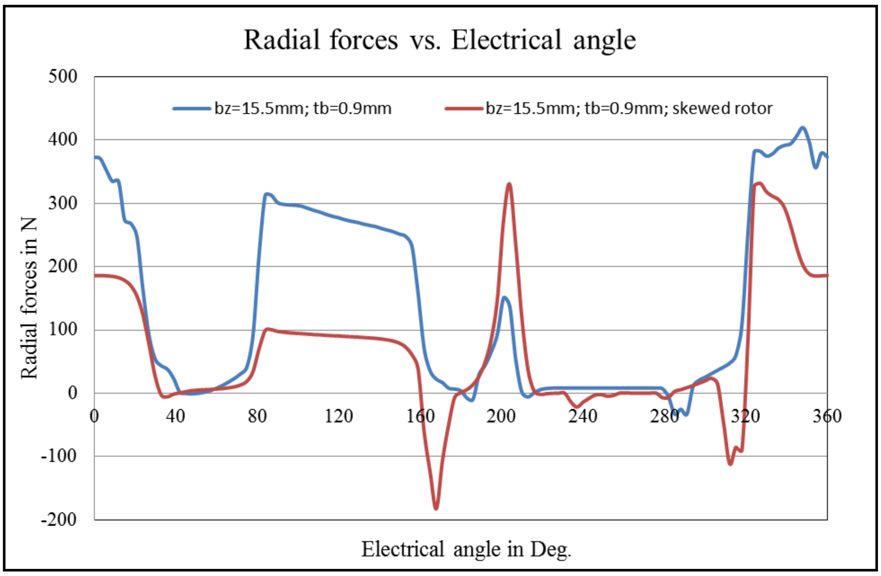

Figure 5-23: Curves of radial forces of the optimal design with and without skewed rotor

In order to explore the modification on the noise behaviour of the machine, the temporal representation for the two dominant modes is performed. First of all, a reduction in the static component (or zero component) by the two investigeted modes is clearly demonstrated. Nevertheless, the fourier decomposition of mode zero with the skewed rotor in Fig. 5-24 reveals an unclear response and gives no judgment on the skewing effect. The reason behind this is actually located in the simulation method used for the temporal representation. As described in Chapter 1, the full electric period is divided into 60 time-steps, where each step represents a specific point in temporal domain. To include the skewing effect in the temporal representation, each point has to be investigated several times to cover all skewing steps. Consequently, the number of simulations which have to be performed with a skewed rotor are equal to 420 simulations (60 points ×7 rotated rotor segments). To reduce this enormous number of simulations, the 60 time points are changed to 36 points. This reduction in the resolution affects in particular the mode zero which is only represented by the cosin part. Regarding mode 10, the fourier decomposition reveals a considerable improvement along its entire behavior. This improvement is denoted by -41% in the static component, -80% and -49% by in the 20th and 40th orders, respectively.

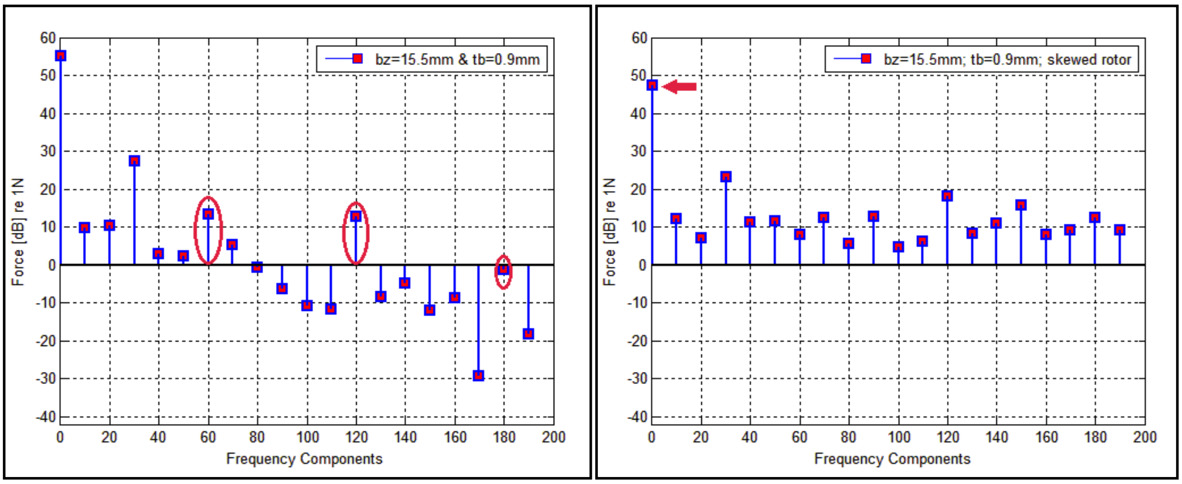

Figure 5-24: Mode zero before and after the skewing process

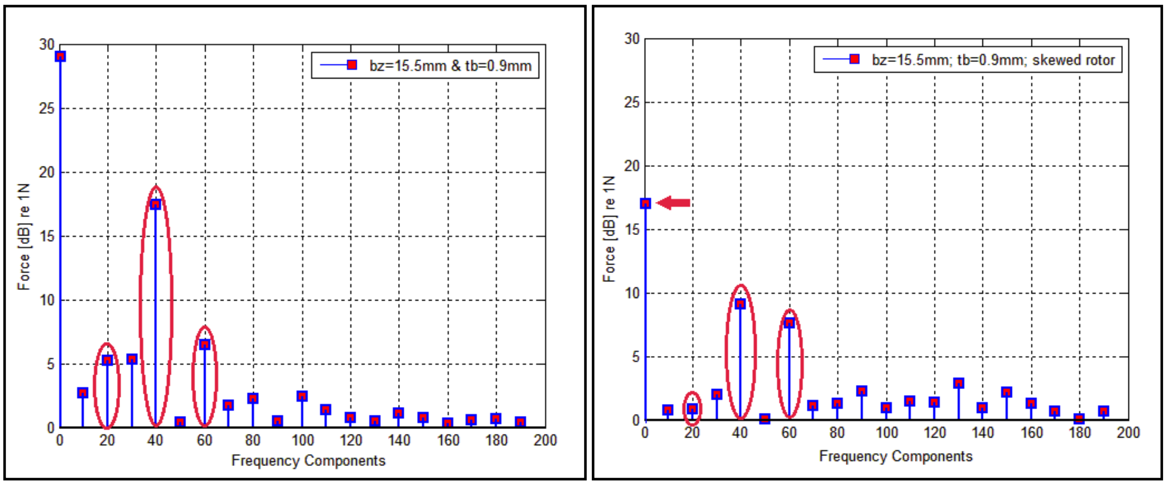

Figure 5-25: Mode 10 before and after the skewing process

5.4 Interpretation

In order to refine the original design and to improve the performance of the studied machine, an electromagnetic optimisation process has already been accomplished. The optimisation targets were the acoustical behavior, the torque ripple and the mean value of torque appearing in the machine. The optimisation process is performed through two parallel paths which are introduced by the geometrical optimisation and the skewing process. In the geometrical optimisation, the laminated sheet design is carefully analyzed in order to find out the parameters that affect the electromagnetic design of the machine and introduce a considerable improvement in its performance. The selection and the modification of parameters has always been exposed to different conditions, taking into consideration not only the electromagnetic side but also the mechanical and the cost sides. Based on these criteria, the optimal geometrical design has been reached. After that, the rotor of these two design models is subjected to the skew process in order to indicate the skewing effect on the vibrational and acoustical behavior, the torque mean value, the torque ripple and also on the entire performance of the machine. Finally the optimal design shows an improved acoustical behavior and also a higher average torque than the original design (see Tab. 5-9).

6 Conclusion

In this thesis, the electromagnetic noise for IPM machines was described. A methodology for the investigation of this noise in IPM machines and especially in those for hybrid vehicles was introduced.

In this work, the analysis of the electromagnetic noise has been clearly analyzed, starting from the electromagnetic design of IPM machine.The reasons behind the generation of the electromagnetic noise and the causes of their occurrence were carefully explained. Also, the medium, where the electromagnetic forces principally act and contribute to the vibration excitation of the system structure of the IPM machine, thus producing the generation process of noise into the surrounding area was introduced. The description of the electromagnetic forces was presented in time and space separately. These forces were split into components. Each component was associated with the corresponding mechanical mode. The way to superimpose these forces on the stator structure was well reflected upon.

This thesis has revealed the effect of different design methods on the noise generation of the IPM machine; Starting from the electromagnetic construction by implementing a non-overlapping windings concept in the stator, passing through the mechanical construction, where individual teeth have been used for building the stator core and a stator frame with surrounding cooling channels to form together the complete stator. The concept of individual teeth has been treated by introducing the different tooth designs and the way of assembling them. The structure of the stator was examinated analytically, numerically and experimentally to assure realistic simulation conditions. Also, the assembly process of the stator and its influence on the generated noise were particularly explained, based on experimental investigation. The damping and friction factors, which are affected by the assembly process of the stator, were then deduced. The harmonic and acoustic simulation of each mechanical mode was performed separately. The numerical method BEM was implemented to investigate the structure borne sound of each mode. The air borne sound was predicted on a spherical surface with one meter diameter around the stator structure.

The sensibility process carried out here on the electromagnetic design has revealed the importance of the geometrical shape of laminations and the skewing process on the performance and on the noise behavior of IPM machine. The sensibility process was achieved by selecting geometrical parameters which have influence on the electromagnetic behaviour of the IPM machine. Each parameter was investigated in a feasible range. The optimal value was found considering the machine performance, the assembly process and the acoutisc behavior of the machine. At the end, all optimized parameters were combined to discover the optimal design.

Moreover, the simulation process for electromagnetic noise in IPM machine was introduced in detail with the connection points between the different types of simulation. These simulations on electromagnetic, mechanical and acoustic fields revealed the important variables that contribute to the evaluation process of the generated noise in IPM machines. Generally, this chain of simulations is independent of the used tools and can be performed using other available tools.

A wide understanding on the generation process of noise in electric machines and a reasonable approach to its evaluation process was accomplished, which can assist principally in the investigation of electromagnetic noise in electric machines.

Finally, it was found that the used methodology can be applied to all kind of electric motors and that the different simulation procedures should be the same in every investigation of electromagnetic noise.

7 Future Work

A further development and improvement of the simulation process will help to establish a greater degree of accuracy in the final results. This can be done by coupling the different software or tools together under one platform or by using one programming language to simplify the optimization loop and to allow the application of an iterative optimization loop, starting with the electromagnetic analysis and ending with the acoustic simulation in order to explore the effect on the generated noise.

It would be interesting to investigate more operating points with different speeds along the torque-speed curve of the electric machine. The effect on the noise generation process can be explored by comparing the results of these operating points. This will be hepful in understanding the noise behaviour of the electric machine if operated deeply in the field weakening range.

Further research is recommended that might explore the importance of the assembly methods and the materials of the stators on the generation of noise. This can be done by analyzing the structure of the electric machine and the different methods that can be implemented to affect its dynamic response.

Furthermore, additional experimental investigations on acoustic will help to ensure realistic boundary conditions for the simulation and improve the accuracy of the results. However, more research is needed to reach a certain consistency between the simulation and the measurement results on the test bench and also in the vehicles. Secondly, new methods could be investigated to treat and confront the electromagnetic noise by acoustic waves in order to make it not just acceptable but also convenient.

List of Symbols

Greek Symbols:

α	Geometrical circumferential angle
δ_v	Variance factor
ε	Relative eccentricity
ε_x	Longitudinal strain
ε_θ	Circumferential strain
$\varepsilon_{x\theta}$	Shear strain in plan xθ
θ_s	Skew angle
θ_{st}	Total skew angle
θ_{ste}	Total electrical skew angle
Θ	Magnetic field
Θ	Magnetomotive force (mmf)
Λ_g	Relative permeance
λ	Frequency parameter
λ_s	Wave length
μ	Rotor harmonic number
μ_0	Permeability of free space
ν	Stator harmonic number
ν_p	Poisson’s ratio
v_s	Particle velocity
ξ_z	Zone factor
ξ_s	Pitch factor
ξ_{sk}	Skew factor
ρ	Material density
σ_s	Radiation efficiency
τ	Pole pitch
ω	Electrical angular frequency

Symbols:

b_s	Slot opening
b_{sat}	Slot opening under saturation
b_x	Tangential flux density
b_y	Radial flux density
bz	Lower tooth width
c	Speed of sound propagation
c_a	Speed of sound in air
c_{SL}	Speed of sound in solids
D_c	Mean diameter of the stator core
e	Eccentricity
E	Young’s modulus
f	frequency
g	Gravity acceleration
g_{nom}	Nominal air gap
G_m	Shear modulus
h_c	Yoke thickness
hs	Height of pole shoe
i	Alternating current
I	Current amplitude
I_s	Instantaneous sound intensity

I_n	Normal sound intensity
k_c	Carter factor
k_{in}	Stacking factor
k_n	Wave number
K	Bulk modulus
LCM	Least common multiple of stator teeth and rotor pole numbers
L_p	Sound pressure level
L_{In}	Normal sound intensity level
L_v	Sound velocity level
L_w	Sound power level
m_C	Mass of stator core
m_{in}	Mass of insulation material
m_{ph}	Number of phases
m_t	Total mass of stator
m_w	Mass of winding
n_s	Number of coils in the electric machine
n_{sp}	Number of coils / phase
n_{zp}	Number of zones / phase
N	Number of turns per coil
N_s	Number of magnets or stacks in axial direction
p	Pole-pair number
p_s	Sound pressure
$\vec{P}$	Maxwellian stress Vector
P_s	Sound power
$\vec{P}_{rad}$	Radial surface force
$\vec{P}_{\tan}$	Tangential surface force
q	Number of slots per pole per phase
r	Mode index
r_s	Radius or distance from sound source
R_C	Mean radius of the stator core
s	Slot pitch
t	Time
tb	Bridge thickness
$\mathrm{T}_{\mathrm{FEM}}$	Torque of the finite element method
V	Volume
y	Coil width
$Wmag$	Width of magnet
Z	Number of teeth
Z_a	Specific acoustic impedance for air
Z_{mech}	Specific mechanical impedance
Z_{rad}	Specific radiation impedance

Bibliography

[Abr1972]: M. Abrmowitz, I.A. Stegun. *Handbook of mathematical functions.*United States Department Of Commerce, National Bureau of Standards, Applied Mathematics Series – 55, Dover Publications, New York NY, 1972.

[Adz2008]: L. Adzi. Entwicklung von Internetdiensten im Bereich der elektrischen Maschinenauslegung.*PhD Thesis, University of Kassel*, 2008.

[Alr2010]: Z. Al Rifai.Erstellung von Modellen zur Analyse der Akustik einer PM-Maschine. *Diplom Thesis, Hochschule Bochum*, 2010.

[Anw2000]: M. N. Anwar, I. Husain. Radial force calculation and acoustic noise prediction in switched reluctance machines. *IEEE Transactions on Industry Applications, Vol.36, pages 1589-1597,* 2000.

[Ari2001]: G. Arians. Numerische Berechnung der elektromagnetischen Feldverteilung, der strukturdynamischen Eigenschaften und der Geräusche von Asynchronmaschinen.*Shaker* Verlag 157, Aachen, 2001.

[Asa2002]: Y. Asano, Y. Honda, H. Murakami. Novel Noise Improvement Technique for a PMSM with Concentrated Winding. *IEEE Power Conversion Conference, PCC-Osaka,* 2002.

[Avi2001]: P. Avitabile. Experimental Modal Analysis, A simple Non-Mathematical Presentation. *Sound and Vibration, University of Massachusetts Lowell*, 2001.

[Bea1995]:C. F. Beards.*Engineering Vibration Analysis with Application to Control Systems.* Published by Edward Arnold, Great Britain, ISBN 0 340 63183 X,1995.

[Bel2004]: A. Belahcen. Magnetoelasticity, Magnetic Forces and Magnetostriction in Electrical Machines. *PhD Thesis, Helsinki University of Technology,* 2004.

[Bla2008]: J. Blauert,N. Xiang. *Acoustics for Engineers*. Springer-Verlag Berlin Heidelberg, ISBN 978-3-540-76346-8, 2008.

[Ble1995]: R. Blevins.*Formulas for natural frequency and mode shape*. Krieger Publishing Company, Malabar, Florida, 1995.

[Boe2008]: M. Boesing, K. A. Kasper, R. W. De Doncker. Vibration Excitation in an Electric Traction Motor for a Hybrid Electric Vehicle. *37th International Congress and Exposition on Noise Control Engineering, Shanghai China*, 2008.

[Bri1988]: R. N. Brigham, J. R. Vivirito. *Means to Reduce Harmonic Torque in Electromagnetic Machines*. United States Patent – Patent No. 4,739,201, 1988.

[Cai2001]: W. Cai, P.Pillay, A.Omekanda. Analytical Formulae for Calculating SRM Modal Frequencies for Reduced Vibration and Acoustic Noise Design. *IEEE International Electric Machines and Drives Conference IEMDC, pages 203–207,* 2001.

[Cai2001']: W.Cai, P. Pillay. Resonant Frequencies and Mode Shapes of Switched Reluctance Motors. *IEEE Transactions on Energy conversion, Vol. 16, No.1,* 2001.

[Cam1992]: D.E. Cameron, J. H. Lang, S.D. Umans. The origin and reduction of acoustic noise in doubly salient variable-reluctance motors. *IEEE Transactions on Industry Applications, Vol. 28, No.6, pages 1250-1255,* 1992.

[Che2006]: Y. S. Chen, Z. Q. Zhu, D. Howe. Vibration of PM Brushless Machine Having a Fractional Number of Slots per Pole. *IEEE Transactions on Magnetics Vol. 42,* 2006.

[Che2008]: Y. Chen, H. Yang, Z. H. Han. Investigation of electromagnetic vibration of permanent magnet brushless machines. *IEEE Electrical Machines and Systems, ICEMS* 2008.

[Cra2005]: L. G. Cravero. Entwurf, Auslegung und Betriebsverhalten von dauermagneterregten bürstenlosen Motoren kleiner Leistung. *PhD thesis Technical University Ilmenau*, 2005.

[Cre2005]: L. Cremer, M. Heckl, B.A.T. Petersson.*Structure-Borne Sound, Structural Vibrations and Sound Radiation at Audio Frequencies*.Springer Berlin Heidelberg, ISBN 3-540-22696-6, 2005.

[Cro2002]: J. Cros and P. Viarouge. Synthesis of high performance PM motors with concentrated windings. *IEEE Trans. on Energy Conversion, vol.17, no.2, pp. 248-253,* 2002.

[DeM1998]: L. H. De Medeiros, G. Reyne, G. Meunier. Comparison of Global Force Calculation on permanent Magnets. *IEEE Transactions on Magnetics Vol. 34,* 1998.

[Div2011]: M. Divandari, M. M. Kabir. Acoustic Noise Reduction of Switched Reluctance Motor Drives. Middle-East Journal of Scientific Research 8. IDOSI Publications, 2011.

[Ebr2008]: M. B. Ebrahimi, J. Faiz, M. J. Roshtkhari and A. Z. Nejhad.Static Eccentricity Fault Diagnosis in Permanent Magnet Synchronous Motor Using Time Stepping Finite Element Method. *IEEE Transactions on Magnetics, Vol. 44, No. 11, pp. 4297-4300,* 2008.

[Eic2007]: J. Eichler. *Physik Grundlagen für das Ingenieurstudium – kurz und prägnant*. Friedr. Vieweg & Sohn Verlag / GWV Fachvertrage GmbH, Wiesbaden, ISBN 97B-3-834B-0223-1, 2007.

[Ehs2010]: M. Ehsani, Y. Gao, A. Emadi. *Modern Electric, Hybrid Electric, and Fuel Cell Vehicles Fundamentals, Theory, and Design*. CRC Press,Taylor & Francis Group, ISBN: 978-1-4200-5398-2, 2010.

[Elk2007]: Z. El-Khawly; Modelling and Optimizing Mechanically a Rotor of an Interior Permanent Magnet Synchronous Motor for Hybrid Vehicles; *Master Thesis, University of Duisburg-Essen, Germany,* 2007.

[Fah2003]: F. Fahy. *Foundations of Engineering Acoustics.*Elsevier Ltd., ISBN: 978-0-12-247665-5, 2003.

[Ger2010]: D. Gerling. Lectures: Elektrische Maschinen und Antriebe. *Lehrstuhl für Elektrische Antriebstechnik und Aktorik, University of the Federal Defense, Munich.* 2010.

[Ger1992]: D. Gerling. Pulswechselrichtergespeiste Käfigläufermaschinen kleinerleistung – Untersuchung hinsichtlich Drehzahlermittlung, Geräusche und elektromagnetischer Störungen. *PhD Thesis, RWTH Aachen University,* 1992.

[Gia2010]: G. Pistoia.*Electric and Hybrid Vehicles Power Sources, Models, Sustainability, Infrastructure and the Market*.ISBN: 978-0-444-53565-8, Elsevier, 2010.

[Gie2007]: J.F. Gieras, C. Wang, J. Lai, N. Ertugrul. Analytical Prediction of Noise of Magnetic Origin Produced by Permanent Magnet Brushless Motors.*IEEE International Electric Machines and Drives Conference IEMDC, Hamilton Sundstrand, Rockford,* 2007.

[Gie2006]: J. F. Gieras, C. Wang, C. J. Lai. *Noise of Polyphase Electric Motors.* s.l.:CRC Taylor & Francis Group, 2006.

[Got2007]: R. Gottkehaskamp. Optimal gefertigt Systematischer Entwurf von dreisträngigen Zahnspulenwicklungen bürstenloser Motoren. *Antriebstechnik Nr. 10, Seite 30,* 2007.

[Grü2006]: A. Grüning. Elektromechanisches Verhalten von Ständerwickelköpfen großer Turbogeneratoren bei stationärem Betrieb und elektrischen Störungen. *PhD Thesis, Universität Dortmund,* 2006.

[Har2005]: R. E. Hartsfield, G. E. Horst, D. M. Hurst, K. A. Sheeran. *Interconnecting Method for Segmented Stator Electric Machines.* United States Patent, Patent No.: US 6,941,638 B2, 2005.

[Hof2005]: H. Hofmann. Darstellung des Betriebsverhaltensdrehzahlvariabler Dauermagnetmaschinenmit dem Kurzschlußstrom als Hauptparameter. *PhD Thesis, University of Federal Defense, Munich,* 2005.

[Hor2005]: G. E. Horst, K. I. Hoemann. *Reduced Coil Segmented Stator.* US Patent Application Publication, Patent No.: US 2005 / 0258706A1.

[Ish2004]: D. Ishak , Z.Q. Zhu, D. Howe. Permanent Magnet Brushless Machines with Unequal Tooth Widths and Similar Slot and Pole Numbers.*IEEE Industry Applications Conference, 39th IAS Annual Meeting,* 2004.

[ISO3744]: EN ISO 3744.*Acoustics. Determination of Sound Power Levels of Noise Sources using Sound Pressure. Engineering Method in an Essentially Free Field over a Reflecting Plane.*ISO 3744:1994.

[ISO9614]: DIN EN ISO 9614-1.*Acoustics –Determination of sound power levels of noise sources using sound intensity –Part 1: Measurement at discrete points.*ISO 9614-1:1993, English version of DIN EN ISO 9614-1:2009.

[Jur2003]: F.Jurisch.Nutrastmomente in elektrischen Maschinen: Neue Betrachtungsweise und Maßnahmen zur gezielten Beeinflussung. *Vacuumschmelze GmbH, DM-PM 4*, 2003.

[Kai2010]: E. L. Kaiser, K. M. Rahman. *Skew Pattern for a Permanent Magnet Motor*.US Patent Application Publication, Patent No. : US 2010/0277027 A1, 2010.

[Kar2007]: M. Karger. Einführung in Die Maschinenakustik. *Fachhochschule Bielefeld*, 2007.

[Ko2004]:H. Ko, K. Kim. Characterization of Noise and Vibration Sources in Interior Permanent-Magnet Brushless DC Motors.*IEEE Transactions on Magnetics, Vol. 40, No. 6, 2004.*

[Kol2005]: S. F. Kolomeitsev, J. R. Suriano. Stator Design for Permanent Magnet Motor with Combination Slot Wedge and Tooth Locator. United States Patent, Patent No.: US 6,844,653 B2, 2005.

[Kur2008]: P. Kurzweil, B. Frenzel, F. Gebhard. *Physik Formelsammlung für Ingenieure und Naturwissenschafter.* Friedr. Vieweg & Sohn Verlag / GWV Fachvertrage GmbH, Wiesbaden, ISBN 97B-3-834B-0251-4, 2008.

[Lac2003]: T. Lachman, T.R. Mohamad, G. L. A. Onyango. Analytical methods for prediction of acoustic noise generation in switched reluctance motors. *Robotics, Intelligent Systems and Signal Processing 2003, Proceedings, 2003 IEEE International Conference on (Volume:1),* 2003.

[Lac2004]: R. Lach, S. Soter. Minimization of vibration and noise stimulation for inverter-fed drives. *Power Conversion Intelligent Motion Power Quality PCIM, Shanghai,* 2004.

[Lac2005]: R. Lach. Magnetische Geräuschemission umrichtergespeister Käfigläufer-Asynchronmaschinen.*PhD Thesis, University of Dortmund,* 2005.

[LeB2008]: J. Le Besnerais. Reduction of magnetic noise in PWM-supplied induction machines, low-noise design rules and multi-objective optimization. *PhD Thesis, Ecole Central de Lille*, 2008.

[Mag2003]: F. Magnussen and C. Sadarangani. Winding factors and joule losses of permanent magnet machines with concentrated windings. *Proc. of Electric Machines and Drives Conference, (IEMDC), vol. 1, pp. 333-339,* 2003.

[Mah1996]: J. Mahn, D. Williams, P. Wung, G. Horst. A systematic approach toward studying noise and vibration in switched reluctance machines: preliminary results. *IEEE Industry Applications Conference, Thirty-First IAS Annual Meeting, IAS '96,*1996.

[Mat2006]: A. Matveev. Development of methods, algorithms and software for optimal design of switched reluctance drives. *PhD Thesis, Technische Universitieit, Eindhoven,* 2006.

[Mei2008]: F. Meier. Permanent-Magnet Synchronous Machines with Non-Overlapping Concentrated Windings for Low-Speed Direct-Drive Applications. *PhD Thesis, Royal Institute of Technology, Sweden,* 2008.

[Mi2011]: Chris. Mi, M. Abul Masrur, D. Wenzhong Gao. *Hybrid Electric Vehicles: Principles and Applications with Practical Perspectives.*John Wiley & Sons, Ltd., ISBN 978-0-470-74773-5, 2011.

[Mös2007]: M. Möser. *Technische Akustik, 7 erweiterte und aktualisierte Auflage*. Springer Berlin Heidelberg, ISBN 978-3-540-71386-9, 2007.

[Mös2009]: M. Möser. *Engineering Acoustics.*Springer-Verlag Berlin Heidelberg, DOI 10.1007/978-3-540-92723-5_4, 2009.

[Mor2010]: K. Moritz. Messtechnik im Maschinenbau Akustikmessungen, Version 3.0.*Technische Universität Darmstadt,* 2010.

[Mue2008]: G. Müller, K. Vogt, B. Ponick. *Berechnung elektrischer Maschinen.* WILEY - VCH Verlag GmbH and Co KgaA, Weinheim, 2008.

[Oku2011]: M. Okubo, M. Kawamura. *Brushless Motor with Skewed Rotor Segments*. US Patent Application Publication, Patent No. : US 7,906,880 B2, 2011.

[Ouy2006]: W. Ouyang, D. Zarko, T.A.Lipo. Permanent Magnet Machine Design Practice and Optimization.*IEEE Industry Applications Conference, 41st IAS Annual Meeting,*2006.

[Ram1983]: K. A. Ramsey. Experimental Modal Analysis, Structural Modifications and FEM Analysis on a Desktop Computer. *Sound and Vibration, Structural Measurement Systems, California,* 1983.

[Rez2010]: A. Rezig, M. R Mekideche, A Djerdir. Effect of Rotor Eccentricity Faults on Noise Generation in Permanent Magnet Synchronous Motors.*Progress in Electromagnetics Research C, Vol. 15, 117,* 2010.

[Ric1967]: R. Richter. *Elektrischer Maschinen, Allgemeine Berechnungselemente, die Gleichstrommaschinen*. Erster Band; Verlag Birkhäuser Basel, 1951.

[Ros2007]: T.D. Rossing.*Springer Handbook of Acoustics*. Springer Science+Business Media, LLC New York, ISBN: 978-0-387-30446-5, 2007.

[Rus1991]: S. Russenschuck. Mathematische Optimierung permanenterregter Synchronmaschinen mit Hilfe der numerischen Feldberechnung.*PhD Thesis, VDI-Verlag GmbH, Düsseldorf*, 1991.

[Sal2004]: P. Salminen, M. Niemelä, J. Pyrhönen, J. Mantere. Performance analysis of fractional slot wound PM-motors for low speed applications. *IEEEindustry applications conference, 39th IAS Annual Meeting, Vol.2, pages 1032-1037*, 2004.

[Tae1994]: F. Taegen, J. Kolbe. Drehmomente und Geräusche der Modularen Dauermagnetmaschine.*Archiv Elektrotechnik 77, Springer-Verlag*, 1994.

[Tat2009]: K. Tatematsu, R. Mizutani, Y. Endo. *Stator core, Motor, and Method of Manufacturing stator*. US Patent, Patent No. : US 2009/0121577 A1, 2009.

[Tim1989]: P.L. Tímár, A. Fazekas, J. Kiss, A. Miklós, S. J. Yang. *Noise and Vibration of Electrical Machines.*Amsterdan-Oxford-New York-Tokyo; Elsevier Science Publishers, 1989.

[Ver1996]: S. P. Verma. Noise and Vibration of electrical machines and drives; their production and means of reduction. *IEEE Power Electronics, Drives and Energy Systems for Industrial Growth*, 1996

[Vij1998]: P. Vijayraghaven, R. Kirshman. Noise in Electric Machines: A Review. *IEEE Industry Applications Conference. Thirty-Third IAS Annual Meeting*, 1998.

[Vor2008]: M. Vorländer. Auralization, *Fundamentals of Acoustics, Modelling, Simulation, Algorithms and Acoustic Virtual Reality.*Springer-Verlag Berlin Heidelberg, ISBN 978-3-540-48829-3, 2008.

[Wal2007]: T. A. Walls, A. D. Crapo. *Permanent Magnet Electric Machine Having Reduced Cogging Torque*. United States Patent – Patent No. : US 7,245,054 B1, 2007.

[Wao2010]: WAON Version 4.0. *User's Manual*. Cybernet Systems Co., Ltd, Chiyoda-ku, Tokyo, 2010.

[Wat1983]: S. Watanabe, S. Kenjo, K. Ide, F. Sato, M. Yamamoto. Natural Frequencies and vibrations Behaviour of Motor Stators. *IEEE Transactions on Power Apparatus and Systems, Vol. PAS-102, No. 4, Toshiba Corporation; Yokohama, Japan,*1983.

[Yam2006]: S. Yamaguchi, H. Kometani, T. Kikuchi, T. Miyazaki. *Permanent-Magnet Rotating Machine*. Patent Application Publication – Pub. No. : US 2006/0192456 A1, 2006.

[Yan2008]: H. Yang, Z. Han, Y. Chen. Electromagnetic Vibration of Interior Permanent Magnet Bruschless Motors under DC and AC Operation.*IEEE Electrical Machines and Systems ICEMS;Tokyo, Japan* 2009.

[Yos2004]: S. Yoshiyuki. *Core and Stator for Motor*. Japan Patent OfficePatent No. 2004328965A, 2004.

[Zar2005]: D. Žarko, D. Ban, T. A. Lipo; *Design Optimization of Interior Permanent Magnet (IPM) Motors With Maximized Torque Output in the Entire Speed Range*.EPE ISBN : 90-75815-08-5, Dresden, 2005.

[Zep2006]: L. P. Zepp. *Electrical Machine Construction Using Axially Inserted Teeth in a Stator Ring or Armature*. Patentnr. US 7042130 B2, 2006.

[Zhu1993]:Z. Q. Zhu, D. Howe. Instantaneous Magnetic Field Distribution in Brushless Permanent Magnet dc Motors, Part III: Effect of Stator Slotting.*IEEE Transactions on Magnetics, 29 (1),* January 1993.

[Zhu2002]: Z.Q. Zhu, D. Howe, C.C. Chan. Improved Analytical Model for Predicting the Magnetic Field Distribution in Brushless Permanent-Magnet Machines. *IEEE Transactions on Magnetics, Vol. 38, NO. 1,* 2002.

Internet sites:

[Ans2010]: Wiki Answers; *What are wavefronts?*; Answers Corporation 2010
http://wiki.answers.com/Q/What_are_wavefronts

[Eia2009]: U.S. Energy Information Administration, Independent Statistics and Analysis. Accessed 2009.

http://www.eia.doe.gov/steo/contents.html

[Eme2009]: S. Meier, F. Meier. Emetor a PMSM Design Tool. Electrical Machines and Power Electronics; KTH Royal institute of Technology
http://www.eme.ee.kth.se/emetor/emetor.php?file=models

[Gas2010]: Gasgoo Global Auto Sources, *Ningbo OMEDA Auto Part co.,Ltd.,Client: Valeo,* (cited: 2010).
http://www.gasgoo.com/auto-parts-trade/image-QSKNT/Progressive-Stamping-Stator.html

[Gis2011]: National Aeronautics and Space Administration, Goddard Institute for Space studies. Accessed2011.

http://data.giss.nasa.gov/gistemp/graphs/

[Nas2011]: NASA Visualization Explorer, Science Visualization Studio. Accessed2011.

http://svs.gsfc.nasa.gov/goto?3817

[Pol2010]: Company Polytec; Data Sheet PSV-400-3D Scanning Vibrometer; Cited 2010. www.polytec.com.

[Roy2010]:S. K. Roy; Physics Notes: for royphysics.net; cited 2010.
http://rophysics.schools.officelive.com/Documents/huygens_principle.pdf